INEEL/EXT-04-02459

Development of Safety Analysis Codes and Experimental Validation for a Very High Temperature Gas-Cooled Reactor

Project Number: 2003-013-K
Nuclear Energy Research Initiative
Report for January 2004 to September 2004

Chang Oh, INEEL
Cliff Davis, INEEL
Richard Moore, INEEL
Hee C. NO, KAIST
Jong Kim, KAIST
Goon C. Park, SNU
John Lee, U. Michigan
W. Martin, U. Michigan
James Holloway, U. Michigan

November 2004

Idaho National Engineering and Environmental Laboratory
Bechtel BWXT Idaho, LLC

INEEL/EXT-04-02459

Development of Safety Analysis Codes and Experimental Validation for a Very High Temperature Gas-Cooled Reactor

Chang Oh, Cliff Davis, and Richard Moore, Idaho National Engineering and Environmental Laboratory (INEEL)

Hee C. NO and Jong Kim, KAIST
Goon C. Park, SNU
John Lee and W. Martin, U. Michigan

November 2004

Idaho National Engineering and Environmental Laboratory

Idaho Falls, Idaho 83415

Prepared for the
U.S. Department of Energy
Office of Nuclear Energy
Under DOE Idaho Operations Office
Contract DE-AC07-99ID13727

CONTENTS

INTERNATIONAL NUCLEAR ENERGY RESEARCH INITIATIVE

Development of Safety Analysis Codes and Experimental Validation for a Very-High-Temperature Gas-Cooled Reactor

PI: Chang Oh, Idaho National Engineering and Environmental Laboratory (INEEL)

Collaborators: Cliff Davis and Richard Moore, INEEL
Hee C. NO and Jong Kim, KAIST
Goon C. Park, SNU
John Lee, W. Martin, and James Holloway, U. Michigan

Project Start Date: October 2003 Project Number: 2003-013-K

Projected End Date: September 2004

Research Objective:

The very high temperature gas-cooled reactors (VHTGRs) are those concepts that have average coolant temperatures above 900^0C or operational fuel temperatures above 1250^0C. These concepts provide the potential for increased energy conversion efficiency and for high-temperature process heat application in addition to power generation and nuclear hydrogen generation. While all the High Temperature Gas Cooled Reactor (HTGR) concepts have sufficiently high temperatures to support process heat applications, such as desalination and cogeneration, the VHTGR's higher temperatures are suitable for particular applications such as thermochemical hydrogen production. However, the high temperature operation can be detrimental to safety following a loss-of-coolant accident (LOCA) initiated by pipe breaks caused by seismic or other events. Following the loss of coolant through the break and coolant depressurization, air from the containment will enter the core by molecular diffusion and ultimately by natural convection, leading to oxidation of the in-core graphite structures and fuel. The oxidation will release heat and accelerate the heatup of the reactor core.

Thus, without any effective countermeasures, a pipe break may lead to significant fuel damage and fission product release. The Idaho National Engineering and Environmental Laboratory (INEEL) has investigated this event for the past three years for the HTGR. However, the computer codes used, and in fact none of the world's computer codes, have been sufficiently developed and validated to reliably predict this event. New code development, improvement of the existing codes, and experimental validation are imperative to narrow the uncertainty in the predictions of this type of accident.

The objectives of this Korean/United States collaboration are to develop advanced computational methods for VHTGR safety analysis codes and to validate these computer codes.

Research Progress:

The collaborators for this research project are the INEEL, the Korea Advanced Institute of Science and Technology (KAIST), Seoul National University (SNU), and the University of Michigan (UM).
This project consists of six tasks for developing, improving, and validating computer codes for analysis of the VHGTR. These tasks are: (1) develop a computational fluid dynamics code for benchmarking, (2) perform a reactor cavity cooling system (RCCS) experiment, (3) perform an air ingress experiment, (4) improve the

system analysis codes RELAP5/ATHENA and MELCOR, (5) develop an advanced neutronic model, and (6) verify and validate the computer codes. The primary activities and key accomplishments for each task are summarized below.

Task 1 – CFD thermal hydraulic benchmark code development (KAIST). Profs. NO and Kim developed the multidimensional system analysis tool and validated it using various experiments: NACOK natural convection test, HTTR-simulated air ingress experiment, HTTR RCCS mockup test, and SANA afterheat removal test. First, we performed the simulation for the German NACOK test in order to check out the capability of the 1-D/3-D integrated GAMMA version as well as to validate the natural convection behavior throughout the entire core during the second stage of an air ingress accident. Even with the assumption of uniform temperature condition, the predicted air or air-he mixture flows are consistent with the observed behavior at various temperature conditions. Second, the HTTR-simulated air ingress experiment which was conducted in Japan was analyzed by GAMMA using combination of 1-D and 2-D components. The test cases are: 10 equal temperature conditions and 5 non-equal temperature conditions in graphite tubes. The predicted results are in a good level of agreement with the measured data, about a 10% deviation for the onset time of natural convection. Third, the HTTR RCCS mockup tests, which were selected as benchmark problems in IAEA CRP for the analysis of afterheat removal under accident conditions, have been simulated by the GAMMA code. The temperatures of the pressure vessel (P.V.) are well predicted, demonstrating that GAMMA can be used to evaluate the hot spots on the P.V. and heat removal by thermal radiation and natural convection. Fourth, the SANA-1 self-acting afterheat removal tests, one of the IAEA benchmark problems, have been simulated to validate the porous media model that was incorporated into GAMMA. It was shown that the GAMMA code has comparable predictability with other codes (TINTE, THERMIX, TRIO-EF, and Flownex) for the SANA-1 simulations. In addition, general thermal radiation model and point reactor kinetics have been incorporated. In order to configure the power conversion system, the system component models are added: pump (or circulator), control systems, simple heat exchangers, turbine/compressor model, valve, and general tables, etc.

Task 2 – RCCS experiment (SNU). Prof. Park performed three categories of experiments, the emissivity measurement test, the separate effect test for the SNU-RCCS water tank and the integral test for the SNU-RCCS. In the emissivity measurement test, the measurement methodology was established and verified by a series of experiments. The effects of filling gas, window and reflection on the emissivity measurement were investigated. The separate effect test was performed to investigate the heat transfer phenomena in the water tank and cooling pipe. The temperature distributions of the water tank, cooling pipe surface and cooling pipe center were measured along the axis. Heat transfer coefficients of the forced convection inside the cooling pipe were derived from the experiments. The integral test facility was constructed to investigate the overall heat transfer process of the SNU-RCCS and a part of the experiments were performed to evaluate the cooling capability of the RCCS during normal operations. Prof. Park proposed the RETRAN-3D/INT and MARS as analytical tools of the SNU-RCCS. The RETRAN-3D/INT and the CFX calculations of the separate effect test were conducted for code-to-experiment validation and code-to-code benchmark respectively.

Task 3 – Air ingress experiment (KAIST). Prof. NO measured chemical parameters at chemical reaction regime. In this experiment, the order of reaction (n) and activation energy (Ea) were estimated as 0.75±0.146 and 218±3.76 kJ/mol respectively with a 95 % confidence level. For analysis of the chemical reaction in an air-ingress accident, the initial reaction rates and CO/CO_2 were measured in a temperature range of 700 to 1500 °C and an oxygen concentration of less than 20 %. The empirical correlation was developed for CO/CO_2 ratio and it yields good predictions within 10% deviation of the experimental data. A Computational Fluid Dynamics (CFD) simulation was conducted and compared to the experimental data using the oxidation parameters and the CO/CO_2 ratio developed here. We derived a graphite oxidation model to cover the chemical reaction and mass transfer over the whole temperature range and validated the model against the data. The separate experimental facility for the effects of geometry and size was designed and manufactured.

As a result, it was found that the internal reaction in the graphite material is more effective than the surface reaction. For more quantitative analysis, this experiment will be performed. High temperature annular channel experiment was designed and conducted for confirmation of heat/mass transfer analogy. And the analysis is in progress.

Task 4 – Improvement of system codes (INEEL). The RELAP5/ATHENA and MELCOR computer codes were assessed using experiments that exhibited important phenomena relevant to a LOCA in the VHGTR. Such assessments are required to validate the codes for VHTGR applications. The assessments investigated code capabilities relative to the calculation of diffusion and natural circulation.

RELAP5/ATHENA was assessed using data from an inverted U-tube experiment. Isothermal and non-isothermal experiments were simulated. Diffusion was the most important phenomenon in the isothermal experiment while both diffusion and natural circulation were important in the non-isothermal experiment. The calculated results were in reasonable agreement with the measured values.

RELAP5/ATHENA code was also assessed using natural circulation data from the NACOK experimental facility. The facility simulated the natural circulation of air through a scaled model of a reactor containing a pebble bed core. The calculated mass flow rates were in reasonable agreement with the measured values.

The MELCOR code was assessed using data from a ternary two-bulb diffusion experiment. Previously, we reported some discrepancies between the MELCOR prediction and the measured data. We simulated the same experiment with the latest released version of the code, which included the entire set of gas reactor updates provided by INEEL. The results from this new calculation agree very well with the experimental results.

Task 5 – Neutronic modeling (UM). The UM team has made substantial progress in developing a full-core model of the VHTR, including double heterogeneities and thermal/hydraulic feedback. The particle fuel has been modeled at four levels of increasing complexity, from a single microsphere cell to a fuel compact cell to a hexagonal block (assembly) cell, to a full-core model with axial and radial reflectors. All models have included the particle fuel as both a homogeneous mixture of fuel and graphite as well as its true heterogeneous geometry. The modeling of the microsphere fuel has included (1) heterogeneous microspheres centered in a cubical cell of graphite (to preserve the packing fraction), (2) heterogeneous microspheres randomly located in the cubical cell of graphite, and (3) two-region microsphere versions of the heterogeneous microspheres. The results show the importance of modeling the double heterogeneity. The results also indicate that one can model the microspheres centered versus randomly located in the cubical cells and that two regions may be sufficient to accurately account for the multiple microsphere regions. Full-core MCNP5 calculations have been completed for homogeneous fuel and heterogeneous fuel with microspheres centered in the unit cells. Coupled neutronic-thermal/hydraulic calculations have been performed with MCNP5 and RELAP5/ATHENA to determine the global flux/power distribution with temperature feedback. These calculations have been performed with homogeneous fuel blocks and are considered preliminary.

Task 6 -- Verification and validation (INEEL and KAIST).

Each party has completed initial assessments during the past year. Additional assessments will be performed in year 2005. Assessments of the data being generated at SNU will also be performed.

Planned Activities:

The following work will be performed during Year 3.

- Test the recently developed graphite oxidation model, perform further validation of SNU RCCS experiments, and perform transient analysis of the depressurized LOFC accidents.

- Perform GAMMA analysis for verifying component models, point kinetics and system component models.

- Investigate a geometry effect on graphite oxidation and the effect of moisture and burn-off.

- Complete neutronics models.

- Complete the coupled neutronic-T/H calculations to determine the converged flux/power distribution in the VHTR.

- Perform coupled neutronic-T/H calculations for heterogeneous fuel and compare with the homogeneous fuel calculations.

- Perform full-core MCNP5 calculations with heterogeneous fuel regions, but with microspheres randomly located within a fuel compact (preserving packing fraction) rather than arranged in a grid or confined to a cubical cell.

- Initiate analysis of depletion. This will involve choosing a depletion module to interface with MCNP5, as well as examining the effect of depletion on the analysis of the double heterogeneities.

- Obtain global flux/power distributions as a function of depletion, including temperature feedback.

- Determine decay heat distribution from the global flux/power distribution as a function of depletion.

- Validate and verify all the models developed from this study using experimental data. Test the recently developed graphite oxidation model, perform further validation of SNU RCCS experiments, and perform transient analysis of the depressurized LOFC accidents.

Narrative:

Task 1: CFD TH Code Development (KAIST)

Task Status and Significant Results

The objective of this task is to develop a multidimensional system analysis tool for the thermo-fluid transport processes in VHTGRs. Following the incorporation of basic thermo-fluid models and benchmarks with the simplified tests for air ingress and natural convection in a pebble bed in the last year, we added the general thermal radiation model and point reactor kinetics as well as various system component models in order to analyze various kinds of the system transients. At the same time, the extensive validation works were carried out as described below.

Task 1-1: Incorporation of special component models

Thermal radiation

Radiation heat transfer in the enclosure is well-modeled by using an irradiation/radiosity method (Holaman, 1986) which assumes that the fluid is non-participating and the radiation exchange between the surfaces is gray and diffuse. The net radiation heat flux from an agglomerated surface k, which consists of the N_k faces of the original mesh, is given by

$$q_{rk}^{"} = \left[\left(\sum_{j \neq k}^{M} F_{kj} \right) \varepsilon_k \overline{T}_k^4 - \varepsilon_k \sum_{j \neq k}^{M} F_{kj} J_j \right] \left[\varepsilon_k + (1-\varepsilon_k) \sum_{j \neq k}^{M} F_{kj} \right]^{-1}, \tag{1-1}$$

where

$q_{rk}^{"}$ = radiative heat flux of a surface k $\left(W/m^2\right)$

F_{kj} = view factors

ε_k = emissivity of a surface k

$\overline{T}_k$ = average temperature of an agglomerated surface k $\left(\mathrm{K}\right)$

J_j = radiative heat flux of a surface j $\left(W/m^2\right)$

Point reactor kinetics

The point kinetic equations (Duderstadt, 1976) consist of the (I+1) first-order ordinary differential equations.

$$\begin{aligned} \frac{dP}{dt} &= \frac{\rho - \beta}{\Lambda} P + \sum_{i=1}^{I} \lambda_i C_i \\ \frac{dC_i}{dt} &= -\lambda_i C_i + \frac{\beta_i}{\Lambda} P, \quad \text{for } i = 1, 2, \cdots, I \end{aligned} \tag{1-2}$$

where

$P =$ total thermal power, W

$\rho =$ reactivity

$\beta =$ total fraction of delayed neutrons

$\Lambda =$ effective prompt neutron lifetime, s

$C_i =$ concentration of the delayed-neutron precursors, W

$\lambda_i =$ decay constant of the delayed-neutron precursors, s^{-1}

The decay heat equations are given by

$$\frac{dH_j}{dt} = -\lambda_j^H H_j + E_j P, \quad \text{for } j = 1,2,\cdots,J \tag{1-3}$$

where

$H_j =$ power from decay heat group, j, (W)

$\lambda_j^H =$ decay constant of decay heat group, j, (s^{-1})

$E_j =$ effective energy fraction of decay heat group, j

$J =$ total # of decay heat groups (11 for ANS71, 69 for ANS79)

The total thermal power generated in the fuel from prompt fission, precursor decay, and delayed fission is determined by

$$P_{tot} = \left(1 - \sum_{j=1}^{J} E_j\right) P + \sum_{j=1}^{J} \lambda_j^H H_j \tag{1-4}$$

When the Xe poison effect is selected, the following two equations are coupled to the point kinetic equations through the reactivity feedback.

$$\begin{aligned} \frac{dI}{dt} &= -\lambda_I I + \frac{\gamma_I}{E_R} P \\ \frac{dX}{dt} &= -\lambda_X X - \frac{\sigma_a^X}{\sum_f} \frac{P}{E_R} X + \frac{\gamma_X}{E_R} P + \lambda_I I \end{aligned} \tag{1-5}$$

where

$I, X =$ Iodine and Xenon concentrations

$\lambda_I, \lambda_X =$ Iodine and Xenon decay constants

$\gamma_I, \gamma_X =$ Iodine and Xenon fission yields

$\sigma_a^X =$ microscopic neutron capture cross section of Xenon

$\sum_f =$ macroscopic neutron fission cross section of UO_2 fuel

The excessive reactivity by Xe poison is represented as

$$\Delta\rho = -\frac{\sigma_a^X}{\sum_a} X \tag{1-6}$$

After determining the initial conditions, all the coupled equations are solved using the 4th-order Runge-Kutta integration method. The time step for the integration is 20 times (assessed later) smaller than the main loop time step to reduce numerical errors.

System component models

The system component models incorporated into the GAMMA code are as follows:

- Abrupt area change
- Critical flow check
- Valve and Pump (or circulator)
- Simple heat exchangers
- Simple turbine/compressor
- Control elements (arithmetic and logical operators and dynamic controllers)

Task 1-2: GAMMA validation

First, the NACOK experimental apparatus (Schaaf, 1998) consisted of a rectangular experimental channel with a height of 7.3 m, a circular return pipe and connecting pipes with a diameter of 125 mm, and a coaxial pipe has been simulated. The experimental channel had a cross-section of 300×300 mm with a regular arrangement of 25 spheres each having a diameter of 6 cm in one layer. Four test series given in Table 1-1 were performed with fixed temperature conditions (Tr=200°C, 400°C, 600°C, 800°C) at the return tube, with experimental channel temperature (Te) varying by a step change of 50°C ranging from 200°C to 1000°C.

Table 1-1. Simulated SANA-1 experimental cases

Fluids	Return cold pipe temperature, Tr (°C)	Experimental channel temperature, Te (°C)
air	200 400 600 800	250-1000 450-1000 650-1000 850-1000
20% He-air	200 400	250-800 450-850
40% He-air	200 400	250-800 450-850

Figure 1-1 shows the GAMMA nodal scheme of the NACOK facility. In the simulation, wall temperatures along the experimental channel and connecting and return pipes are assumed to be uniform and kept to be constant. The effective thermal conductivity of the pebble bed is calculated by the cell-model of Zehner/Bauer/Schlünder and for free convective heat transfer coefficient Churchill and Chu's correlation is used at the return cold and connecting pipes. The boundary effects near the channel wall are neglected since half-spheres are filled in empty space on the wall. Five friction formulas (Ergun, Molerus, KTA, Tallmadge, and Macdonald) are investigated for sensitivity. Even with the assumption of uniform temperature condition, the predicted air mass flows shown in Figure 1-2 agree closely with the experiment. No significant difference is shown for different friction formula. Rather than, the overall difference seems from the combined effect of the heat transfer between wall and fluid and the hydraulics in a pebble bed and at the wall boundary.

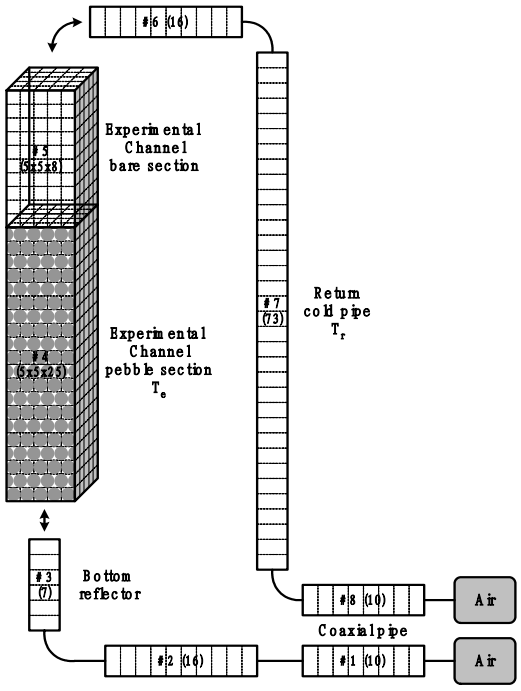

Figure 1-1 Nodal scheme for the NACOK test facility.

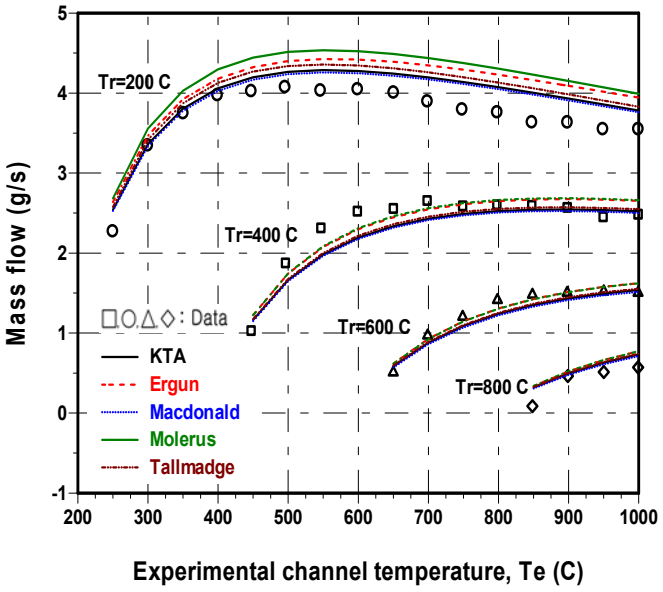

Figure 1-2 Predicted mass flows for the air-filled case.

Second, the HTTR-simulated experimental facility (Takeda, 1997) consisted of a reactor core simulator, a high-temperature plenum, a water-cooled jacket corresponding to the reactor vessel and simulated inlet and outlet pipes to the coaxial pipe has been simulated. The reactor core simulator has four graphite tubes (one central, #4, and three peripherals, #5) and a ceramic plenum. In order to consider the effect of local natural circulation which promotes air transport through the annular passage, an annular passage (#8) is modeled by 2-D component. Figure 1-3 shows the predicted oxygen mole fractions for the non-equal temperature test case (850°C/750°C in central/peripheral graphite tubes). In the first calculation, as shown at Figure 1-4, we

have found that the CO_2 produced at the bottom region of graphite tubes is trapped in the hot plenum (#3), thereby delaying the onset time of natural convection by about 1.5 days. Its delay is presumed to be caused by several internal leak paths, which are established directly as well as indirectly through the thermal insulator (#7) from the hot side to the cold side. Therefore, in the subsequent calculation, all the leak paths are modeled by single path (#13) with a very small flow area. The predicted results considering an internal leak path show better agreement with the experimental data than that without a leak path. For all experimental cases simulated, Figure 1-5 shows that the onset times of natural convection are accurately predicted within a 10% deviation.

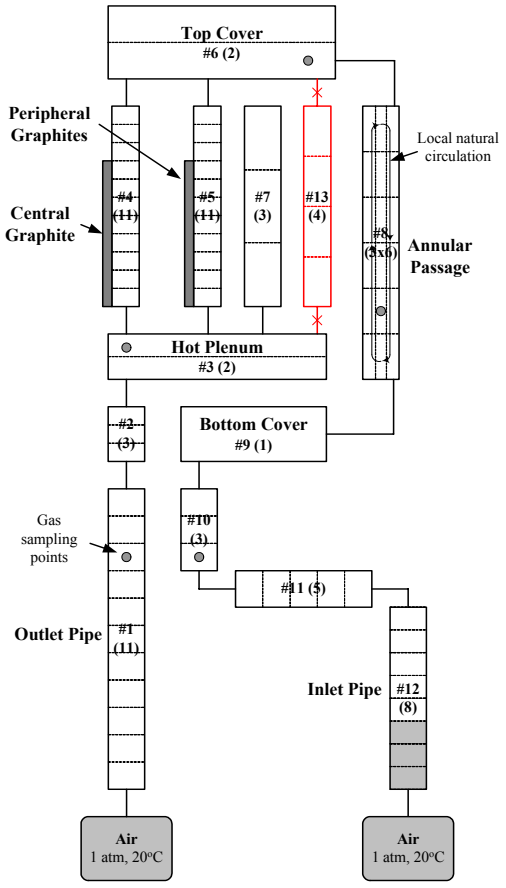

Figure 1-3. Nodal scheme of the HTTR-simulated system.

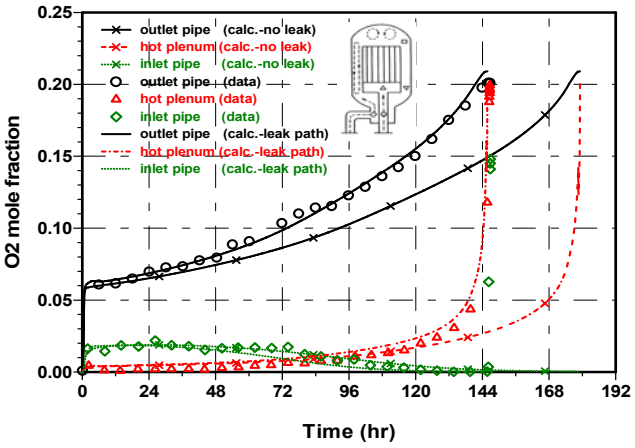

Figure 1-4. Predicted O_2 mole fractions

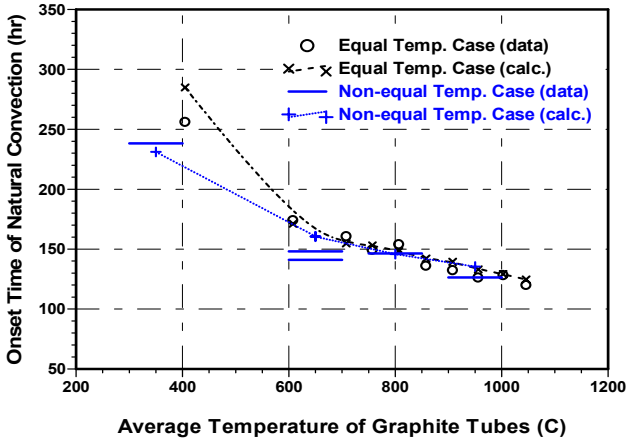

Figure 1-5 Predicted onset times of natural convection.

Third, the HTTR RCCS mockup test facility (IAEA, 2000), which consisted of a pressure vessel (P.V.) with 1 m in diameter and 3 m high, a heater block simulating decay heat, the tube-type three cooling panels surrounding the P.V., and the cavity wall occupied by air at the atmospheric pressure, has been simulated.

Seven tests were conducted with different kinds of fluids in a P.V. (vacuum, He, or N_2) and cooling panels (air or water), total heating powers, axial power shapes, and P.V. top head with/without the stand pipes simulating the control element driving assembles. We used the axi-symmetric mesh layout by assuming the rotational symmetry of the apparatus and considered the radiation heat transfer in each enclosure by using the irradiation/radiosity method for the gray and diffuse surfaces. Since the heat removal contribution by natural convection is not negligible, proper correlations are selected and applied to specific surface types. For the simulation, the temperature distribution of cooling panels is used as a boundary condition. Figure 1-6 shows the calculated surface temperature profiles for one representative case (vacuum in a P.V.) and the relative contribution of thermal radiation to total heat removed from the outside of the pressure vessel. The calculated ratio of heat transferred by thermal radiation to the total heat input is about 68%-97%, comparable to that of the other analysis codes. The GAMMA code predicts well the heat removal by free convection while some of other analysis codes slightly underestimate it.

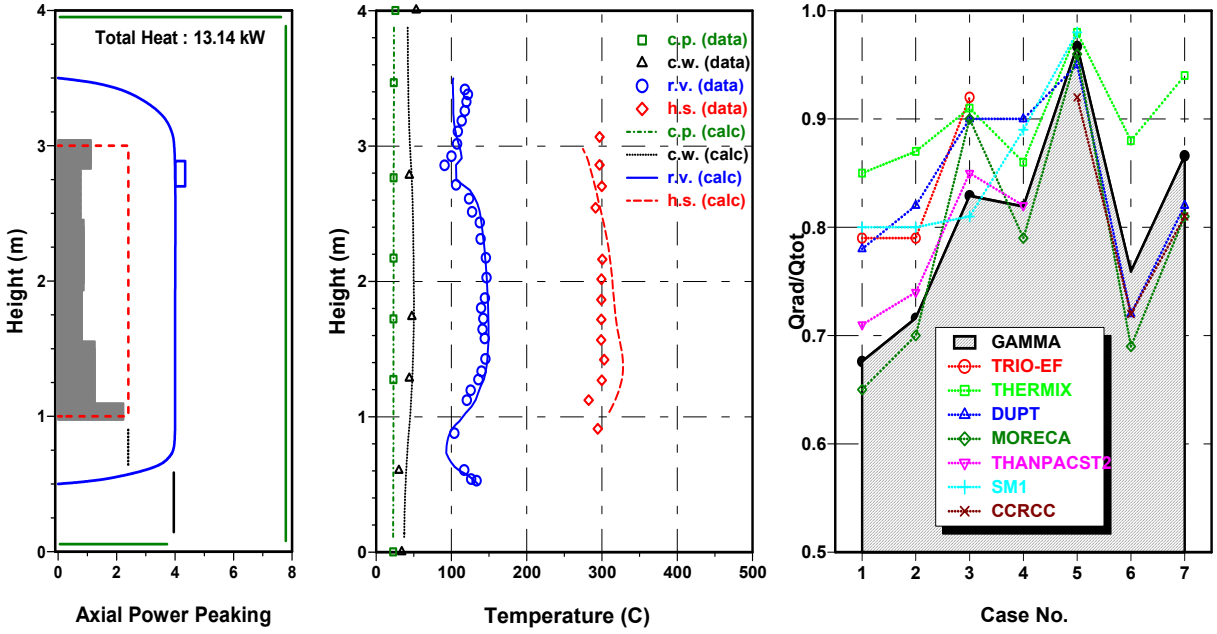

Figure 1-6 Calculated results: surface temperature profiles of heater, P.V., and cavity wall for the vacuum case 1 (center), relative contribution of thermal radiation to total heat removal for all the test cases (right)

Fourth, the SANA-1 self-acting afterheat removal test (IAEA, 2000), one of the IAEA benchmark problems, has been simulated to validate the porous media models which is incorporated into the GAMMA code. All kinds of test cases listed in Table 1-2 have been investigated and the simulation results have been compared with other codes' (TINTE:Germany, THERMIX:China, TRO-EF:France, and Flownex:South Africa) results. Due to the rotational symmetry of the SANA-1 facility, the GAMMA axi-symmetric mesh scheme with 1000 meshes for the fluid region and 1400 meshes for the solid region including a pebble bed was used.

Table 1-2. Simulated SANA-1 experimental cases.

Configurations	Pebble diameter (mm)	Heating tube/pebble bed geometry	Gas	Heating power (kW)
(1)	60	long heating element	N_2, He	10, 30
(2)	60	short heating element at the top	N_2, He	20
(3)	60	short heating element at the bottom	N_2, He	20
(4)	60	short heating element at the bottom with gas plenum above the pebble bed	N_2, He	20
(5)	30	long heating element	N_2, He	10, 30
(6)	60	long heating element	N_2, He	30 to 10 ramp 10 to 25 step change

Among the predictions, Figure 1-8 shows the calculation results for one representative case, the non-uniform heating test at the bottom. In all the simulated cases, the prediction results of GAMMA agree closely with the measured data and are comparable to the other codes' results, although some deviations are observed in the lower or upper layers due to the boundary effects at the edge of the pebble bed. The simulated results show that the heat transport by conduction/convection/radiation in the pebble bed, which is expected to occur during the accident conditions including an air ingress accident, is well predicted using the available correlations for the effective thermal conductivity and the interfacial convective heat transfer.

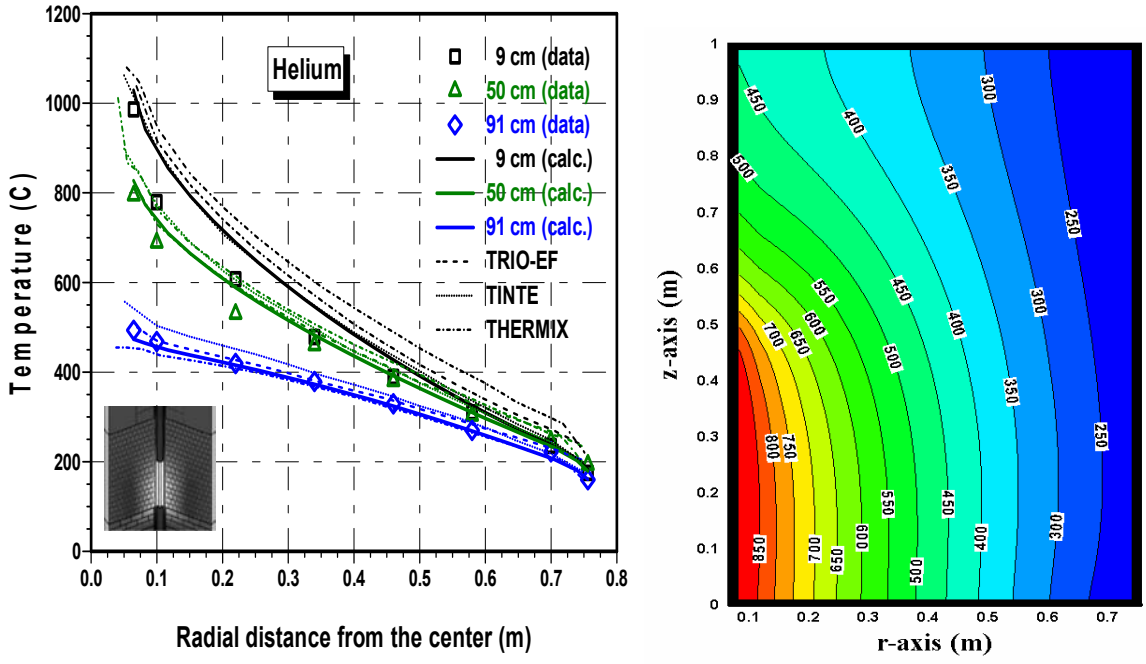

Figure 1-8 Calculated pebble temperature distributions and gas temperature contour: bottom element heating at 20kW, He coolant, 6 cm pebble.

In the simulations of SANA power ramp up and down transient tests, as shown at Figure 1-9, some deviations are shown in the spatial distribution of pebble temperatures. However, the pebble temperature trend as a function of time are well predicted and well in accordance with the other codes' results and the measured data.

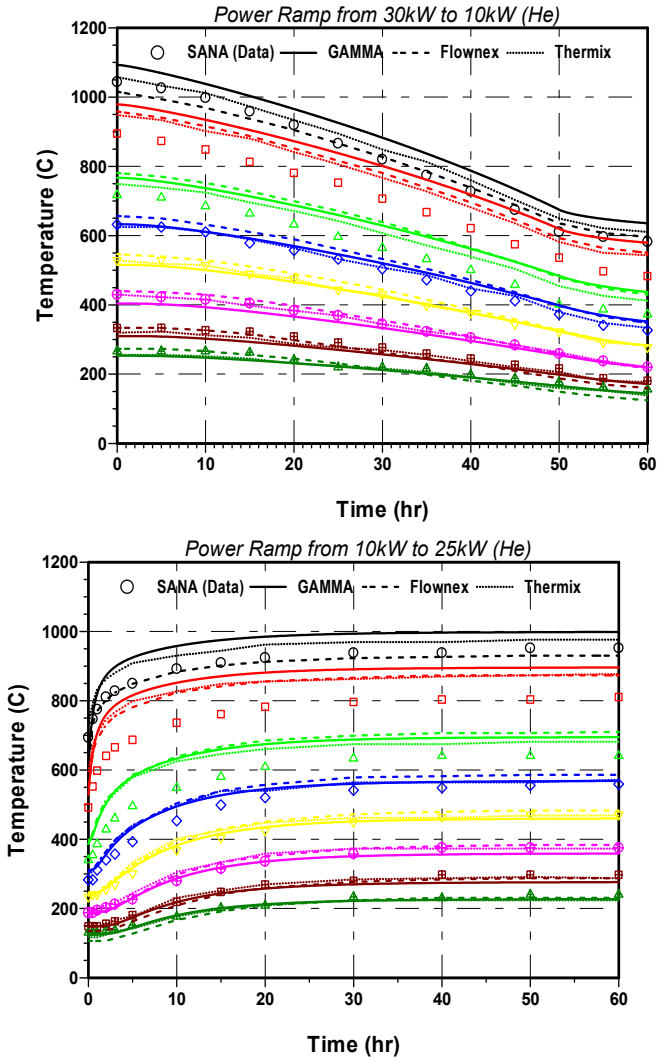

Figure 1-9 Calculated results for the SANA power ramp up and down tests of the He-filled case.

Next Quarter Activities

- Validation with the SNU RCCS experiment
- Testing of KAIST's graphite oxidation model
- Preparation of GAMMA inputs for 250MWt PBR and 600MWt PMR
- System analysis for the typical GCR transients, like the depressurized LOFC accident.

Issues/Concerns

There are neither issues nor concerns. This task is on schedule.

Task 2: RCCS Separate Experiment (SNU)

Task Status and Significant Results

We proposed a new concept of the RCCS, named SNU-RCCS to overcome the disadvantage of both the weak cooling ability of air-cooled RCCS and the complex structures of water-cooled RCCS. The schematic diagram of the SNU-RCCS is presented in Figure 2-1. The system mainly consists of two parts, water tank located between the containment and reactor vessel and four trains of air cooling system installed in the water tank. In normal operations, the heat loss from the reactor vessel is transferred into the water tank via cavity. The heat is removed by forced convection of air flowing through cooling pipes. During the LOFC accident, the after heat is passively removed by the water tank without the forced convection of air and the RCCS water tank is designed to provide sufficient passive cooling capacity of the after heat removal for three days. This new concept of the RCCS is believed to have advantages of better cooling capability and simpler structure compared to existing air-cooled RCCS and water-cooled RCCS respectively.

The objectives of this task are to carry out the experiment for the SNU-RCCS to provide the experimental data for the validation of the thermal hydraulic code being developed at KAIST and to evaluate the feasibility of the system using the experiments and system analysis codes validated by code-to-experiment and code-to-code benchmarks. To achieve these objectives, we planned three categories of experiments: 1) emissivity measurement test, 2) separate effect test for the SNU-RCCS water tank and, 3) integral test for the SNU-RCCS test. In this report, the results of these experiments are presented. Also, the code-to-experiment validation for the system analysis codes started and the RETRAN-3D/INT and CFX calculation were conducted for the separate effect test results. The introductory results of the analyses were described in this report.

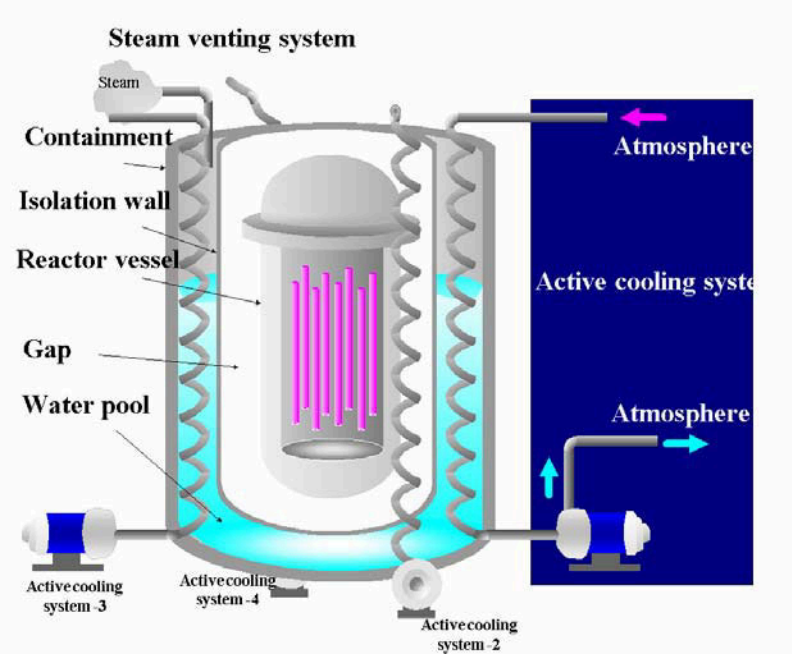

Figure 2-1 Schematic diagram of the SNU-RCCS.

Task 2-1 Emissivity measurement experiment

The heat loss and the after heat can be transferred from the core to the ambient air via several heat transfer processes such as conduction, radiation, and convection. Among these processes, radiation heat transfer was reported to be the most important process, especially in accident condition, because the radiation heat transfer rate increases with the reactor vessel temperature. In accident condition the radiation heat transfer is known to be over 70% of total heat transfer from the reactor vessel surface to the RCCS through the cavity (IAEA, 2000).

Since the rate of radiation heat transfer tends to change according to the emissivities, temperatures and geometry of the reactor vessel and cavity wall, it is very important to know the exact emissivity of the materials and the temperatures for the calculation of the heat removal in the RCCS. For these reasons, several researches have been performed in order to evaluate the effect of emissivity on the heat transfer in RCCS of VHTGR (N. Kuzavkov, 2000). In most studies the supposed emissivity values of reactor vessel were utilized in numerical calculations. However, unfortunately, the emissivity depends on many factors: roughness of surface, temperature, background radiation, and oxidation level of materials, and so on. The information on the emissivity for a given material in real circumstance of the RCCS, therefore, is required to analyze the heat transfer rate in VHTGR (D. Especel, 1996).

As a preliminary process of the emissivity measurement at the integral test facility of the SNU-RCCS, an experiment was performed to verify the emissivity measurement characteristics using the infrared thermometer and the uncertainty factors which would occur during the main experiment.
The test facility is shown in Figure 2-2 and it is mainly composed of the stainless steel chamber, the infrared thermometer, the hot plate, and the thermocouple. The emitting material was carbon steel, the same material with the reactor vessel of the SNU-RCCS. The emissivity was measured by the infrared thermometer within the temperature range of 100 to 500^{0}C. This range of the temperature covers the range of the temperature of the reactor vessel in both normal and accident conditions. The infrared thermometer has temperature range of -32~900^{0}C, wavelength range of 8~14 ㎛, accuracy of 1 %, and spot size of 16 Φ at 800 mm. Generally the infrared thermometer measures the temperature with radiation emitted from the surface of target material. That is, the infrared thermometer cannot measure the true temperature of target material without the true emissivity of that. Using this property inversely, the emissivity can be estimated if the true temperature of material is known. For using this principle the thermocouple was installed in the center of hot plate and the temperature was measured to compare with the temperature measured by infrared thermometer.

Effect of Window

Zinc Selenide (ZnSe) window with 50 mm diameter and 5 mm thickness was equipped at the head of chamber. Figure 2-3 shows the effect of the ZnSe window estimated by experimental results with and without window in the air. By dividing the experimental value with window by that without window, the transmittance of window was estimated as 74.7 to 76.7 % within maximum error range of 1.5. The results satisfies the range of material characteristic transmittance in wavelength range of 8~14 ㎛, that is 72 to 76 %.

Effect of Gases

Generally, it is known that the kind of gas filled in cavity and its concentration can affect the measurement of emissivity (S.S.Sazhin, 1996; N. Lallemant, 1996). In normal operation condition of VHTGR the cavity would be filled with air. However, if the pressure boundary is broken during the accident, the coolant like the helium can be soaked into the cavity. Also, if the inner surface of water tank is broken, it is possible that water spills into the cavity and evaporates. In order to estimate the effect of gas filled in the cavity, the experiments are performed with three gases of each different concentration.

In order to evaluate the effects of air and helium concentration on the measurement of emissivity, the experiments were carried out with the various concentrations. Figures 2-4 and 2-5 show the measured emissivity with the variation of the concentration. In both cases, the changes of emissivity according to the concentration are very small, within 3 % of the average value. This means that the effect of the air concentration on the measurement of emissivity is not significant. That is, air and helium do not absorb and reflect the radiation in the wavelength range of 8~14 ㎛, the temperature range of 100~500^{0}C, and the pressure range of 0.2~1.0 atm. Also the compensated emissivity by transmittance of ZnSe varied from 0.84 to 1.0 with temperature. This value is lager than theoretical emissivity value of oxidized carbon steal with range of 0.80~0.95. This reason will be discussed later.

The effect of steam on the measurement of emissivity was estimated. Figure 2-6 shows the relatively low emissivity compared with the other experiments using air and helium because the steam absorbs and reflects the radiation (L. A. Dombrovsky, 2000). Inner surface of chamber covered with the water droplet absorbs the background radiation so that the increase of the measured emissivity due to background radiation was almost not observed. Since the increase of temperature causes more evaporation inside chamber, the measured emissivity decreased gradually. Over about 300^{0}C the steam evaporated sufficiently inside chamber and overproduced steam is released out of chamber to maintain 1atm. So steam concentration becomes to be saturated, and the measured emissivity shows almost constant value.

Background Radiation Effect

The most important factor of uncertainty in the measurement of emissivity is the background radiation. The results of the two experiments for the air and the helium show that the measured emissivity increases with the temperature, which is believed to be caused by background radiation. In order to verify this phenomenon clearly the experiments to measure the emissivity were carried out inside and outside stainless steel chamber. The measured emissivity inside chamber was higher than that of outside chamber as shown in Figure 2-7. The additional radiation due to the chamber has the ratio about 4~18 % with the temperature. In order to compensate the effect of background radiation the qualitative analysis of radiation is needed. It is expected that it could be solved by commercial code such as NEVADA (TAC Technologies, 2000). The result from the code will be compared with the experimental results. With the same methodology the actual emissivity will be measured in SNU-RCCS and the radiative heat transfer in the cavity will be analyzed.

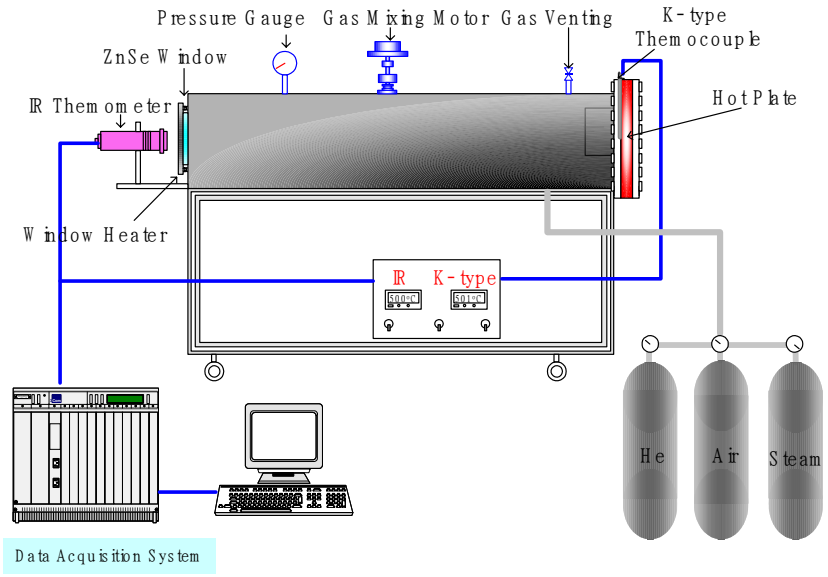

Figure 2-2 Schematic diagram of the experiment test facility.

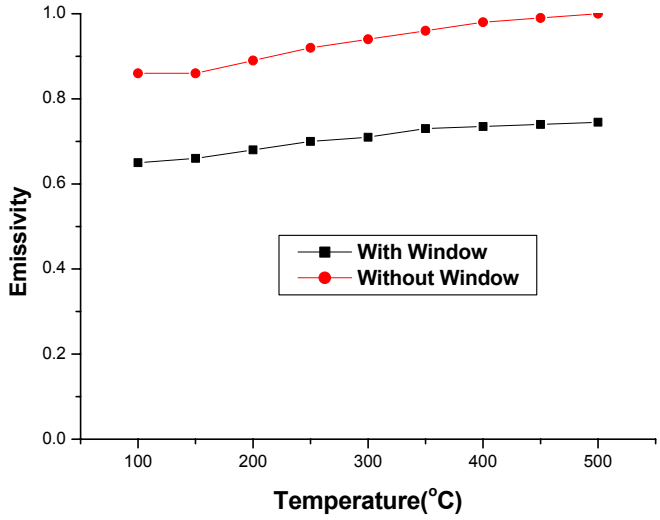

Figure 2-3 Emissivity with or without window.

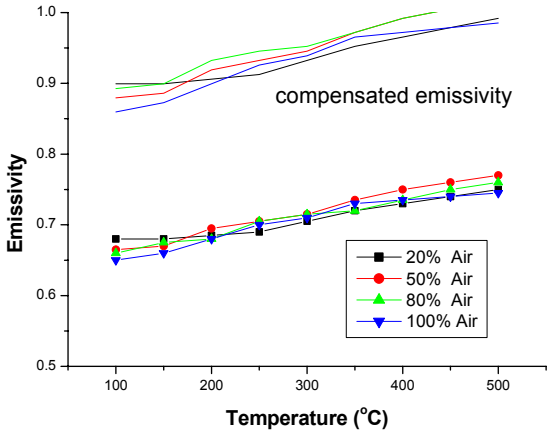

Figure 2-4 Change of emissivity with air concentration.

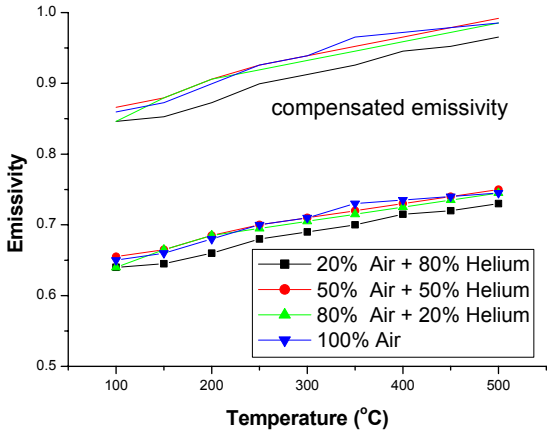

Figure 2-5 Change of emissivity with helium concentration.

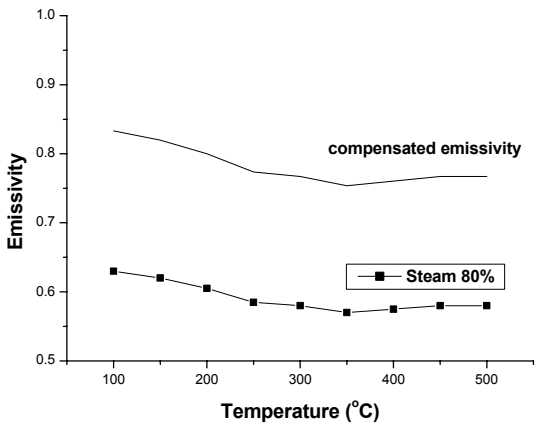

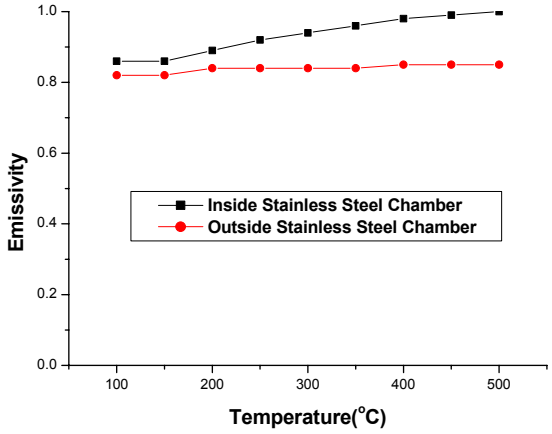

Figure 2-6 Effect of steam on measurement of emissivity. Figure 2-7 Effect of background radiation.

Task 2-2 Separate effect test for the water pool of the SNU-RCCS

We have performed separate effect tests for the heat transfer phenomena in the water tank of the SNU-RCCS to investigate the natural convection of water in the water tank and the forced convection of air in the cooling pipe. From the measurement of local temperature distributions in the tank water, cooling pipe surface and cooling pipe center we would like to derive heat transfer coefficients of the cooling pipe and evaluate heat transfer coefficient correlations of previous studies.

Figure 2-8 shows the schematic diagram of the test facility and the measuring parameters and instrumentations are summarized in Table 2-1. The test section simulates a quarter section of the water tank and it has six U-bend heaters in the vicinity of the inner wall to reproduce the heat coming from the cavity wall. The total power of the heaters was calculated considering the scaling ratio of the SNU-RCCS test facility (1/100 power ratio). To remove the heat, a cooling pipe is equipped in the test section which has fifteen U-bends as shown in Figure 2-8. The outlet of the cooling pipe is connected to the suction of a blower and ambient air flows through the cooling pipe. The experimental cases are tabulated in Table 2-2.

Figure 2-9 shows the experimental results of the pressure drop measurement between the inlet and outlet of the cooling pipe. The frictional pressure drop was computed from Eq.(2-1) applying the friction factor correlation of Nikuradse (1966) for a smooth circular duct.

$$\Delta P_{fric} = \frac{4fL}{D_h}\frac{\rho_g v_g^2}{2} \tag{2-1}$$

$$f = 0.0008 + 0.0553\,\mathrm{Re}^{-0.237} \tag{2-2}$$

The form loss pressure drop was calculated subtracting the friction loss from the total pressure drop as shown in Figure 2-9 and a comparison among the calculated values and predicted values using the form loss coefficient of a standard U-bend like Eq. (2-3) is provided in Figure 2-10.

$$K = \frac{K_1}{\mathrm{Re}} + K_\infty (1 + 0.5 D^*) \qquad \text{(Hooper, 1981)} \tag{2-3}$$

where, $K_1 = 1000$, $K_\infty = 0.35$ in U-bend.

The figure shows reasonable agreement among the experimental data and the predicted form loss pressure drops using the above correlation and it was found that the loss coefficient of a standard U-bend is available for the cooling pipe of the SNU-RCCS. These experimental results of the pressure drop and loss coefficient will be used for the validation of the CFD code and the preparation of the input deck for safety analysis codes such as RETRAN-3D/INT and MARS.

Figure 2-11 indicates the experimental results of the temperature distributions at the water tank, cooling pipe surface and axis of the cooling pipe. As air flows through the cooling pipe, its temperature increases markedly. However the temperature of the cooling pipe surface shows little variation along the pipe axis. The axial temperature distributions are therefore similar to those for heat transfer in a tube with constant surface temperature condition. The bulk liquid temperature is higher at the top part of the tank than at the bottom part by 1~2^{o}C only. This means the water in the tank are well mixed by natural circulation and a thermal stratification does not occur in the water tank since large portion of the heat is removed at the top of the tank as a result of large temperature difference between air and water.
From the experimental results the heat transfer coefficient for the forced convection was calculated. Applying conservation of energy, Eq. (2-4), to the differential control volume of Figure 2-12, we obtain

$$d\dot{q}_{conv} = \dot{m}_g c_p dT_m = 2\pi h r_{in} dx \left(T_{s,in} - T_m \right) \quad \text{or} \quad h = \frac{\dot{m}_g c_p}{2\pi r_{in}} \frac{dT_m}{dx} \frac{1}{T_{s,in} - T_m} \tag{2-4}$$

The flow averaged mean temperature and pipe inner surface temperature in above equation should be substituted by the temperature of the cooling pipe center and outer surface that were measured in the experiments to calculate the heat transfer coefficient. Since information for the velocity and temperature fields of the cooling pipe is necessary to obtain the mean temperature, we assumed that those are the same with the velocity and temperature profiles of the fully developed turbulent flow under the constant temperature condition. The appropriateness of this assumption will be discussed with a calculation result using the CFX code later. Applying the assumption, the flow averaged mean temperature can be expressed as follows.

$$T_m = \frac{3}{2(n+2)} T_{s,in} + \frac{2n+1}{2(n+2)} T_c \quad \text{(where, n=7) (Kakac et al., 1987)} \tag{2-5}$$

In Figure 2-12, the heat transfer in the cooling pipe by conduction can be expressed as,

$$d\dot{q}_{cond} = \frac{2\pi dx k \left[T_{s,out} - T_{s,in} \right]}{\ln \left(r_{out} / r_{in} \right)} \tag{2-6}$$

Equating Eq.(2-4) and Eq.(2-6) it follows that the derivative of the mean temperature is related to the temperatures at the cooling pipe inner and outer surface.

$$\frac{dT_m}{dx} = \frac{2\pi k}{\dot{m}_g c_p} \frac{\left[T_{s,out} - T_{s,in} \right]}{\ln \left(r_{out} / r_{in} \right)} = \frac{2\pi h r_{in}}{\dot{m}_g c_p} \left[T_{s,in} - T_m \right] = \frac{2\pi h r_{in}}{\dot{m}_g c_p} \left[T_{s,in} - T_c \right] \frac{2n+1}{2(n+2)} \tag{2-7}$$

Rearranging Eq.(2-7), we obtain Eq. (2-8)

$$\frac{k(T_{s,out}-T_{s,in})}{\ln(r_{out}/r_{in})} = hr_{in}(T_{s,in}-T_c)\frac{2n+1}{2(n+2)} \text{ or } T_{s,in} = \frac{\dfrac{kT_{s,out}}{\ln(r_{out}/r_{in})} + hr_{in}T_c\dfrac{2n+1}{2(n+2)}}{hr_{in}\dfrac{2n+1}{2(n+2)} + \dfrac{k}{\ln(r_{out}/r_{in})}} \tag{2-8}$$

Substituting from Eq.(2-8), Eq.(2-4) and Eq. (2-7) can be expressed as follows,

$$h = \frac{\dot{m}_g c_p}{2\pi r_{in}}\frac{dT_m}{dx}\frac{2(n+2)}{2n+1}\frac{1}{\dfrac{\dfrac{kT_{s,out}}{\ln(r_{out}/r_{in})} + hr_{in}T_c\dfrac{2n+1}{2(n+2)}}{hr_{in}\dfrac{2n+1}{2(n+2)} + \dfrac{k}{\ln(r_{out}/r_{in})}} - T_c} \tag{2-9}$$

$$\frac{dT_m}{dx} = \frac{3}{2(n+2)}\frac{dT_{s,in}}{dx} + \frac{2n+1}{2(n+2)}\frac{dT_c}{dx} \tag{2-10}$$

$$= \frac{2n+1}{2(n+2)}\frac{dT_c}{dx} + \frac{3}{2(n+2)}\left[\frac{\dfrac{k}{\ln(r_{out}/r_{in})}\dfrac{dT_{s,o}}{dx} + r_{in}\dfrac{2n+1}{2(n+2)}\left[\dfrac{T_c dh}{dx} + \dfrac{h dT_c}{dx}\right]}{\dfrac{k}{\ln(r_{out}/r_{in})} + hr_{in}\dfrac{2n+1}{2(n+2)}} - \frac{\left(\dfrac{kT_{s,o}}{\ln(r_{out}/r_{in})} + hr_{in}T_c\dfrac{2n+1}{2(n+2)}\right)\cdot\dfrac{2n+1}{2(n+2)}r_{in}\dfrac{dh}{dx}}{\left(\dfrac{k}{\ln(r_{out}/r_{in})} + hr_{in}\dfrac{2n+1}{2(n+2)}\right)^2}\right]$$

The spatial derivatives of the temperature at the outer surface and axis of the pipe in Eq. (2-10) can be obtained from the experimental data with the multiple regression method. Assuming the spatial distribution of the heat transfer coefficient to a third order polynomial, we can solve the Eqs. (2-9) and (2-10) at each measuring location. The calculated local heat transfer coefficients are presented in Figure 2-13. To consider the effect of the conduction through the cooling pipe, the heat transfer coefficients were recalculated with an assumption, $T_{s,in} = T_{s,out}$ and compared with the previously calculated values as shown in Figure 2-14. As a result it was found that the effect of the conduction is negligible for the calculation of the heat transfer coefficient. Excluding the effect of conduction, Eq.(2-9) can be reduced as follows,

$$h = \frac{\dot{m}c_p}{2\pi r_{in}}\frac{1}{T_s - T_c}\frac{2(n+2)}{2n+1}\frac{dT_m}{dx} = \frac{\dot{m}c_p}{2\pi r_{in}}\frac{1}{T_s - T_c}\frac{2(n+2)}{2n+1}\left[\frac{3}{2(n+2)}\frac{dT_s}{dx} + \frac{2n+1}{2(n+2)}\frac{dT_c}{dx}\right] \tag{2-11}$$

Integrating above equation along the axis, we can obtain averaged heat transfer coefficients.

$$\bar{h} = \frac{1}{L}\int_0^L h dx = \frac{\dot{m}c_p}{2\pi rL}\frac{2(n+2)}{2n+1}\int_0^L \frac{1}{T_s - T_c}\left[\frac{3}{2(n+2)}\frac{dT_s}{dx} + \frac{2n+1}{2(n+2)}\frac{dT_c}{dx}\right]dx \tag{2-12}$$

In Figure 2-15, the calculation results of the Nusselt number in the cooling pipe were indicated and compared with correlations of previous studies to evaluate the correlations. The Dittus-Boelter correlation (Dittus and Boelter, 1930) for fully developed turbulent flow and the Mori-Nakamura correlation (Mori and Nakayama, 1967) for a helical coil which is implemented in RETRAN3D/INT (Paulsen et al, 1996) were used for the

evaluation. As a comparison result, our experimental data found to be 30% higher than the predicted curve by Dittus-Boelter for a straight pipe because of the effect of secondary flow in curved pipes. Also the Nusselt numbers are about 10 % larger for the cooling pipe than for a helical coil tube which has the same radius (r_{coil}=0.5m) with our test facility. This underestimation is seemed to be caused by the presence of the U-bend. Tailby and Staddon (1970) reported Nusselt number increments for air cooling in 180^o bend. They explained that in a bend secondary flow pushes heavier fluid particles toward the outer wall and lighter ones toward the inner wall and thus the bend augments the secondary flow resulting in significantly higher heat transfer coefficients at the outer wall. Also Moshfeghhian and Bell (1979) observed higher heat transfer coefficient in the downstream of the bend as well as in the bend.

From this characteristic of the heat transfer phenomena in the cooling pipe, a CFX calculation was carried out to obtain detailed information of the fluid velocity and temperature. The calculation simulates the cooling pipe alone and the experimental data of the cooling pipe surface temperature were implemented as boundary conditions. The k-ε model was used for turbulent modeling. Figure 2-16 shows the grid and velocity vectors of the calculation. Figures 2-17 and 2-18 show the calculation results of the velocity and temperature profiles at the temperature measuring locations of the cooling pipe. The centrifugal effect of the bend, which shifts the maximum of the axial velocity toward the outer wall, is well represented in our calculation as shown in Figure 2-19. This is the same trend with the results of Pruvost et. al. (2004) who investigated the flow structure in U-bend using the FLUENT code as shown in Figure 2-20. Also our calculation result for the air temperature at the axis showed a reasonably good agreement with the experimental data. From this calculation results, we concluded that the CFX code can simulate the heat transfer phenomena in the cooling pipe of SNU-RCCS.

As stated above, the assumption for the temperature profile of fully developed turbulent flow was applied for the calculation of the flow averaged mean temperature. To evaluate the assumption, we computed the flow averaged temperatures from the CFX results and compared it with the temperatures calculated by Eq. (2-5) in Figure 2-21. The mean temperature shows about 5% larger values with the assumption than with the CFX predicted results. Even though the assumption does not cause significant distortion of the mean temperature, we will recalculate the heat transfer coefficient of the experimental data applying the velocity and temperature profile of the calculation result. Also more evaluation for other correlations will be carried out and an appropriate correlation will be implemented in the system analysis code such as MARS and RETRAN to simulate the thermal hydraulic behaviors of the SNU-RCCS.

Table 2-1 Measuring parameters and instrumentations.

Measuring Parameters	Measuring Location	Instrumentations
Flow Rate	Cooling Pipe Inlet	Bi-directional Flow Tube
Temperature	Cooling Pipe Axis: 9 Points Cooling Pipe Surface: 7 Points Liquid Temperature: 6 Points	Thermocouples
Differential Pressure	Between Inlet and Outlet	DP Transmitter

Table 2-2 Experimental cases.

Gas velocity	Heat Power (kW)
32 ms/	2.7, 4.0, 5.0
40 m/s	2.7, 4.0, 5.0, 6.0
48 m/s	2.7, 4.0, 5.0, 6,0, 7.0
52 m/s	2.7, 4.0, 5.0, 6.0, 7.0
57 m/s	2.7, 4.0, 5.0, 6.0, 7.0, 8.0

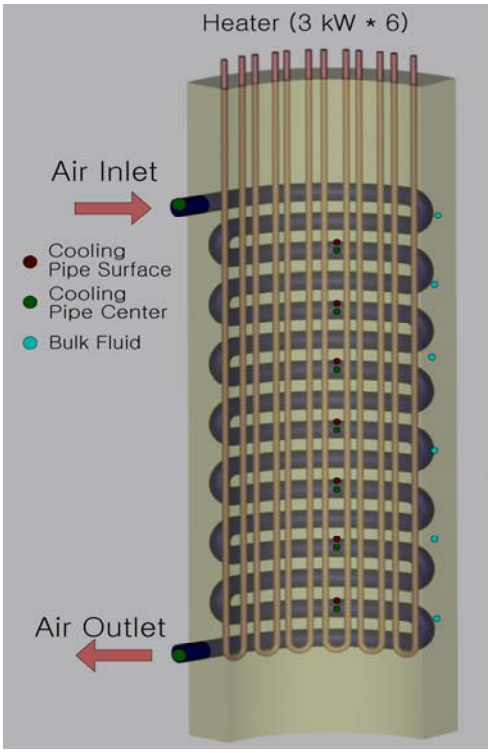

Figure 2-8 Schematic diagram of the separate effect test facility for the SNU-RCCS water tank.

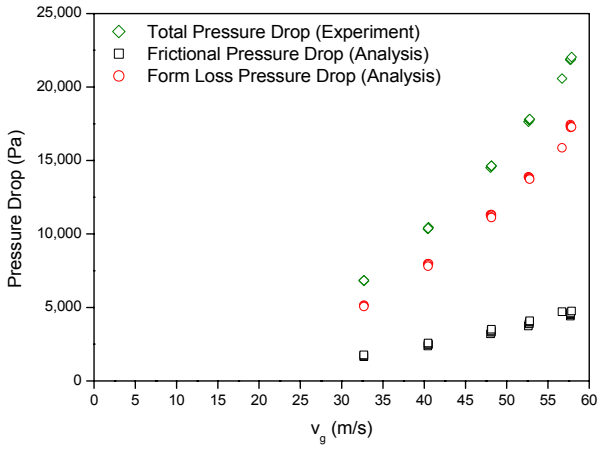

Figure 2-9 Pressure drop.

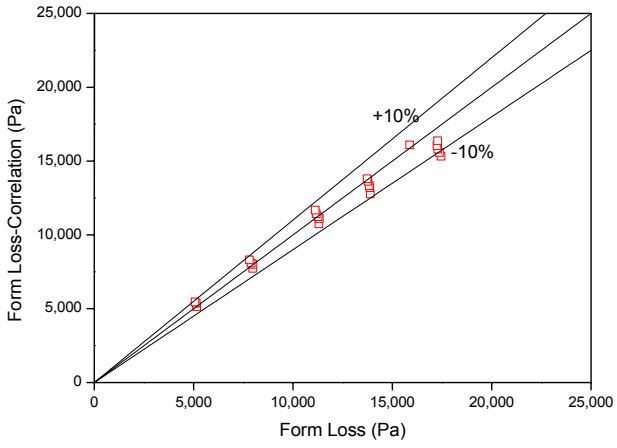

Figure 2-10 Comparison of form loss pressure drop.

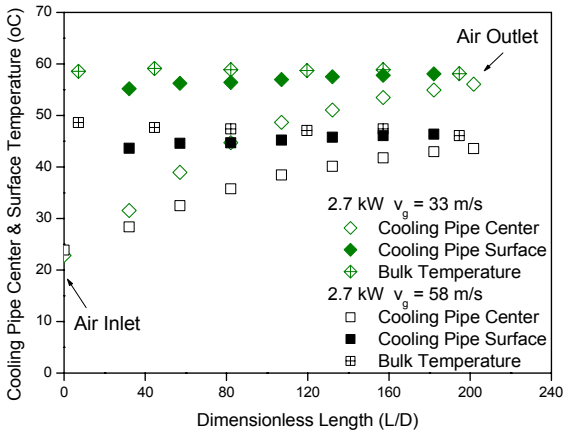

Figure 2-11 Temperature distribution.

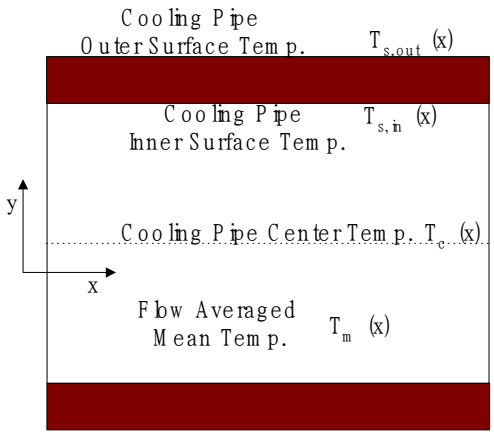

2-12 Control volume of the cooling pipe.

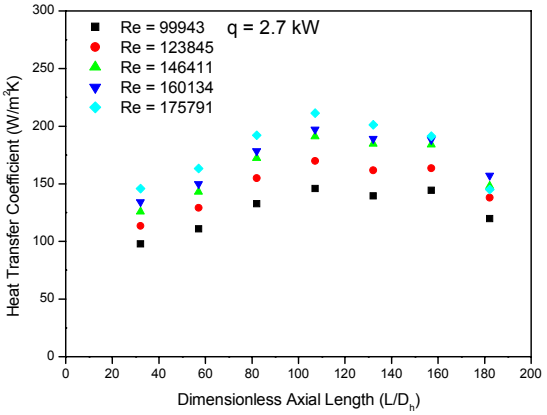

Figure 2-13 Local heat transfer coefficients.

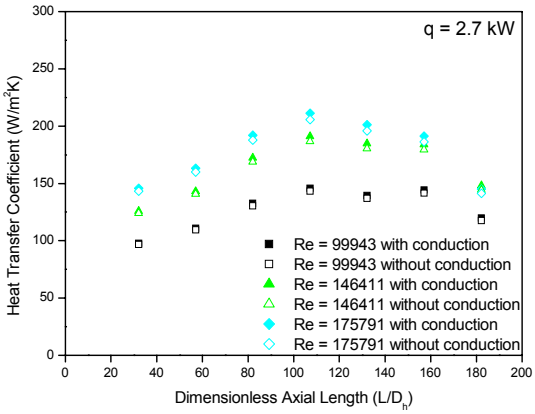

Figure 2-14 Effect of conduction on heat transfer coefficients.

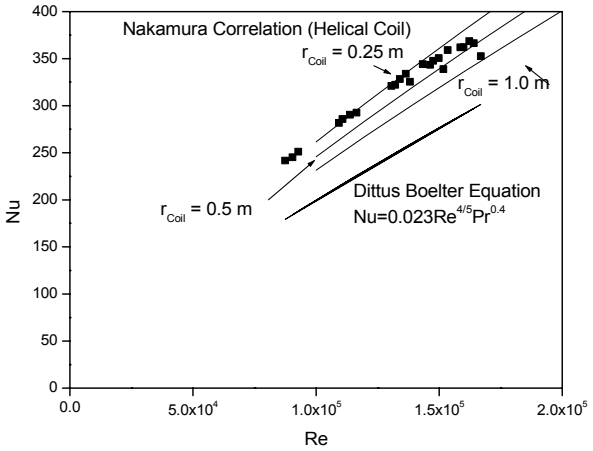

Figure 2-15 Averaged heat transfer coefficient.

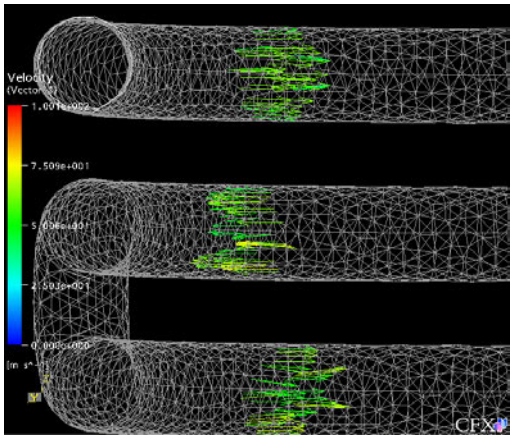

Figure 2-16 Grid and velocity vectors in the cooling pipe.

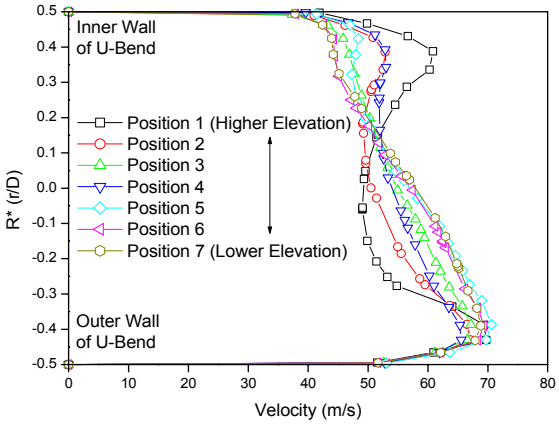

Figure 2-17 Velocity profiles in the cooling pipe.

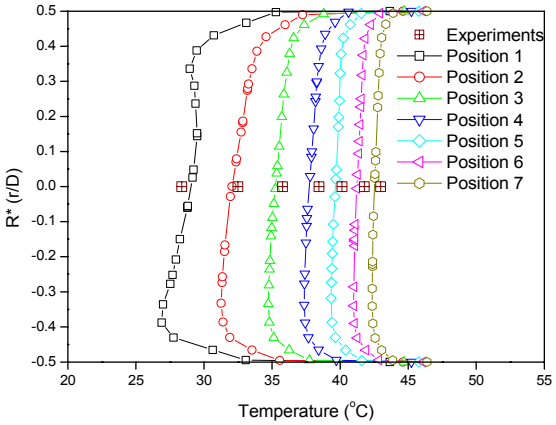

Figure 2-18 Temperature profiles in the cooling pipe.

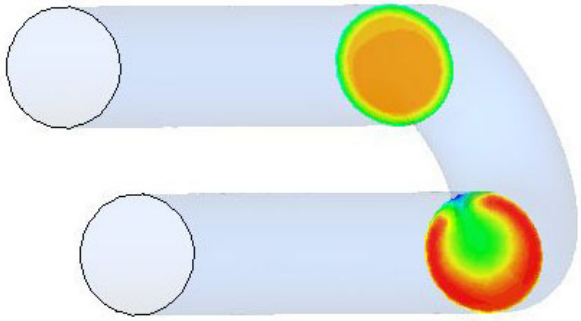

Figure 2-19 Velocity at the inlet and outlet of the u-bend.

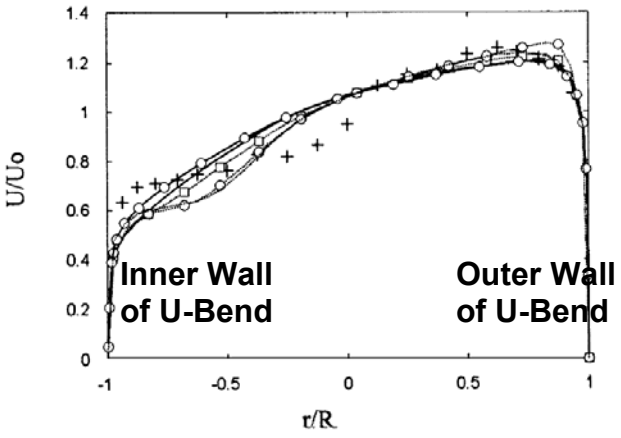

Figure 2-20 Velocity profiles.

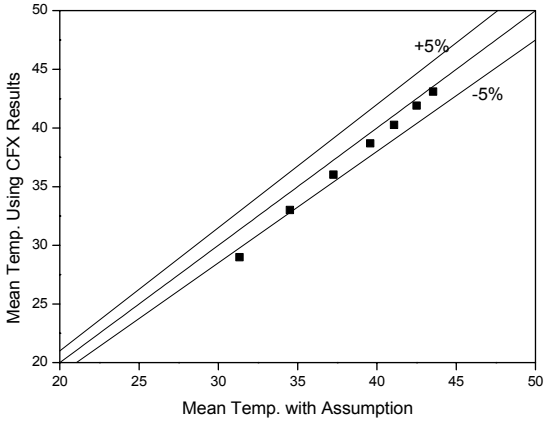

Figure 2-21 Comparison of mean temperature.

Task 2-3 Integral Experiment for the SNU-RCCS

An experimental apparatus was constructed to investigate the heat transfer phenomena in the SNU-RCCS such as natural convection of air and radiation in the cavity, natural convection of water in the water tank and forced convection of air in the cooling pipe. The schematic diagram and the photos of the experimental apparatus are shown in Figures 2-22 and 2-23. The apparatus mainly consists of a reactor vessel, water tank surrounding the vessel, upper tank, cooling pipe and air supply system. The reactor vessel is 1/10 linear scaled model of the PBMR (Pebble Bed Modular Reactor) and it has 1/100 power ratio and 1/1000 volume ratio. In the reactor vessel, six cartridges of heaters were installed to simulate heat loss during normal operation and after heat during the LOFC accident. The heat released from the reactor vessel is transferred to the water tank and the upper tank through the cavity. To remove the heat, thirteen cooling pipes are installed in the water tank and the upper tank (12 in the water tank, 1 in the upper tank) as shown in Figure 2-24. The outlets of the cooling pipes are connected to two common headers and each common header is connected to the suction of two blowers. Ambient air enters in the cooling pipes and takes heat from the water tank and the upper tank. The detail dimension of each component was indicated in Figure 2-25. The major measuring parameters are the air flow rate, pressure drop along the cooling pipe, water level in the water tank and temperatures and the instrumentations and each measuring locations are summarized in Table 2-3. The thermocouples are located at three radial positions, near the inner and outer wall and the center of the water tank. The temperatures of the water tank are measured at three radial positions, five axial positions and three azimuthal positions and additionally three more thermocouples are equipped at the bottom of the water tank.

We plan to perform a series of experiments to investigate heat transfer phenomena in the water pool and the cavity of the SNU-RCCS and evaluate the performance of the cooling system during normal operations and the LOFC accident. The planned experiments for normal operations consist of the normal operation tests to obtain operating characteristics of the RCCS and 1/4 train trip tests to validate the redundancy of the system. Under the LOFC accident conditions, the RCCS has to remove the entire core after heat in the unlikely case of failure or unavailability of the main and all other shutdown cooling systems. Also, the maximum vessel temperature should be within the design criteria for 72 hours without any necessary actions by the operator or controlling equipment. In the LOFC accident experiments, we will evaluate the performance and feasibility of the SNU-RCCS in the emergency condition when the after heat is removed by the water tank alone. Additionally, we will test the effect of the relief valve failure which accentuate the depletion of the water tank and the effect of filling gas on the heat transfer in the cavity. In this report, the typical experimental results for the normal operations are presented.

The normal operation experiments have been performed with the air velocity of 20 m/s, 30 m/s and 40 m/s and the postulated heat loss of 10 kW, 25 kW and 40 kW. Since the power removed by the RCCS was found to be sensitive to the amount of heat loss from the reactor vessel, we have performed the experiments controlling the portion of heat loss that was reported to be 0.3 % in the PBMR, 0.5 % in the GT-MHR and 2 % in the HTR-10 (IAEA, 2000 and IAEA, 2001).

Temperature distributions at the reactor vessel wall and cavity wall were measured in the experiments as shown in Figures 2-26. The reactor vessel wall temperature markedly increases along the axis from the bottom to the middle of the reactor vessel and then keeps approximately constant along the elevation. At the top of the reactor vessel, the wall temperature decreases slightly because the effect of radiative heat transfer from the heater decreases. The similar trend of temperature profile was observed at the cavity wall except sharp increase at the top of the cavity wall where the free surface of the water located. In Figure 2-27, the temperature profiles at the water tank, the cooling pipe surface and the axis of the cooling pipe are presented and they shows the same characteristics with the experimental results of the separate effect tests described in the previous section. The cooling pipe surface temperatures are nearly constant along the elevation and the differences of the bulk liquid temperature between the top and bottom of the water tank are about 3~4^{o}c. The deviations of the liquid temperatures between the inner part and outer part of the water tank are less than 2^{o}C.

This means that the water in the tank is well mixed by natural circulation of water. Comparing the temperatures between the cavity wall and bulk liquid temperature near the water tank inner surface, it seems that large gradients exist like Figure 2-28. The narrow gap between the cooling pipe and heating surface makes the effect of viscous force significant and it reduces the heat transfer of natural convection in that region as same as in the enclosures which have narrow gap and large aspect ratio (Incropera and Dewitt, 1996). Because of the low heat transfer coefficient, the water temperature decreases rapidly at the vicinity of the heating surface.

In Figure 2-29, the heat removal portion of the upper tank is presented and it shows that 13~23 % of the heat loss was removed by the upper tank. Since the heated air at the reactor vessel wall flows upward to the upper part of the cavity by natural circulation, the portion of the heat removal by the upper tank is proportional to that of the natural convective heat transfer. The temperature of the reactor vessel wall rises in keeping with heating power and subsequently it raises the radiation effect on the total heat transfer. As the portion of the radiation in total heat transfer increases, that of natural convective heat transfer is reduced. The portion of heat removal by the upper tank, therefore, decreases with the heating power as shown in Figure 2-29.

For the redundancy of the RCCS the system should be designed to have enough cooling capability although one of four trains of air cooling systems is unavailable. To investigate the temperature distribution in the RCCS under the condition, 1/4 train trip tests were carried out. Figure 2-30 shows the comparison results between normal case and 1/4 trip case that were performed with 20 m/s of air velocity and 40 kW of the heater power. The temperature in the water tank increases about 6~10^{o}C in the trip test but local increase of the temperature was not observed at the non-cooling region and it is concluded that the water in the water pool may be well mixed under the 1/4 trip condition of the air cooling system. As a result of the increase of the water temperature, the cavity and reactor vessel temperatures are raised but it is found that the effect is not significant like Figure 2-31.

These experimental results about the radiative and convective heat transfer will be used for the validation of the system analysis code such as RETRAN and MARS and the GAMMA code that is being developed in KAIST. Also the heat transfer coefficients at the water tank and cooling pipe will be derived from the experimental data and those will be implemented in the system analysis codes.

Table 2-3 Major measuring parameters and locations.

Parameters	Instrumentation	Measuring Location	Quantity
Air Flow Rate	BDFT	Air Inlet	13
Pressure Drop	DP Transmitter	Air In and Out	1
Water Level	DP Transmitter	Water Tank	1
Temperatures	K-type TC (130)	Upper Tank	3
		Water Tank	48
		Reactor Vessel	24
		Cavity Wall	24
		Reactor Vessel for Emissivity	3
		Air In	8
		Air Out	8
		Cooling Pipe Surface	24

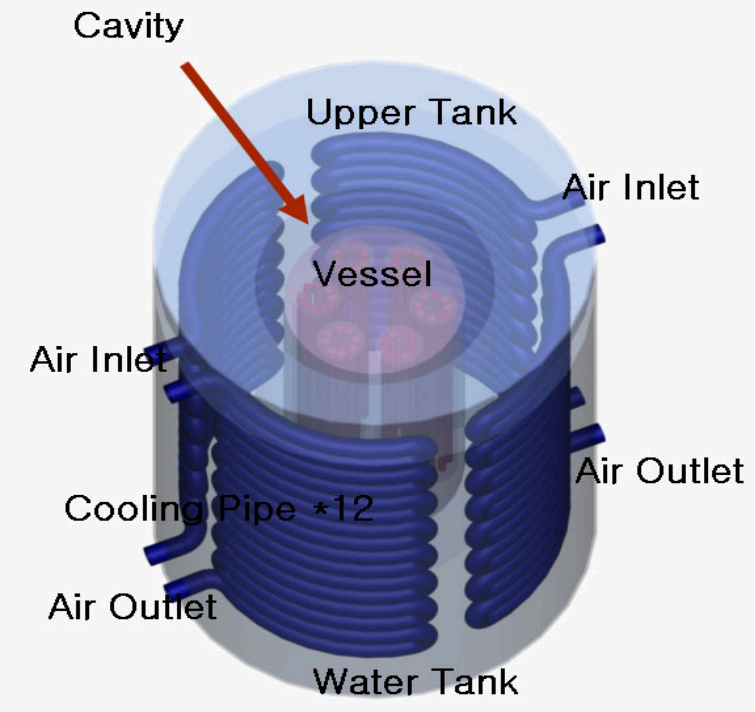

Figure 2-22 Schematic diagram of the test facility.

Figure 2-23 Photograph of the test facility.

(a) Upper tank. (b) Water tank.

Figure 2-24 Configuration of the cooling pipe.

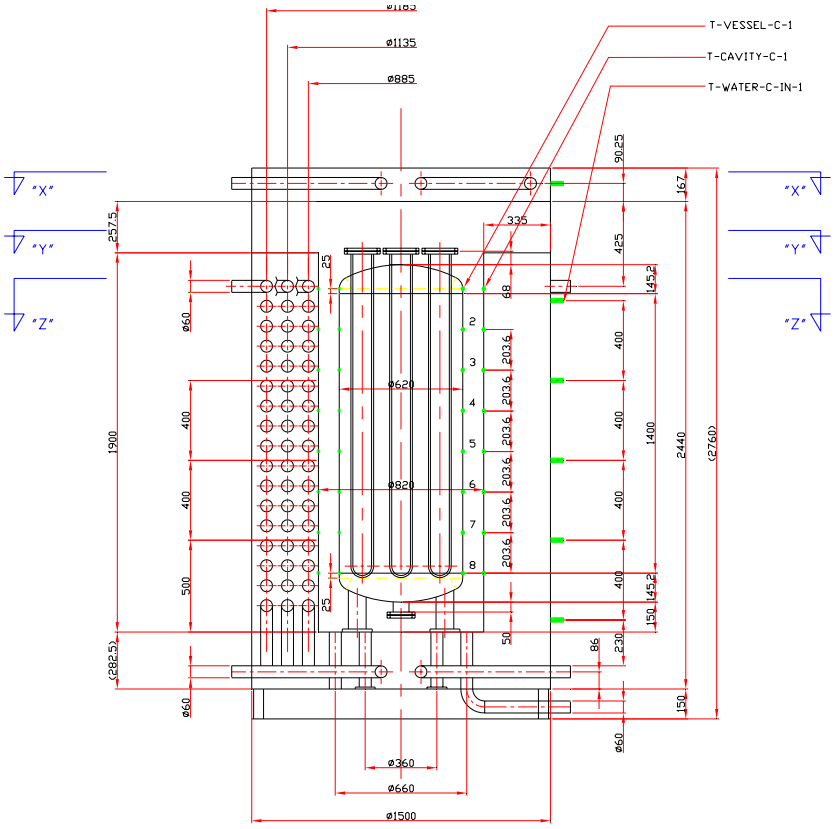

Figure 2-25a Detail dimensions of the test facility (side view).

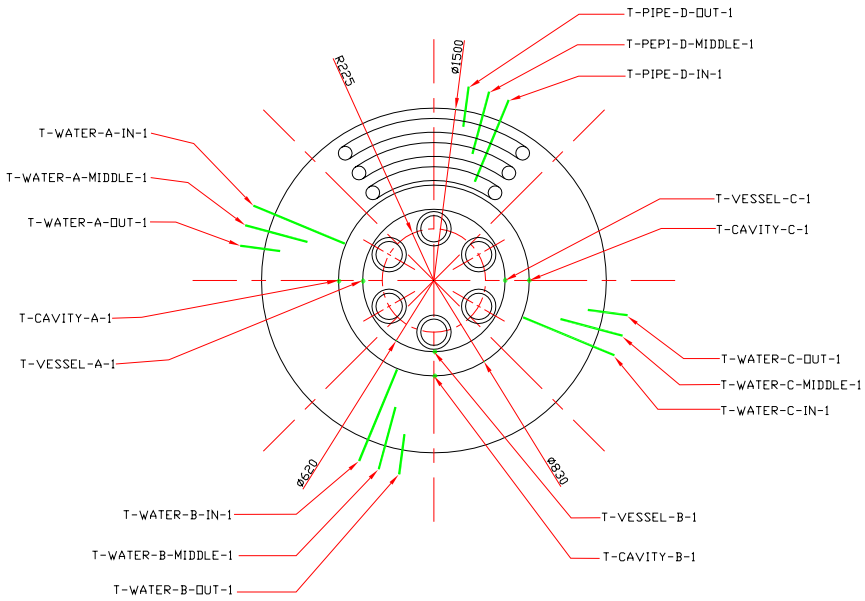

Figure 2-25b Detail dimensions of the test facility (top view).

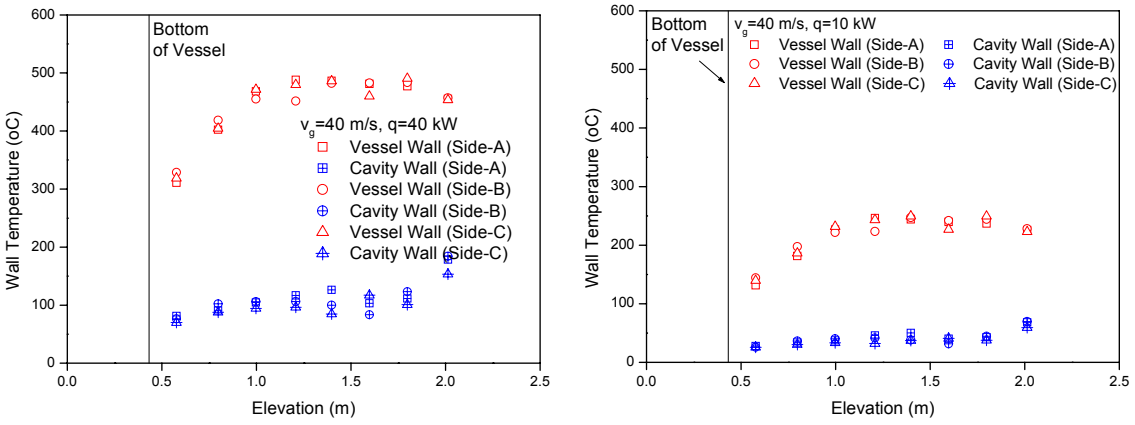

(a) v_g=40 m/s, Q=40 kW (2% Heat Loss). (b) v_g=40 m/s, Q=10 kW (0.5% Heat Loss).

Figure 2-26 Axial distribution of the reactor vessel and cavity temperatures.

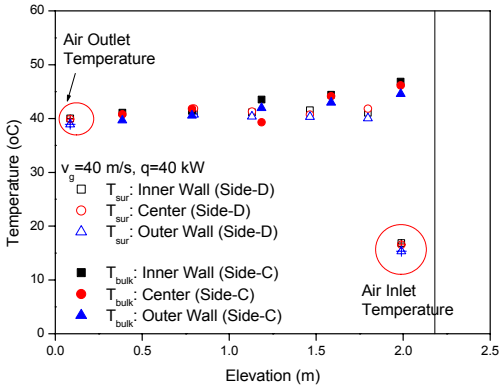

(a) v_g=40 m/s, Q=40 kW (2% Heat Loss).

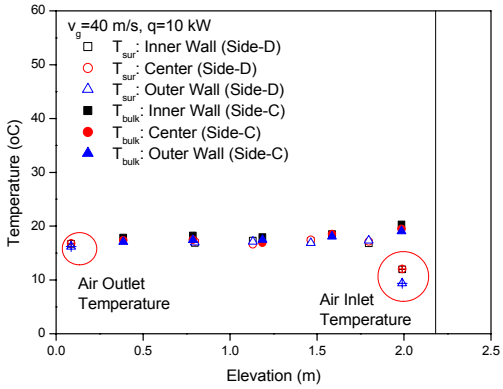

(b) v_g=40 m/s, Q=10 kW (0.5% Heat Loss).

Figure 2-27 Axial distribution of the water tank and cooling pipe surface temperature.

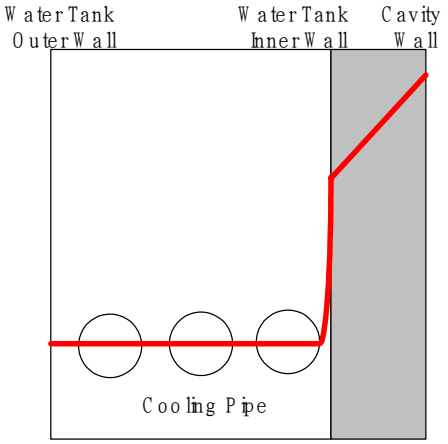

Figure 2-28 Temperature profile near the water tank inner wall.

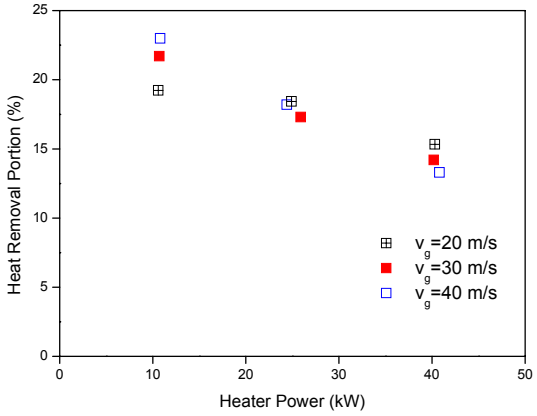

Figure 2-29 Heat removal portion of the upper tank.

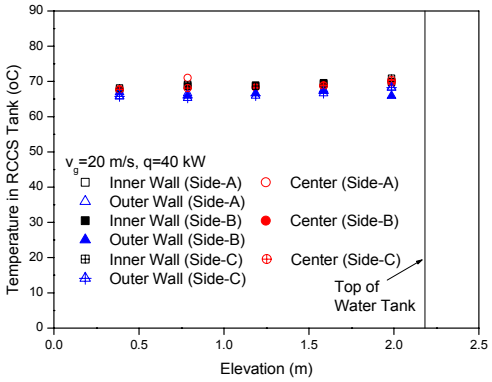

(a) Normal case

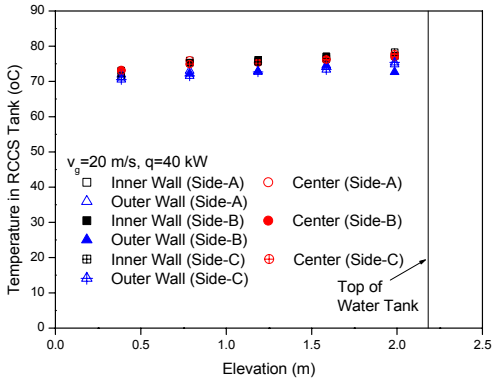

(b) 1/4 train trip

Figure 2-30 Axial distribution of the water tank temperature.

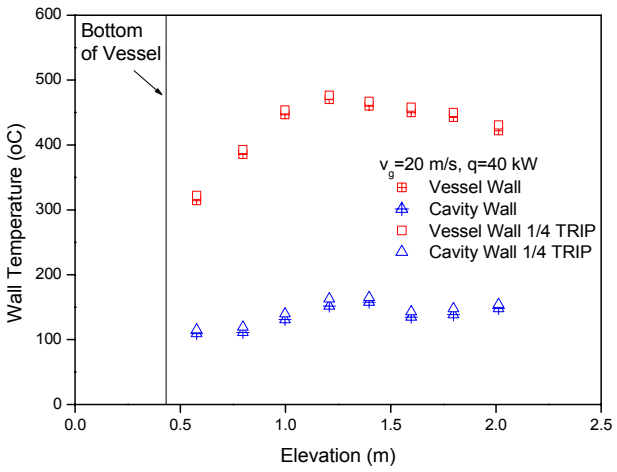

Figure 2-31 Axial distribution of the vessel and cavity temperatures: normal case and 1/4 train trip.

Task 2-4 Code Validation

We consider the RETRAN-3D/INT and MARS codes as analytical tools for the simulation of the SNU-RCCS and the CFX code has been used for the code-to-code validation of the system analysis codes. Code-to-experiment and code-to-code benchmarks have been performed for verification and validation of the analytical methods and analyses using the RETRAN-3D/INT and CFX were conducted for the separate effect test.

The nodalization for the analysis using RETRAN-3D/INT for the separate effect test is shown in Figures 2-32. The analysis model consists of 55 volumes and 74 junctions. It includes the 33 heat structures to simulate the heat transfer phenomena at heater and cooler. In addition, there are cross flow junctions to consider the cross flow between region 1 and 2 in Figure. The inlet of the cooler is modeled using fill junction and the mass flow rate is given as a boundary condition. Zukauskas (1972) and Mori-Nakayama (1967) heat transfer coefficients are used for shell and tube sides of cooler, respectively.

Figures 2-33 compares the experimental data and code calculation results of the water temperature and cooling pipe surface temperature. The calculation results show good agreement with the experimental data of the bulk liquid temperature, however the RETRAN-3D/INT under-predicts the surface temperature of the cooling pipe at the top of the test section. This result is caused by the excessive cooling near the inlet of the cooling pipe and proper local heat transfer coefficient will be implemented after the analysis for the experimental data of the separate effect tests.

To simulate the heat transfer phenomena from the water pool to the cooler and the liquid behaviors in the water tank using CFX calculation, the experimental results of the cooling pipe surface temperature were applied as a boundary condition of the calculation. Figure 2-34 shows the water temperature distribution calculated by the CFX code for the separate effect test. The temperature field and velocity vector near the cooling pipe are indicated in the Figure 2-35. The natural circulation of the water, the upward flow near the hot wall and downward flow near the cooling pipe, was observed in the calculation. The liquid temperature difference between the top and bottom of the test section is about 6^{o}C which is 4.5^{o}C larger than the experimental data. Also the CFX code over-predicts the liquid bulk temperature by 7~10^{o}C as shown in Figure 2-36. It is likely that this difference is affected by the mesh size at the boundary layer near the cooling surface that has the sharp gradient of the liquid temperature as shown in Figure 2-35-(a). The present nodes

near the cooling surface will be divided to make the node size smaller than the boundary layer of the natural convection.

From this calculation, it was found that the exact modeling of the cooling pipe has some problems such as the computation time, mesh limitation and so on. Therefore a simplification of the cooling pipe mesh is necessary for the efficient calculation and we will evaluate the possibility of this approach.

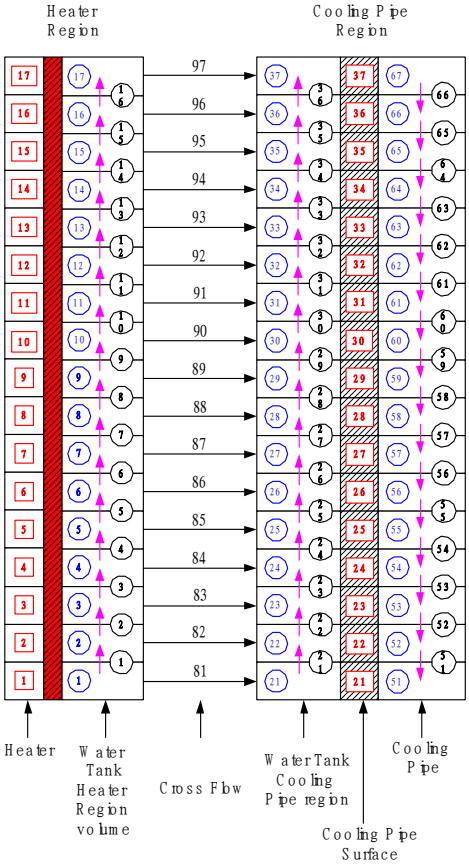

Figure 2-32 Nodalization of RETRAN-3D/INT calculation.

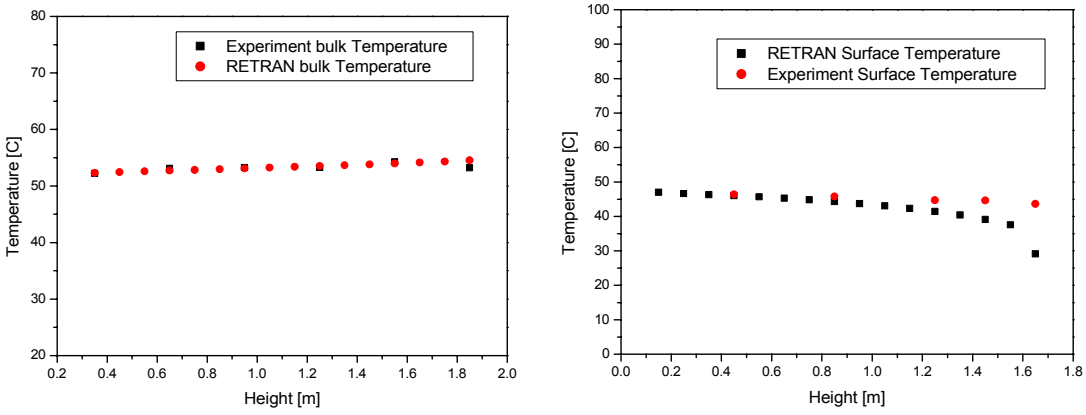

(a) Liquid bulk temperature. (b) Cooling pipe surface temperature.

Figure 2-33 Comparison between experimental data and RETRAN-3D/INT results.

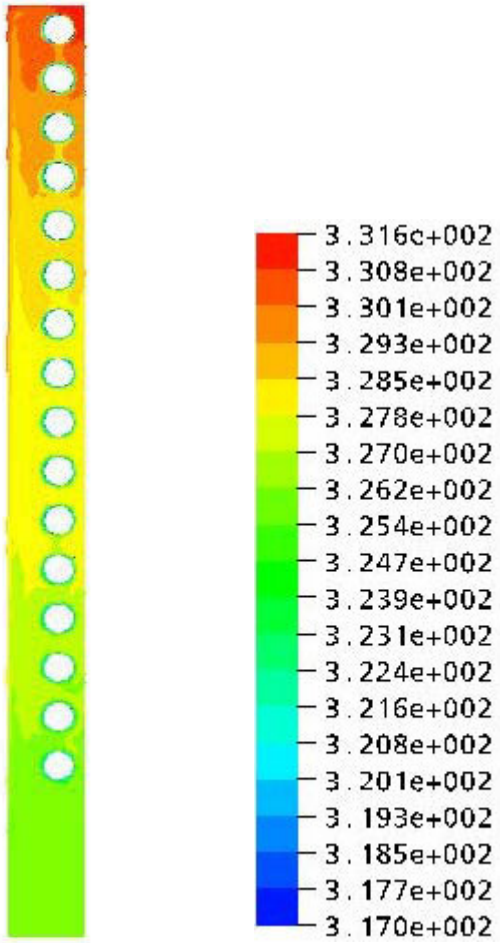

Figure 2-34 CFX calculation result: temperature distribution.

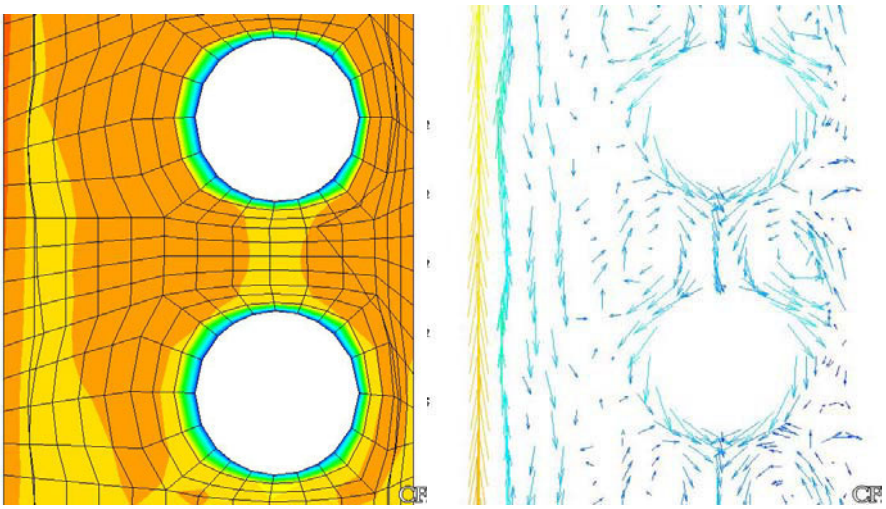

Figure 2-35 CFX calculation result: temperature and velocity vector distribution near the cooling surface.

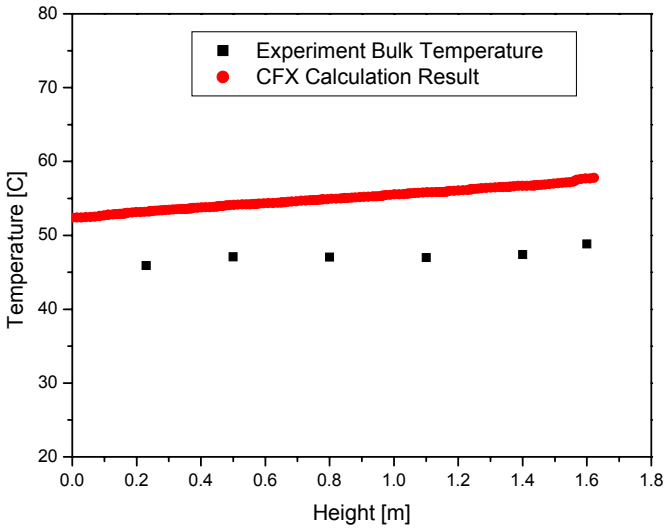

Figure 2-36 Comparison of liquid temperature between CFX calculation and experiment

Next Year Activities

In the next year, we will perform the LOFC accident experiment and the experimental results will be used for the improvement and validation of the thermal hydraulic codes. The validation and assessment of the safety analysis codes such as RETRAN-3D/INT and MARS will continue.

Issues/Concerns

There are neither issues nor concerns.

Task 3: Air Ingress Separate Experiment (KAIST)

Task Status and Significant Results

The objective of this task is to carry out the graphite oxidation experiment, to determine the oxidation-limited model (chemical kinetics-limited, diffusion-limited or in-pore diffusion-limited model), and to develop measurement techniques of the concentration of each species.

The present study investigates the graphite oxidation reaction, which is one of the most serious problems during an air-ingress accident in a high temperature gas-cooled reactor (HTGR). As a first step, the kinetic parameters (activation energy and the order of reaction) of IG-110 were experimentally investigated in a chemical-kinetics limited regime. Figure 3-1 shows the schematic diagram of the experimental facility. In this experiment, we obtained the oxidation rate by gas analysis method. This method offers to have two advantages: (1) faster and more precise response than a general thermo-gravimetric analysis (TGA); and (2) availability of direct analysis for production gas such as CO and CO2.

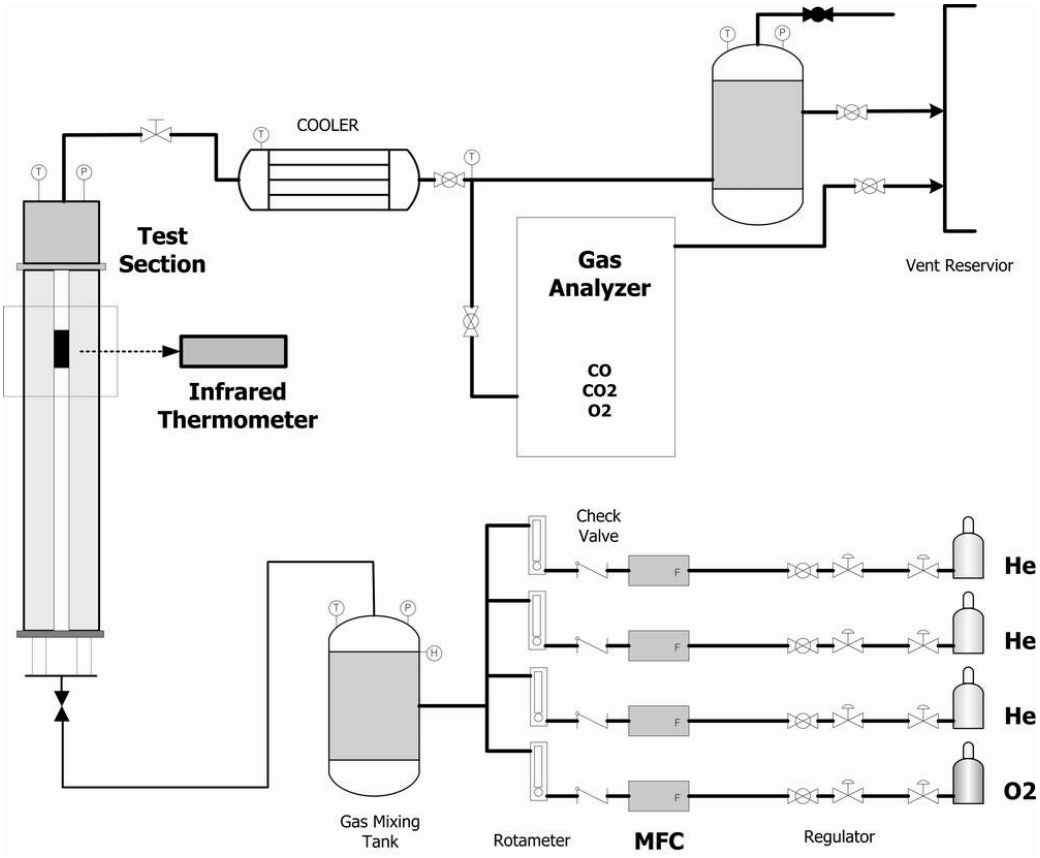

Figure 3-1 Schematic diagram of experimental facility.

Figure 3-2 shows the test section of this experiment. The test section has a cylindrical shape and is made of a quartz tube. In order to maintain a hydraulically fully-developed flow during the test, a long test section was designed. This design gave us a well-known flow field (Hagen-Poiseuille flow) around the surface of the test specimen. The specimen was installed in the center of the test section and a ceramic rod supported it. An induction heater was used for heating the sample and its temperature was measured by a non-contact measurement technique using two infrared thermometers (IRtex Raymatic 10, Raytec Ranger 3i). Setting temperature could be achieved within 30sec by the induction heating method without disturbing the gas flow field.

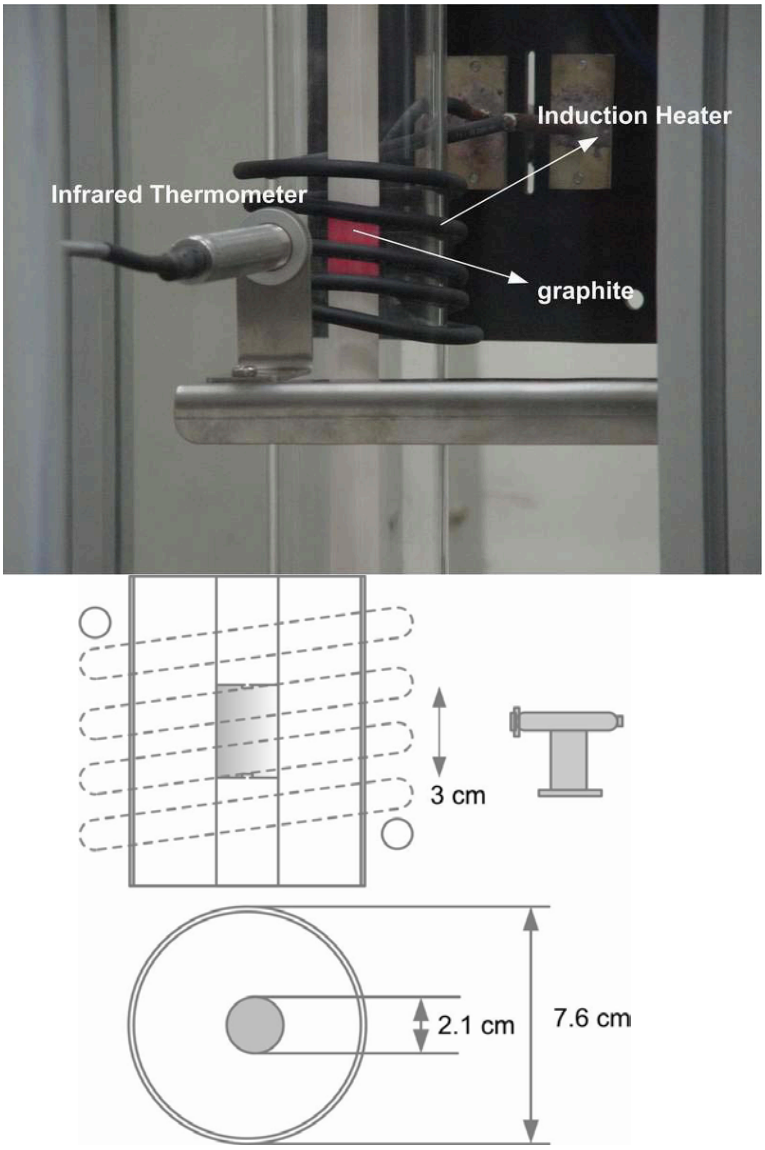

Figure 3-2 Test section of the kinetic parameter measurement experiment.

In order to obtain the activation energy (Ea), we measured the reaction rate at different temperatures. We have performed a total of 33 tests at different conditions, and the results are illustrated in Figure 3-3. Our results can be summarized as follows:

- Ea = 218.43±3.76 kJ/mol within a 95% level of confidence.
- Ea is not affected by oxygen concentration, as Hinsen [1983] shows.
- Ea is not affected by the characteristics of fluid dynamic conditions.

In order to obtain the order of reaction (n), we measured the reaction rate at different oxygen concentrations. We have performed a total of 66 tests at different conditions and the results are summarized in Figure 3-4. The final results are as follows:

- n = 0.75±0.146 within a 95% level of confidence,
- n is not affected by burn-off,
- n is not affected by temperature, as Lewis [1965] and Hinsen [1983] show.

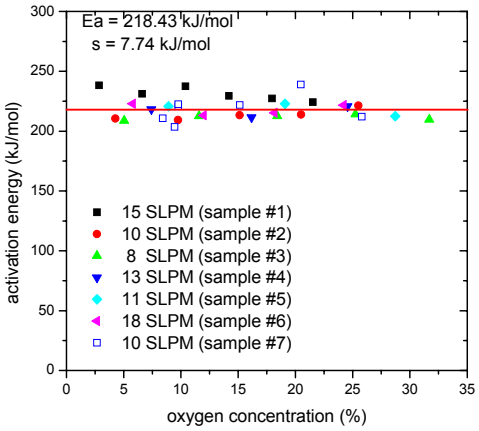

Figure 3-3 Results of activation energy (Ea).

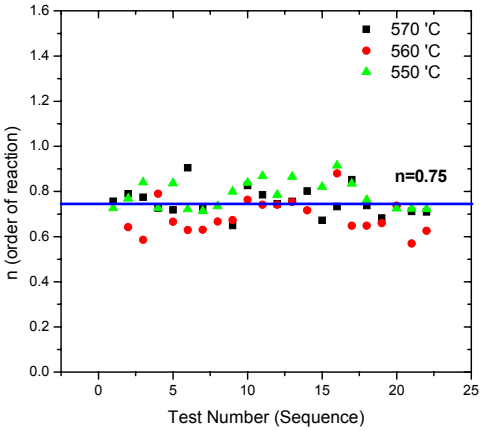

Figure 3-4 Results of order of reaction (n).

For analysis of the chemical reaction in an air-ingress accident, the initial reaction rates and CO/CO2 were measured in a temperature range of 700 to 1500 °C and an oxygen concentration of less than 20%. Figure 3-5 and Figure 3-6 show the reaction rate and the CO/CO2 ratio respectively. Figure 3-5 shows that the reaction rate increases with temperature at a low temperature regime and is saturated at high temperature. The main reason for the saturation is that the chemical reaction rate is limited by mass transfer at high temperature.

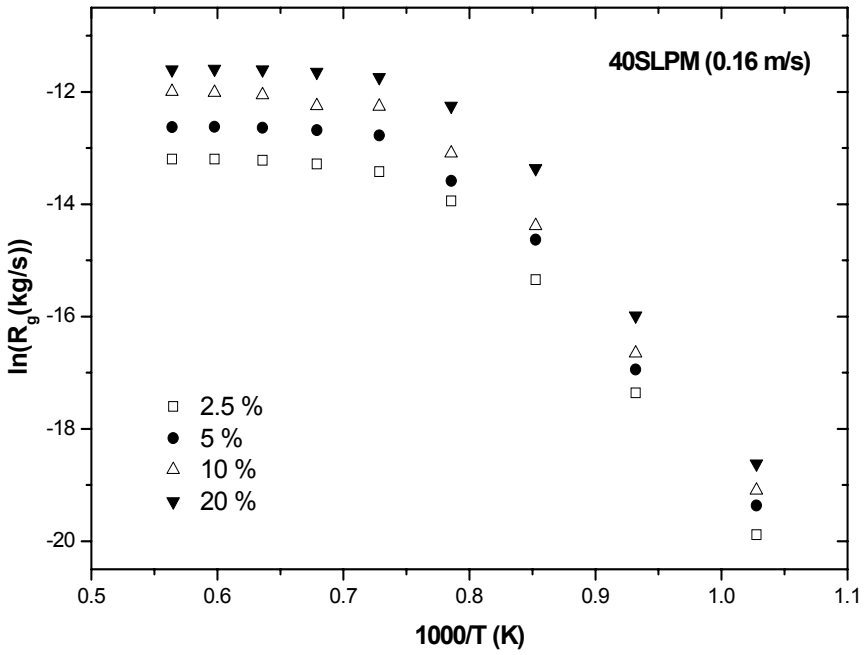

Figure 3-5 Results of oxidation rate.

Figure 3-6 shows the experimental results of CO/CO2 ratio. In this graph, our data and Takahashi's data [1994] are included. Takahashi experiment was performed with the same graphite material as ours. We developed the following empirical correlation for IG-110 graphite as the previous researcher's approach:

$$f_{CO/CO2} = 7396 \exp(-\frac{69604}{R\,T}) .$$

We did not consider the oxygen concentration effect in this correlation because this effect was not observed in our experiment as shown in Figure 3-6.

The above correlation has an applicable range covering air-ingress accident conditions of HTGR and it yields good predictions within 10 % deviation of the experimental data.

A Computational Fluid Dynamics (CFD) simulation was conducted and compared to the experimental data using the oxidation parameters and the CO/CO2 ratio developed here. Figure 3-7 shows the mesh of this simulation. Figure 3-8 shows a comparison between the predictions and data. This graph shows that the calculation results are in good agreement with the experiment. This indicates that, if we provide accurate chemical kinetic parameters and an accurate model for the relative fraction of CO and CO2 gases, we can accurately predict the reaction rates as well as thermal-hydraulic variables for the whole range of temperature and oxygen concentration using the CFD code.

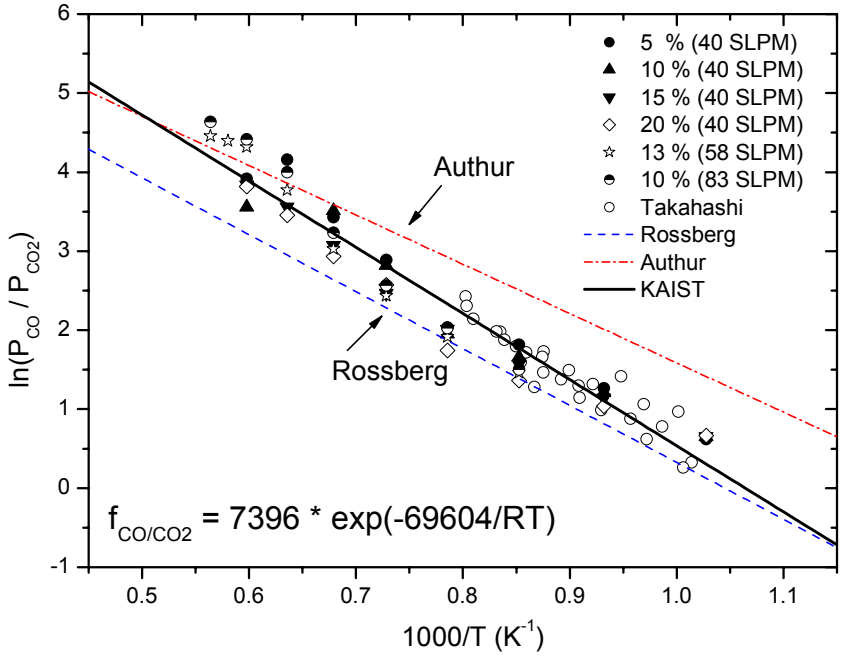

Figure 3-6 Results of CO/CO2 ratio.

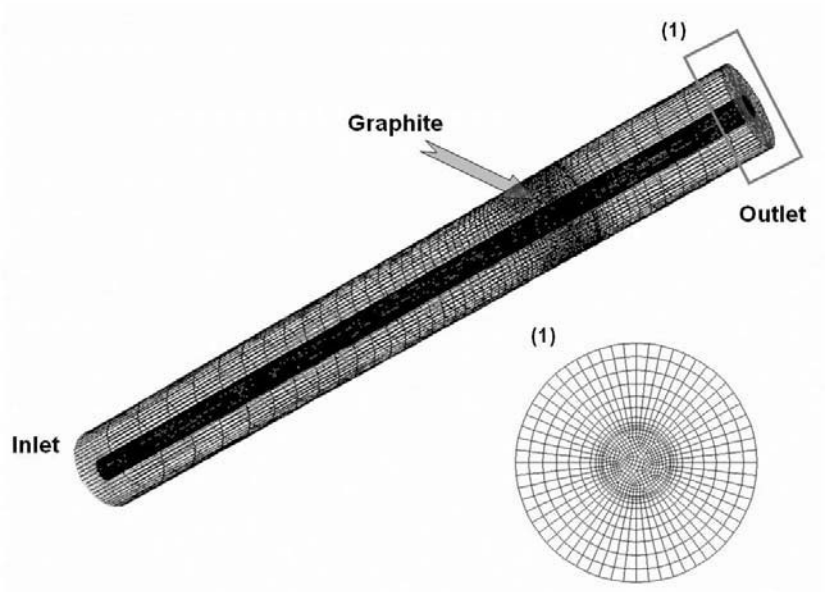

Figure 3-7 Mesh of CFD simulation.

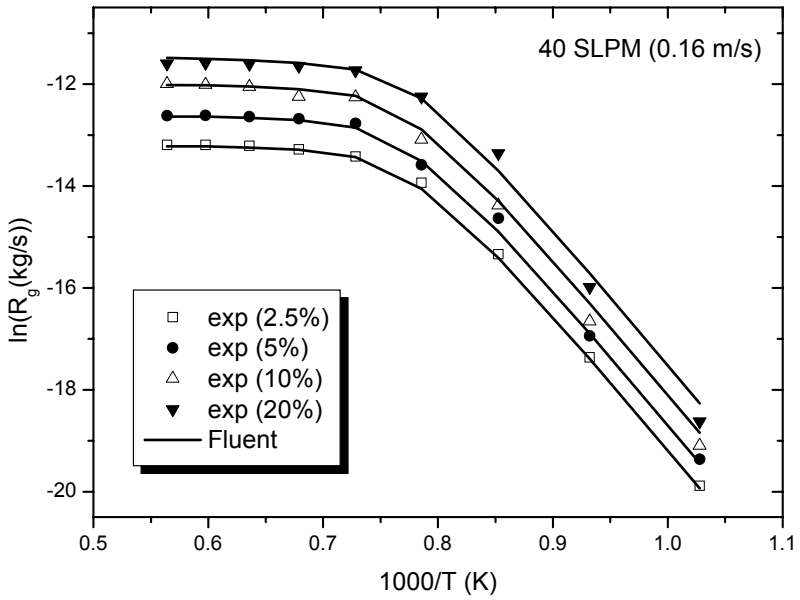

Figure 3-8 Comparison of CFD simulation with experimental results.

Using a CFD simulation, we can calculate the reaction rate for various conditions and geometries. However, in actual applications, we use a system tool rather than a CFD tool, because the latter requires excessive computing time as too many meshes and time steps are required for a transient analysis. As the system tool uses a coarse mesh scheme, we need a correlation-type model for prediction of the chemical reaction. In the present study, we derived the general equation without the limitation as follows:

$$\frac{1}{R_g} = \frac{1}{R_{mb}} + \frac{1}{R_{cb}},$$

where

$$R_{mb} = K_m \cdot C_b \cdot A,$$

$$R_{cb} = K_0 \cdot e^{-\frac{Ea}{R \cdot T}} \cdot P_{O2,b}{}^{n} \cdot A \quad (n \neq 0),$$

where

R_g = graphite oxidation rate (kg/s)

R_{cb} = asymptotic chemical reaction rate(kg/s)

R_{mb} = asymptotic mass transfer rate (kg/s)

K_m = $M_c \cdot (2f_{CO/CO2} + 1)/(f_{CO/CO2} + 1) \cdot k_m$ (kg m/mol s)

k_m = mass transfer coefficient (m/s)

C_b = bulk oxygen concentration (mol/m^3)

R = gas constant

T = temperature (K)

A = apparent surface area (m^2)

$P_{O2,b}$ = oxygen pressure in bulk flow (atm)

We compared the results calculated by the above equation with the experimental results. The combination of correlations used for this calculation is summarized in Table 3-1. Arrhenius equation and heat/mass transfer analogy were used as a chemical reaction and a mass transfer correlation, respectively. Since the flow was not fully developed for diffusion, the entrance effect was considered. We also corrected the high mass transfer effect. Figure 3-9 provides a comparison between the correlation and the experiment. We used two options for the prediction of the diffusion coefficient in the calculation: a binary diffusion coefficient and an effective diffusion coefficient. An effective diffusion coefficient for the mass transfer calculation produces better predictions than a binary diffusion coefficient does.

Table 3-1 Graphite oxidation model and correlations.

Total Reaction Rate	$\frac{1}{R_g} = \frac{1}{R_{mb}} + \frac{1}{R_{cb}}$
Chemical Reaction Rate	1. General Arrhenius Equation $R_{cb} = K_0 \cdot e^{-\frac{Ea}{R \cdot T}} \cdot {P_{O2,b}}^n \cdot A$
Mass Transfer Equation	2. General Mass Transfer Equation $R_{mb} = K_m \cdot C_b \cdot A$ a. Heat/Mass Analogy b. Entrance effect correction (Greatz solution) $Sh = \frac{k_m \cdot d}{D} = 3.66 + \frac{0.0668(d/x) \cdot (\mathrm{Re} \cdot Sc)}{1 + 0.04 \cdot [(d/x) \cdot (\mathrm{Re} \cdot Sc)]^{2/3}}$ c. High Mass Transfer correction $\theta = \frac{\ln(B_{m1} + 1)}{B_{m1}}$ d. Effective diffusion coefficient $D_{1m} = \frac{(1 - f_1)}{\sum_{i=2}^{n} (f_i / D_{1i})}$

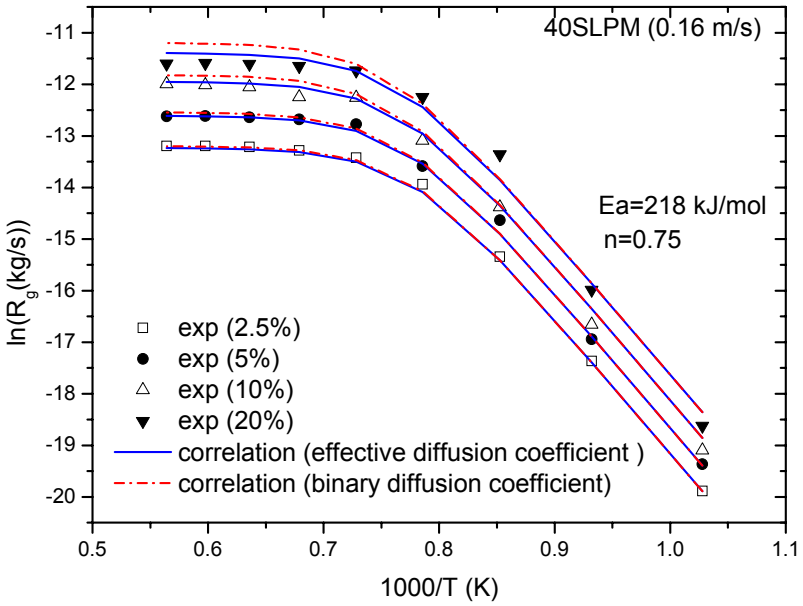

Figure 3-9 Comparison of correlation with experimental results.

To estimate mass transfer effect and confirm the heat/mass transfer analogy, we designed and manufactured another experimental facility. Figure 3-10 shows the test section of the facility.

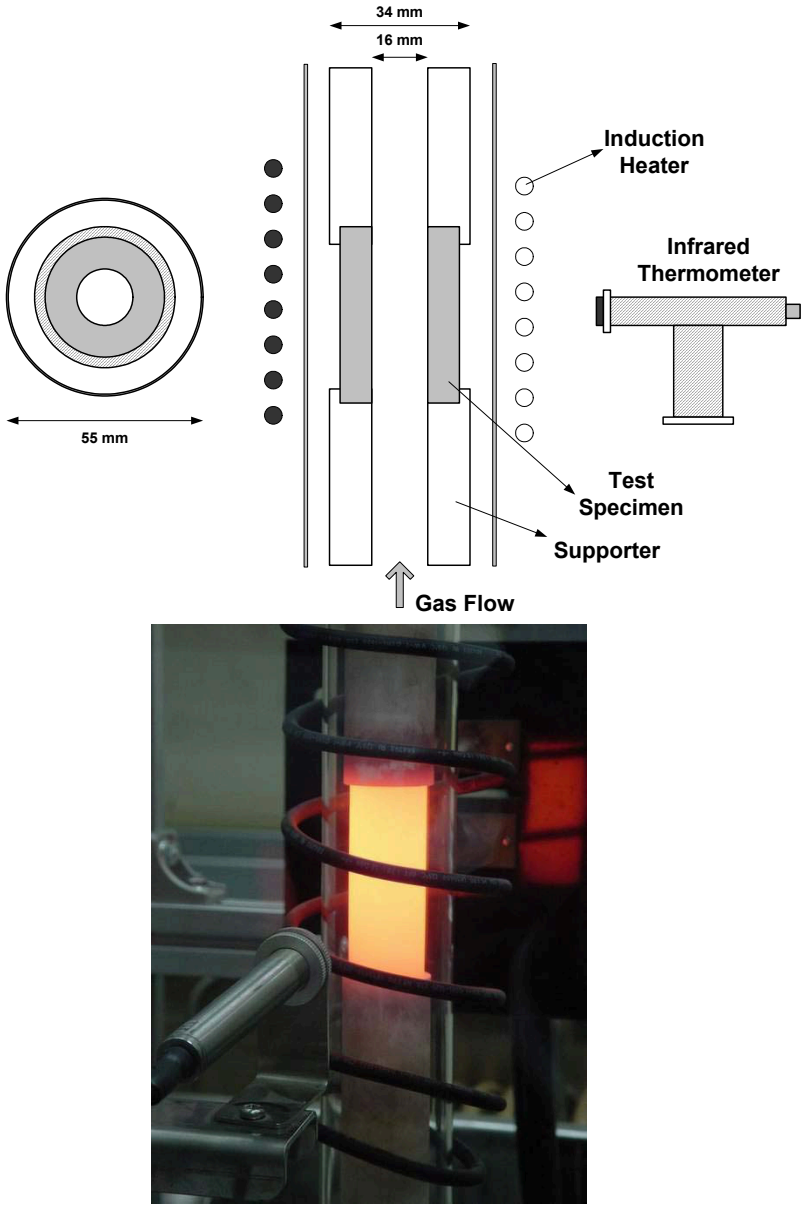

Figure 3-10 Test section of the annular channel experiment.

It was designed as an annular channel. The diameter of the channel was 16 mm and it has the same hole diameter as the GT-MHR core. This test was performed for 5 different lengths to estimate the entrance effect. The reaction rate was measured at different velocities. Figure 3-11 shows the experimental results. This test will be carried out for more cases for analysis.

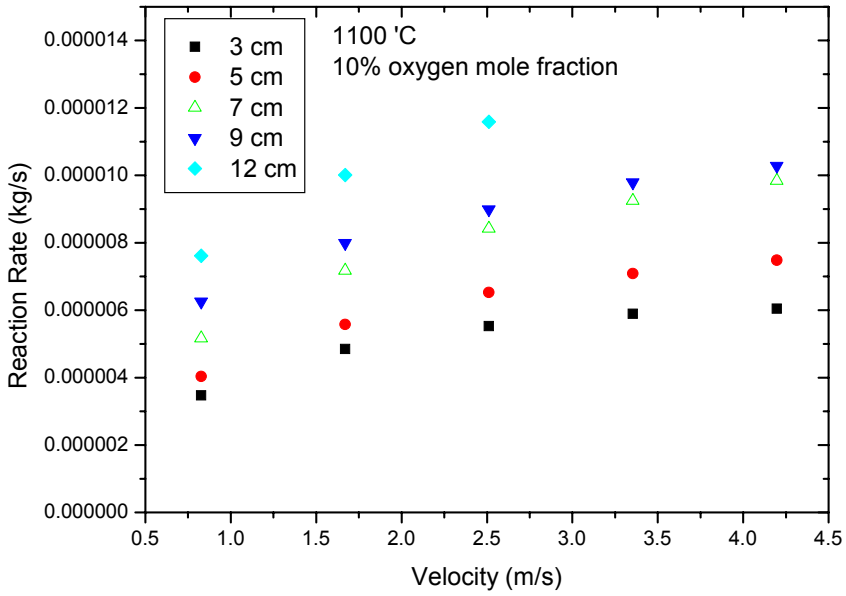

Figure 3-11 Results of the annular channel experiment.

The separate experimental facility for the effects of geometry and size was designed and manufactured. The objective of this experiment is to generalize our small scale experimental data to the full scale nuclear reactor. Figure 3-12 shows the facility. In this experiment, the reaction rate is directly measured by a balance. The furnace was heated by electric heater at 600 ℃ and the temperature was measured by ceramic-sheathed thermocouple. Natural air was used for reacting fluid and it was filtered and dehumidified before entering the test section. The flow rate was 1 SLPM and it was controlled by the mass flow controller.

Before entering the quantitative analysis, we estimated which one is more effective between internal reaction of the material and external surface reaction. Figure 3-13 shows the main idea of this test. As the sample changes from left to right, the volume of the sample decreases and its area increases. Therefore, if the reaction rate of the left sample is larger than the right one, it means that the internal reaction is more effective parameter. Conversely, if the reaction rate of the left sample is smaller than the right one, it means that the external surface reaction is more effective. Figure 3-14 shows the type of geometries used in our experiment. Figure 3-15 shows the sample results. As shown in this figure, the reaction rate of the left sample is larger than the right one. So we can conclude that the internal reaction is more effective than the surface reaction. Some data is illustrated in Figure 3-16. In this figure, we can find that volume effect is more related to the oxidation rate than surface effect. This experimental work is now in progress. So, for quantitative analysis and modeling, more experimental data and further study is necessary.

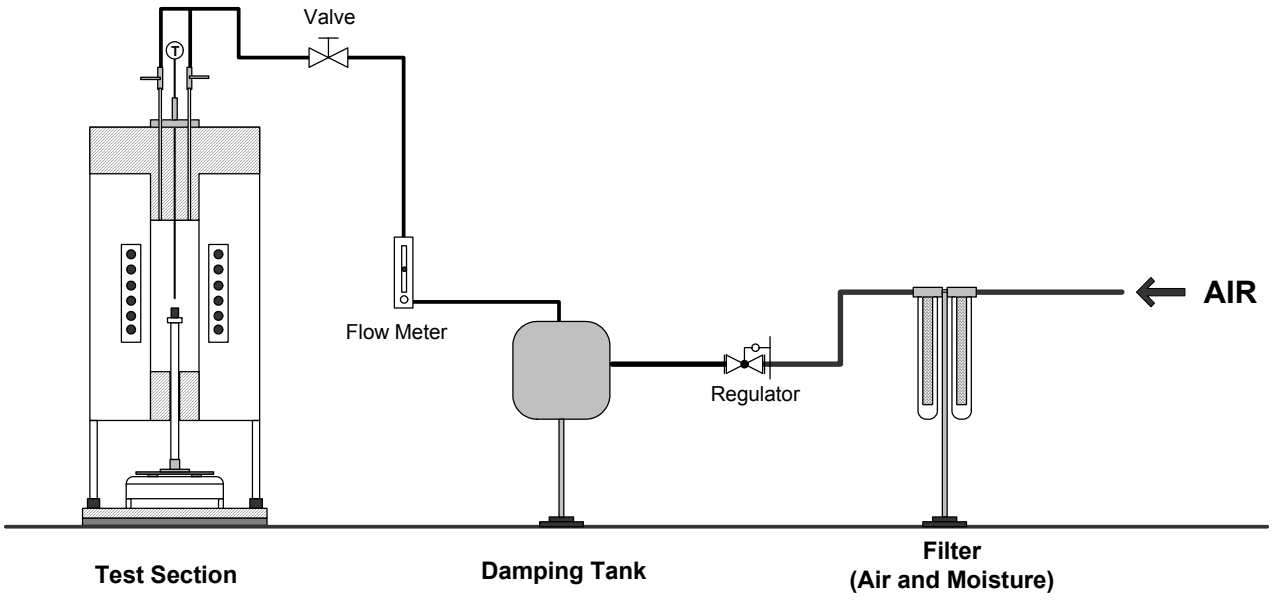

Figure 3-12 Experimental facility for geometry and size effect.

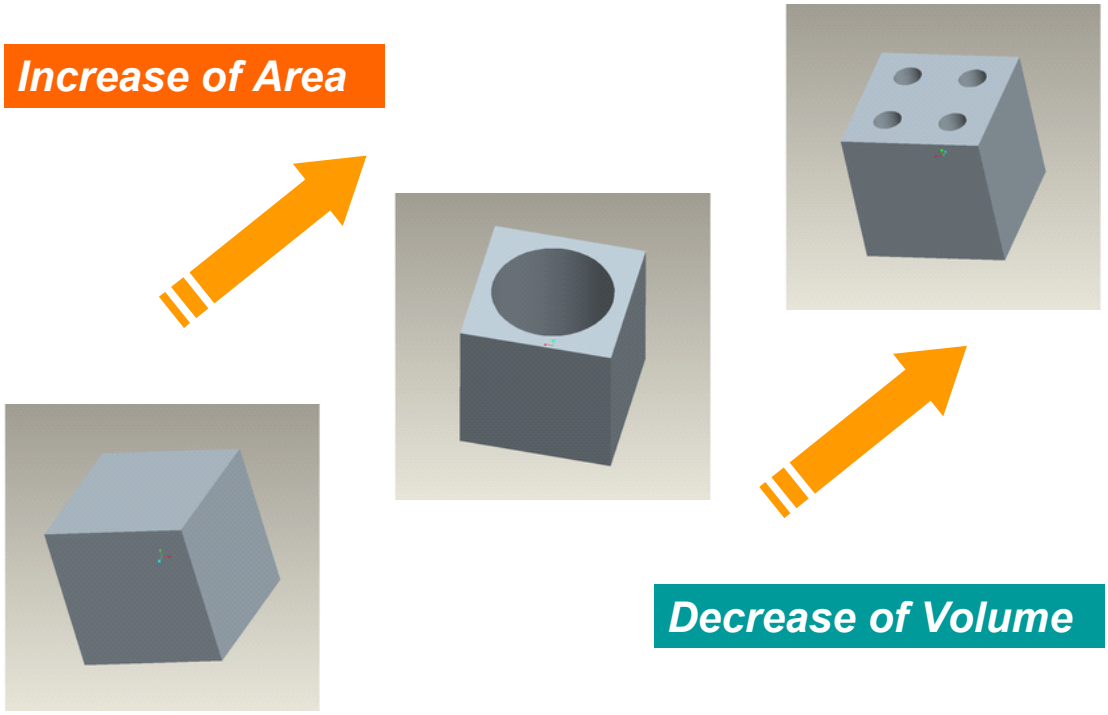

Figure 3-13 Main idea of the geometry and size effect test.

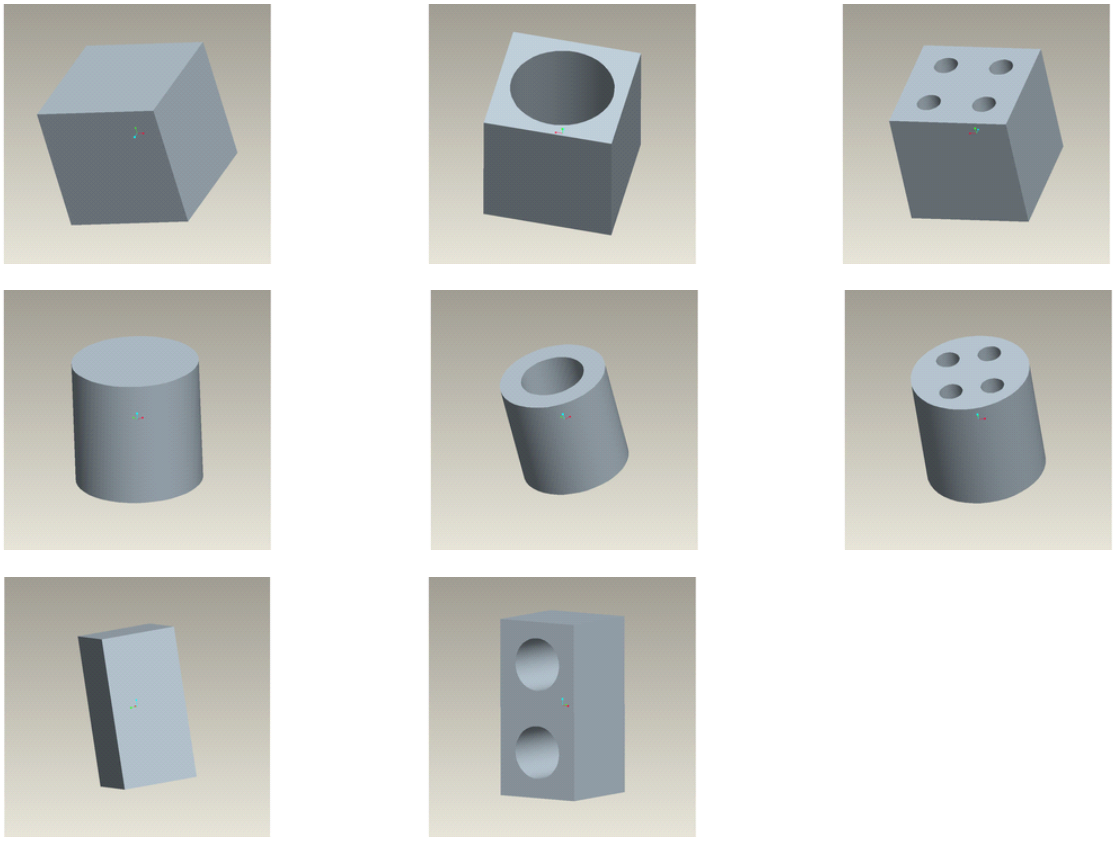

Figure 3-14 Type of geometries.

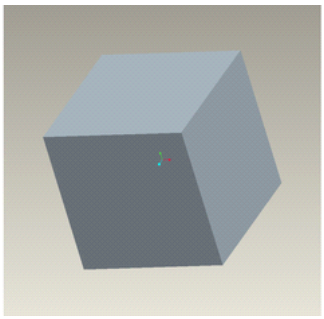

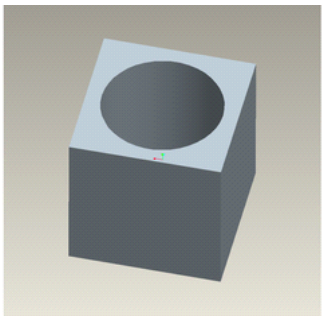

25 X 25 X 25 mm

25 X 25 X 25 (D=15) mm

Volume = 15625 mm³	**>**	**Volume = 7771 mm³**
Area = 3750 mm²	**<**	**Area = 4693 mm²**
Reaction Rate = 6.38e-4 g/min	**>**	***Reaction Rate = 3.78e-4 g/min***

Figure 3-15 Sample results of qualitative geometry test.

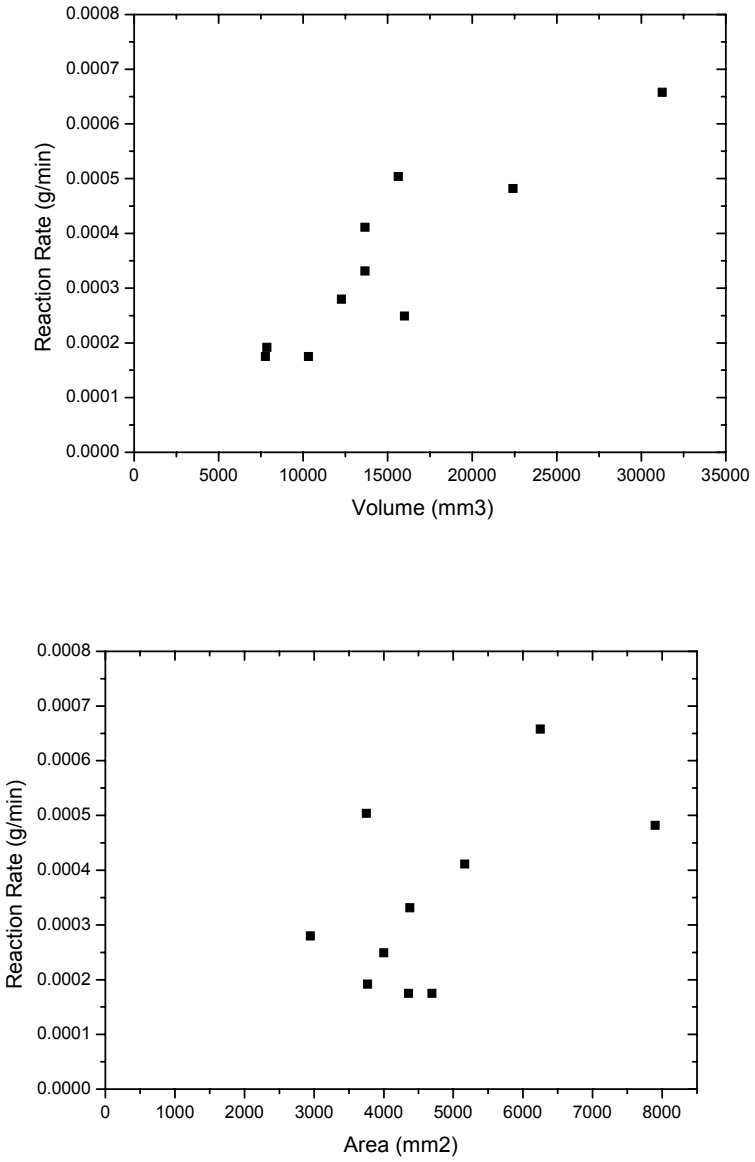

Figure 3-16 Results of geometry effect test.

Next Year Activities

The experiment and analysis for geometry and size effect will be performed in the next year. From those experimental results, the model for normalization factor will be made. For analysis of the annular channel experiment, heat/mass transfer analogy will be confirmed. Moisture effect and burn-off effect will be experimentally investigated.

Issues/Concern

No issues or concerns

Task 4: Improvement of System Codes (INEEL)

The RELAP5-3D (RELAP5-3D Code Development Team 2003) computer code is being improved for the analysis of very high temperature gas-cooled reactors. Following a loss-of-coolant accident, flow through the reactor vessel may initially stagnate due to a non-uniform concentration of helium and air. However, molecular diffusion will eventually result in a uniform concentration of air and helium. The difference in fluid temperatures within the reactor vessel may then establish natural circulation that can supply significant amounts of air to the reactor core. The heat released by the resulting oxidation of graphite in the core has the potential to increase the peak cladding temperature. In order to analyze the effects of oxidation on the response of the reactor during accidents, a molecular diffusion model was added to an experimental version of RELAP5-3D. The model is based on Fick's Second Law for spatially uniform pressure and temperature. The binary diffusion coefficients are obtained from the correlation of Fuller et al. from Reid et al. (1987).

Diffusion and natural circulation are important phenomena during a loss-of-coolant accident in very high temperature gas-cooled reactors. The capability of RELAP5-3D to represent both phenomena was assessed. The diffusion model was assessed using data from inverted U-tube experiments (Hishida and Takeda 1991). The code capability to simulate the natural circulation of air through a pebble bed was assessed using data from the NACOK facility (Kuhlmann 2003). Both assessments are described in detail below.

Assessment of the Molecular Diffusion Model

The experimental apparatus of Hishida and Takeda (1991) is shown in Figure 4-1. The apparatus consisted of an inverted U-tube, ball valves, and a tank. The inner diameters of the U-tube and the tank were 0.0527 and 1.0 m, respectively. The heights of the U-tube and tank were 1.45 and 0.5 m, respectively.

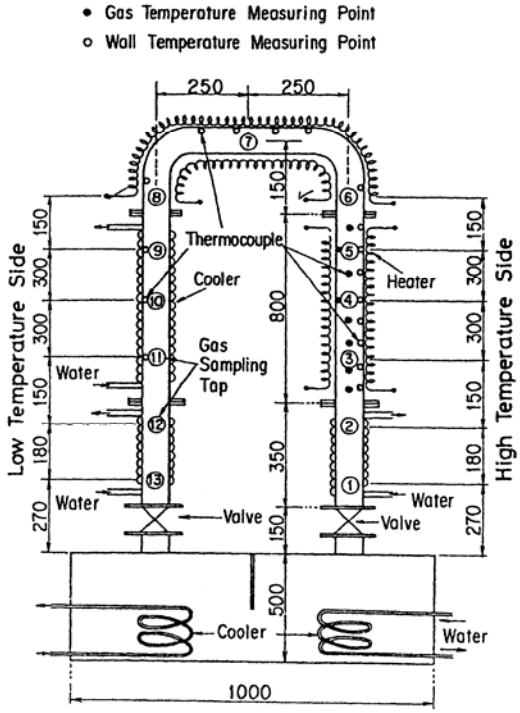

Figure 4-1 Inverted U-tube experimental apparatus (from Hishida and Takeda (1991)).

The ball valves that separated the inverted U-tube from the tank were closed before the start of the test. The tank and the inverted U-tube were then evacuated and filled with nitrogen and helium, respectively.

Electrical heaters controlled the fluid temperatures of one vertical leg and the horizontal leg at the top of the inverted U-tube. The temperature of the other vertical leg was controlled by external cooling with water. After the temperatures had stabilized, the pressures in the tank and inverted U-tube were adjusted to match atmospheric pressure. The test was initiated by opening the ball valves, which allowed nitrogen to diffuse from the tank upwards through the U-tube. The mole fraction of nitrogen was measured at several locations in both legs of the inverted U-tube. The uncertainty in the mole fraction measurement was 5%. Two tests were conducted; one utilized isothermal conditions at room temperature, while the other utilized a non-isothermal profile with values varying between 18 and 256°C.

A RELAP5 model of the inverted U-tube was developed as illustrated in Figure 4-2. The model represented the inverted U-tube, ball valves, and tank components. The tank was divided into two halves, with a connecting junction at the bottom, because the experimental version of the diffusion model does not currently allow more than one junction to be connected at each face of a control volume. Heat structures were used to simulate the walls of the inverted U-tube and the tank. The temperatures of the outer surface of the heat structures were set at the measured values. The RELAP5 model shown in Figure 4-2 is much more detailed than typical reactor models and consists of 144 control volumes, most of which are 2.45 cm long. The nodalization is similar to that used previously by Hishida and Takeda (1991) and Lim and No (2003).

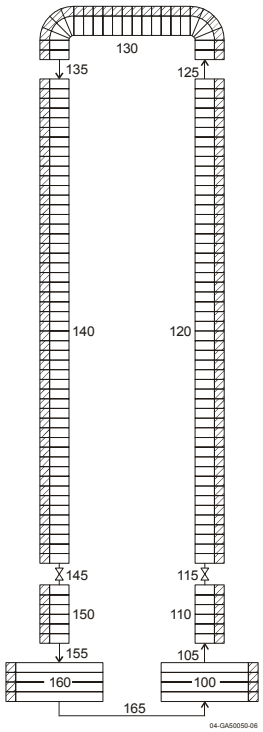

Figure 4-2 RELAP5 model of the inverted U-tube experiment.

RELAP5 calculations were performed for both the isothermal and non-isothermal experiments. Results for the isothermal experiment are presented in Figure 4-3. The figure shows measured and calculated mole fractions of nitrogen versus time at four elevations, ranging from 0.6 to 1.35 m above the top of the tank. The measured results are represented with symbols, while the calculated results are represented with solid lines containing symbols.

The calculation reasonably represented the trends observed in the isothermal experiment. First, the mole fraction of nitrogen initially increased more rapidly at the lowest elevation, due to the shorter distance from

the tank, which was initially full of nitrogen, and more slowly at the higher elevations. Second, because there were no buoyancy differences between the two vertical legs of the U-tube in this experiment, the mole fractions in both legs increased symmetrically. The calculated results were also generally in reasonable quantitative agreement with the measured values. The calculated results were slightly outside the uncertainty of the measurements at the elevation of 0.6 m, but within the uncertainty at the higher elevations. Similar results were obtained by Lim and No (2003), which indicates that possible errors in the RELAP5 code or input model are not the likely causes of the differences.

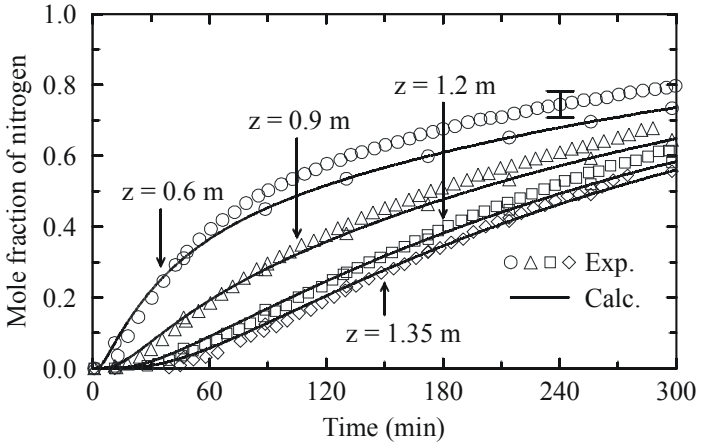

Figure 4-3 Measured and calculated results for the isothermal test.

A sensitivity calculation was performed in which the number of control volumes was doubled from that shown in Figure 4-2. As shown in Figure 4-4, the calculated results were slightly better with the more detailed nodalization. The calculated results are not expected to be as accurate using a coarser nodalization that is typical of most reactor system models, where the core is generally modeled with about 10 control volumes. However, the more coarsely nodalized system models are expected to show correct trends.

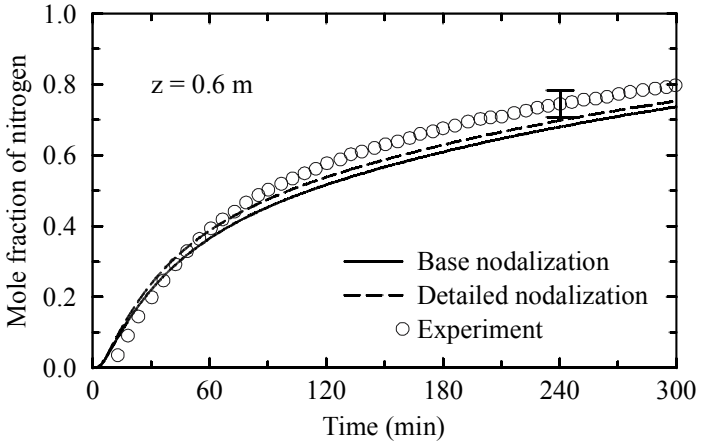

Figure 4-4 The effect of nodalization on calculated results for the isothermal experiment.

Calculated and measured results for the non-isothermal experiment are shown in Figures 4-5, 4-6, and 4-7, which correspond to elevations 0.6, 0.9, and 1.35 m above the top of the tank, respectively. Each figure shows results for both the hot and cold legs of the inverted U-tube. In both the calculation and the test, the mole fraction of nitrogen increased more rapidly on the hot side of the U-tube than on the cold side due to a larger diffusion coefficient, which increases with temperature, and buoyancy effects, which aided the

movement of nitrogen on the hot side of the U-tube and opposed it on the cold side. The rapid increase in mole fraction near 220 min was caused by the onset of natural circulation.

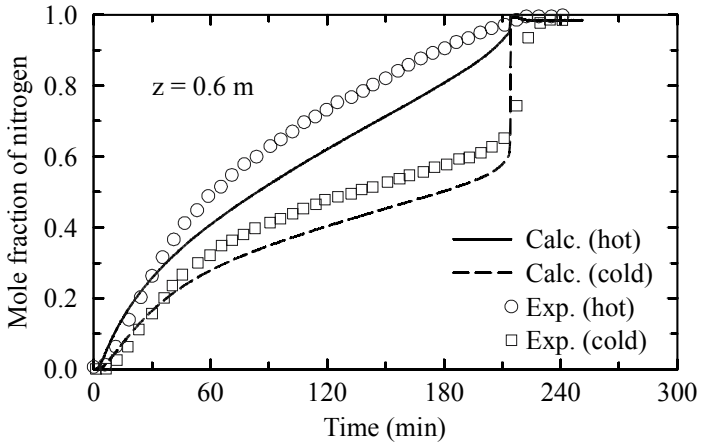

Figure 4-5 Measured and calculated results for the non-isothermal experiment at 0.6 m.

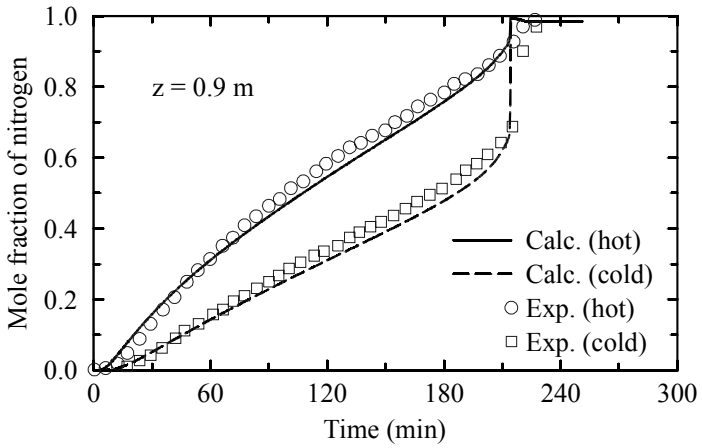

Figure 4-6 Measured and calculated results for the non-isothermal experiment at 0.9 m.

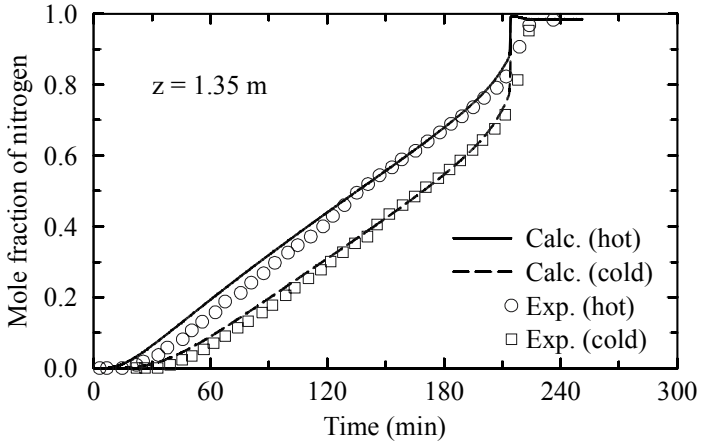

Figure 4-7 Measured and calculated results for the non-isothermal experiment at 1.35 m.

The calculated results were in reasonable quantitative agreement with the measured values. The differences between the calculated and measured results were generally within the reported uncertainty at all

measurement locations except for the lowest one. The calculated results at the lowest locations are similar to those obtained by Lim and No (2003). The timing of the onset of natural circulation, which introduces relatively large amounts of air into the core and therefore could initiate significant graphite oxidation in a reactor, was calculated to within a few minutes.

Assessment of Natural Circulation through a Pebble Bed

The RELAP5-3D computer code was assessed using natural circulation data generated in the NACOK experimental apparatus (Kuhlmann 2002). The NACOK experiments were designed to investigate the effects of air ingress into the core of a high-temperature reactor following a loss-of-coolant accident. The experiments investigated the effects of molecular diffusion, natural circulation, and oxidation. The natural circulation experiments were used for this assessment.

The NACOK experiments simulated natural circulation of air through a scaled model of a high-temperature reactor containing a pebble bed core as shown in Figure 4-8. The experimental apparatus consisted of an experimental channel, a coaxial duct, supply and return tubes, and heating elements. The experimental channel had a square 300x300 mm cross-section and a total height of 7.3 m. The experimental channel consisted of three axial sections including a bottom reflector, a 5.0-m long section containing packed spheres, and an empty 1.7-m long section hereafter called the top reflector. The 60-mm diameter spheres were packed in a regular arrangement of 25 spheres per layer. Every other layer used half spheres along two of the four channel walls. The resulting porosity of the packing was 0.395. The inner diameter of the supply and return tubes was 125 mm. The coaxial duct was a horizontal annulus with both the inner and outer tubes connected to the atmosphere.

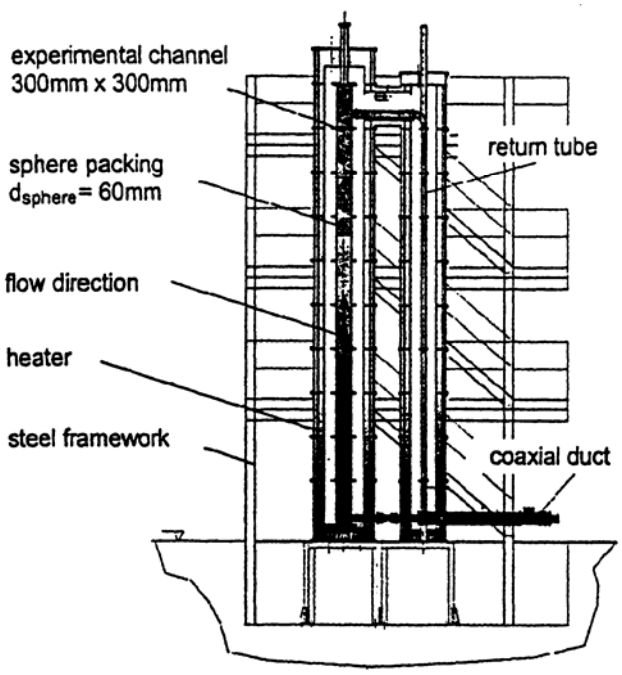

Figure 4-8 Schematic of the NACOK experimental apparatus (from Schaaf et al. 1998).

Heating elements were used to control the temperature of the walls in the experimental channel and the return tube during the experiments. The wall temperature of the return tube was set at 200, 400, 600 or 800°C. The temperature of the experimental channel was controlled between a minimum value that was 50°C higher than the temperature of the return tube and a maximum value of 1000°C. The difference in temperature between

the experimental channel and the return tube induced air to naturally circulate through the supply tube, up through the experimental channel, down through the return tube to the outer tube in the coaxial duct, and back to the atmosphere. The packed spheres in the pebble bed represented the dominant hydraulic resistance in the flow circuit. Thus, the experiments were used to test the calculation of friction factors in a pebble bed.

The RELAP5 model of the NACOK facility is shown in Figure 4-9. The model represented all the hydraulic components of the experimental apparatus, including the coaxial duct, supply tube, bottom reflector, packed spheres, top reflector, and return tube. Boundary conditions of atmospheric pressure and 20°C were applied in Components 100 and 170, which were time-dependent volumes. The thickness of the supply and return tubes was taken as 4 mm based on Schaaf et al. (1997). The inner diameter of the outer tube in the coaxial duct was then calculated from the area of 0.0080 m^2 reported by Kuhlmann (2002).

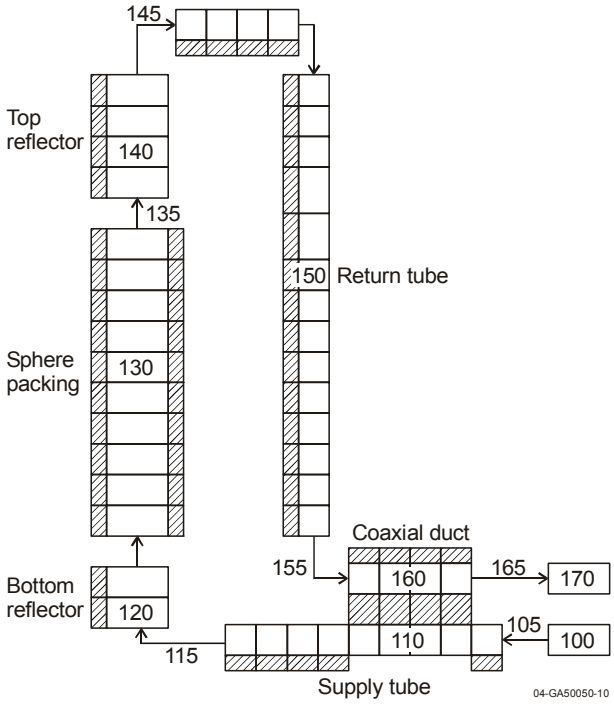

Figure 4-9 RELAP5 model of the NACOK natural circulation experiment.

Heat structures were used to represent the walls of the coaxial duct, the supply and return tubes, and the experimental channel. The packed spheres were also modeled with a heat structure. The wall temperature of the bottom reflector, spheres, top reflector, and the horizontal portion of the return tube were set at the measured value of the experimental channel. The wall temperature of the vertical portion of the return tube was set at the measured value of the return tube. The code calculated the temperature drop due to conduction across each heat structure and the heat flux to the fluid in the adjacent control volume. Because of the small mass flow rates involved, the heat transfer coefficients were generally calculated using natural convection or laminar correlations.

The inner wall of the coaxial duct was modeled to preheat the air entering the experimental channel. The surface temperature of the first heat structure in the supply tube downstream of the coaxial duct was set at the measured temperature of the return tube to represent the portion of the tube within the heating vessel of the return tube. Similarly, the surface temperature of the last heat structure in the supply tube was set at the temperature of the experimental channel. The remaining heat structures in the supply tube were set at the ambient temperature. As shown later, the calculated air flow rates were relatively sensitive to the preheating of the air entering the experimental channel.

The pressure loss across the packed spheres was calculated using the model from SCDAP/RELAP5 (SCDAP/RELAP5-3D Code Development Team 2003). For single-phase flow, the model reduces to the Ergun equation given by Bird et al. (1960). The Ergun equation is

$$\Delta P = \rho V_o^{\,2}\left(\frac{150(1-\varepsilon)^2}{Re_o\,\varepsilon^3}+\frac{1.75(1-\varepsilon)}{\varepsilon^3}\right)\frac{L}{D_p}\ , \qquad (1)$$

where

ΔP = pressure drop due to friction
ρ = fluid density
$V_o = \varepsilon V$ = superficial velocity, where V is the actual fluid velocity
ε = porosity or void fraction
$Re_o = \frac{\rho V_o D_p}{\mu}$ = Reynolds number based on superficial velocity
μ = fluid dynamic viscosity
L = length of the pebble bed
D_p = diameter of a pebble.

The RELAP5 model shown in Figure 4-9 was used to perform a series of calculations in which the wall temperatures were held constant at the measured values until a steady state was achieved. The results of the calculations are illustrated in Figure 4-10, which shows mass flow rate of air as a function of the temperature in the experimental channel for temperatures of the return tube, T_R that varied between 200 and 800°C. The calculated results were in reasonable agreement with the measured values. The important trends observed in the experiments were predicted by the code. In particular, the shape of the curve at T_R = 200°C was similar in the calculations and the experiment. The mass flow rate initially increased sharply with increasing experimental channel temperature, reached a maximum value near 550°C, and then gradually decreased. The volumetric flow increased monotonically with experimental channel temperature because the increased temperature difference between the channel and the supply tube caused an increased driving head for natural circulation. However, the mass flow decreased at higher temperatures because the density decreased at a faster rate than the volumetric flow increased, and, to a lesser extent, because the Reynolds number was decreasing, which caused increased hydraulic resistance as indicated by Equation 1. The code also correctly predicted the trend of decreasing mass flow as T_R increased at a given experimental channel temperature. This trend was primarily caused by the decreased temperature difference between the experimental channel and the return tube, which decreased the driving head for natural circulation. The RELAP5 model was used to simulate all 40 data points reported by Kuhlmann (2002). The root-mean-square error in the calculated flow rate was 0.21 g/s, which corresponds to about 5% of the maximum measured value. The value of $Re_o/(1-\varepsilon)$ varied between 9 and 120 in the calculated results shown in Figure 4-10.

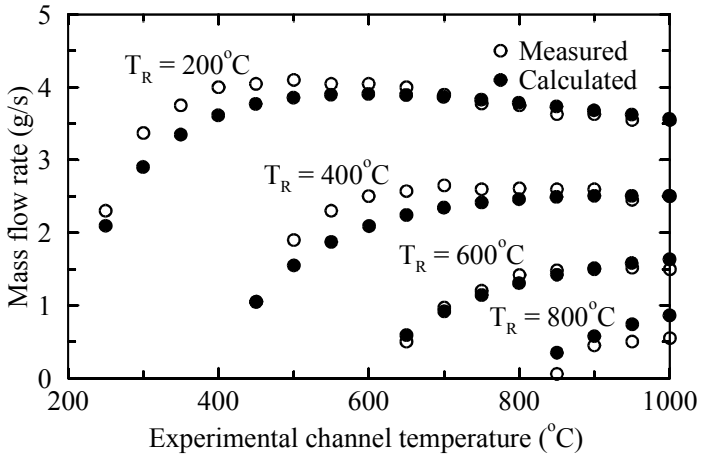

Figure 4-10 Measured and calculated air flow rates for the NACOK natural circulation experiments.

The average calculated fluid temperature in the experimental channel was less than the reported temperature because a certain distance was required to heat the fluid in the experimental channel up to the temperature of the wall. Similarly, the average calculated fluid temperature in the return tube was less than the imposed wall temperature of the return tube. As a result, the actual driving head for natural circulation was less than that obtained from the difference in fluid densities corresponding to the difference in wall temperatures between the experimental channel and the return tube. The calculated driving head for natural circulation varied between 60 and 90% of the value calculated from the difference in wall temperatures.

The calculated mass flow rates were sensitive to the temperature boundary conditions applied to the walls of the heat structures, which affected the relative fluid temperatures and densities in the experimental channel and the return tube and thus affected the driving head for natural circulation. For example, a sensitivity calculation was performed in which the boundary condition in the horizontal leg at the top of the return tube was changed from the temperature of the experimental channel to the temperature of the return tube. Although Kuhlmann (2002) did not report the average wall temperature in this portion of the return tube, the actual temperature is expected to be between the reported values for the experimental channel and the return tube, and probably nearer to that of the experimental channel as assumed in the original calculation. Applying a lower wall temperature in this relatively short region resulted in a lower average fluid temperature in the return tube, which increased the driving head for natural circulation and resulted in an increase in the calculated mass flow rate of 0.26 g/s averaged over all 40 data points. A second sensitivity calculation was performed in which the wall temperatures of the last heat structure in the supply pipe and of the two heat structures in the bottom reflector were changed from the reported temperature of the experimental channel to a value halfway between the ambient and experimental channel temperatures. Applying a lower wall temperature in this portion of the experimental channel decreased the average fluid temperature in the channel, which decreased the driving head for natural circulation and resulted in an average decrease in the calculated mass flow rate of 0.23 g/s. The average change in the flow rate for each sensitivity calculation is significant compared to the root-mean-square error of 0.21 g/s reported earlier.

Assessment of Molecular Diffusion with MELCOR

In the last quarterly report, results from MELCOR were shown for the diffusion of a ternary gas mixture corresponding to the experiment described by Duncan and Toor (A.I.Ch.E Journal 1962). As indicated in the report the general shape of the mole fraction curves agreed with the experimental data, however the timing of the diffusion process did not agree. This last quarter we ran the same model on the latest released version of

MELCOR (version 1.8.5) with the entire gas reactor updates provided by INEEL included in the new version of MELCOR. The results from this new calculation agree very well with the experimental results.

A schematic of Duncan and Toor experiment is shown in Figure 4-11. The experiment consisted of two volumes connected by a short capillary diffusion line. The two volumes are referred to in the figure as Bulb #1 and Bulb #2. Bulbs #1 and #2 have volumes of 77.99 cm^3 and 78.63 cm^3, respectively. The diffusion line connecting the two bulbs is 85.9 mm long with an internal diameter of 2.08 mm. The diffusion line contains a stopcock, which is used to separate the gas mixture contained in bulb #1 from the gas mixture contained in bulb #2. The gas contained in bulb #1 is a mixture of nitrogen and carbon dioxide with a molar composition of 50.086 percent nitrogen and 49.914 percent carbon dioxide. The gas mixture in bulb #2 contains nitrogen and hydrogen with a molar composition of 49.879 percent nitrogen and 50.121 percent hydrogen. When thermal (32.5°C) and mechanical (1 atm) equilibrium was established between the two bulbs, the stopcock was opened allowing the diffusion process to begin.

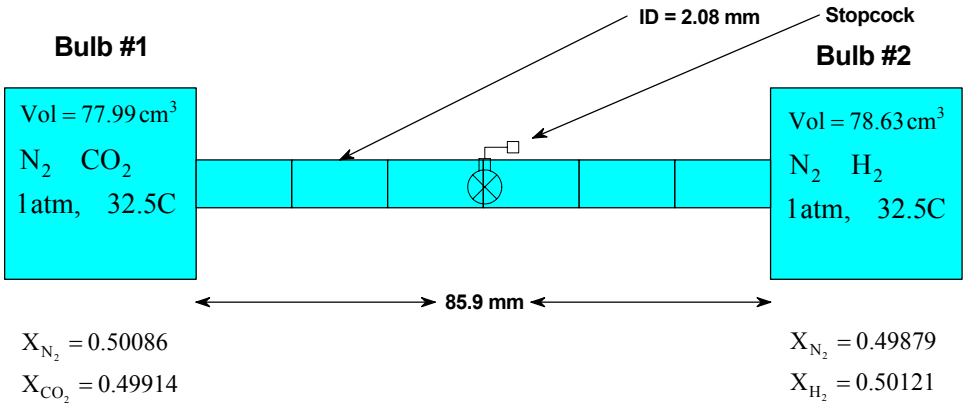

Figure 4-11 Schematic of the two-bulb experiment.

The results from the experiment show that the nitrogen in bulb #2, which has a slightly higher concentration of N2, begins to diffuse toward bulb#1. In a short time (≈ 130 sec) the mole fraction of N2 in bulb #2 drop below the mole fraction of N2 in bulb #1, however the mole fraction of N2 in bulb #2 continues to decrease while the mole fraction of N2 in bulb #1 increases. This trend continues until approximately 6 hr at which time the mole fraction in bulb #1 stops increasing and starts to decrease. At this time the mole fraction in bulb #2 stops decreasing and starts to increase. The period between 130 sec and 6 hr is referred to as the reverse diffusion of nitrogen.

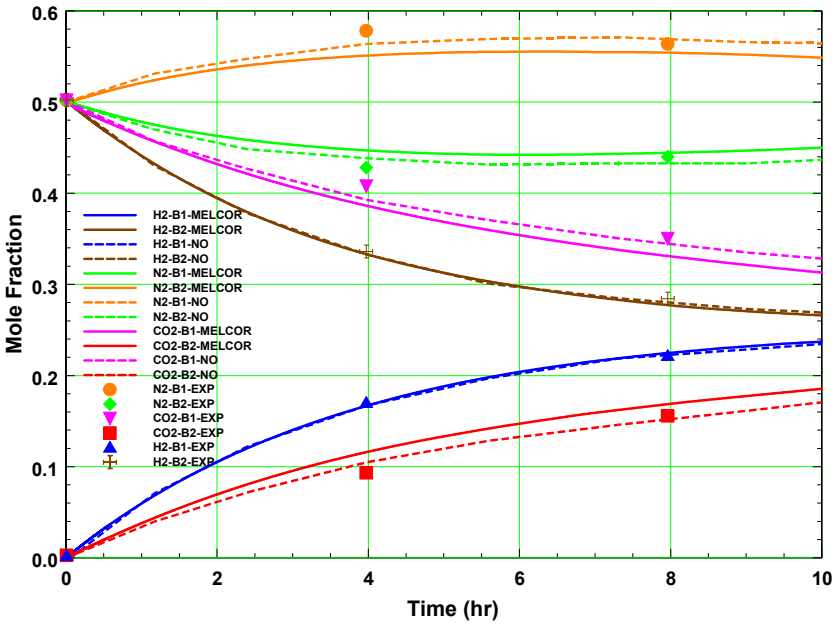

Figure 4-12 Multi-component diffusion results.

Viewing the results in Figure 4-12, we see that the MELCOR results compare very well with the experimental results for the diffusion of a ternary gas mixture.

***Next year activities*:** In the next year, we will perform additional assessment uing the RELAP5/ATHENA and MELCOR computer codes.

Issues / Concerns: There are neither issues or concerns.

Task 5: Neutronic Modeling (University of Michigan)

Task Status and Significant Results

Effort to date has been focused on analyzing the double heterogeneity posed by the TRISO fuel and to predict the VHTR power distribution with thermal/hydraulic feedback. These efforts are described below.

1. Analysis of Double Heterogeneity

Effort to date has been focused on developing MCNP5 (Brown, 2003) models with both homogeneous and heterogeneous microsphere fuel particle (TRISO), including (a) single microsphere models, (b) fuel compact models, and (c) full-core models. Results have been obtained for all levels of analysis, including preliminary results for the full-core model with reflectors. These efforts are described below.

(a) Single microsphere model

A heterogeneous microsphere fuel particle model has been created with MCNP consistent with the NGNP Point Design (MacDonald, 2003). This single microsphere cell consists of a 10.36% enriched fuel microsphere and graphite matrix to yield a packing fraction = 0.289 and explicitly models all regions: fuel kernel, carbon buffer, SiC, and inner/outer pyrolytic carbon shells and graphite matrix. Figure 5-1 depicts the geometry.

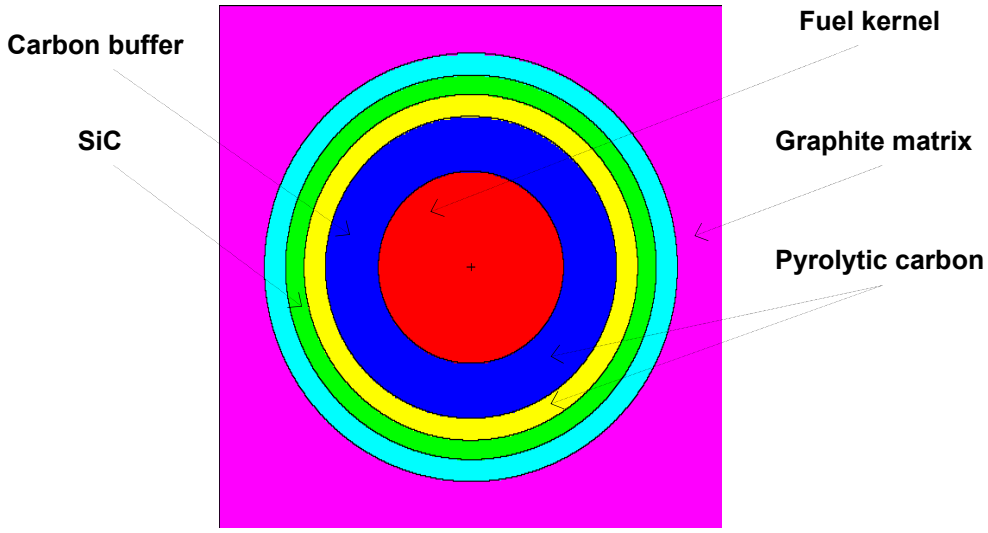

Figure 5-1 Heterogeneous Microsphere Cell for TRISO Fuel.

We performed neutronic analyses for a single microsphere fuel cell for three different models: homogeneous model (homogenized mixture of microsphere and graphite matrix), two-region model (fuel kernel and remainder of microsphere/graphite matrix), and fully heterogeneous model, as shown in Figure 5-1. Figure 5-2 shows the MCNP5 geometries for these three models.

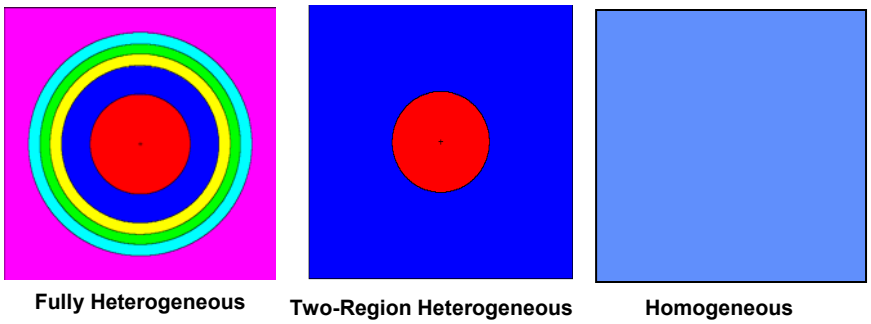

Figure 5-2 Single Microsphere Cells.

For each different model, we performed criticality calculations and the results are given in Table 5-1 (Ji, 2004). It is clear that the microsphere heterogeneity must be included in the neutronic analysis as it represents a 5% reactivity effect, and this does not account for the reactivity effect caused by the fuel compact heterogeneity.

The LANL calculation (Brown, 2004a; Brown, 2004b) was performed by Dr. Forrest Brown of the MCNP Group in X-5 division. The "fully heterogeneous" term means that the location of the sphere was "jiggled" randomly every time the neutron entered (or re-entered) the cell, with the constraint that the sphere could not overlap the boundary of the cube. Therefore, at the microsphere level, the random location of the sphere within the cubical cell represents a .2% decrease in k_{eff} compared with the sphere centered in the cell.

The two-region cell gave nearly the same results as the fully heterogeneous cell and since the latter case takes twice the computational time, this may warrant the use of the two-region cell for neutronic analyses of VHTR fuel. This is discussed further in the next paragraph.

To analyze the two-region model, we calculated the multi-group radial flux profiles for both two-region and fully heterogeneous microsphere cells. Figure 5-3 shows the tally region divisions for two models and Figure 5-4 depicts the flux profiles for the fully heterogeneous model (note the log scale). Figure 5-5 compares the radial profiles for the two-region cell versus the heterogeneous cell for representative resonance energy neutrons in the energy range 6.57-6.77 eV.

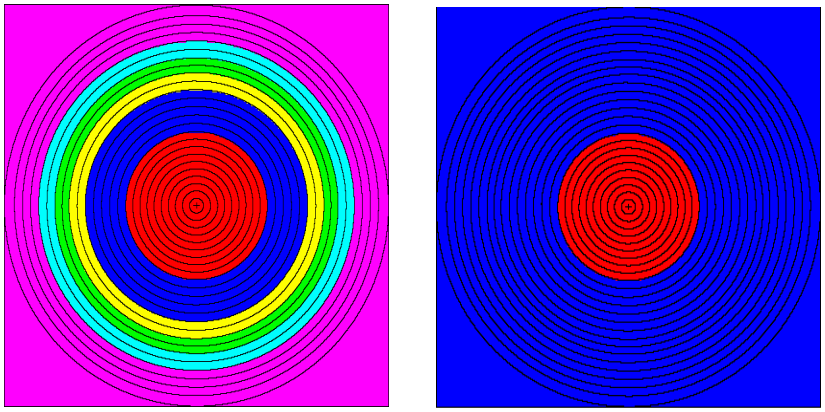

Fully Heterogeneous. **Two-Region Heterogeneous.**

Reflecting b.c. on all sides of cubes.

Figure 5-3 Tally regions for Two-Region Microsphere Models.

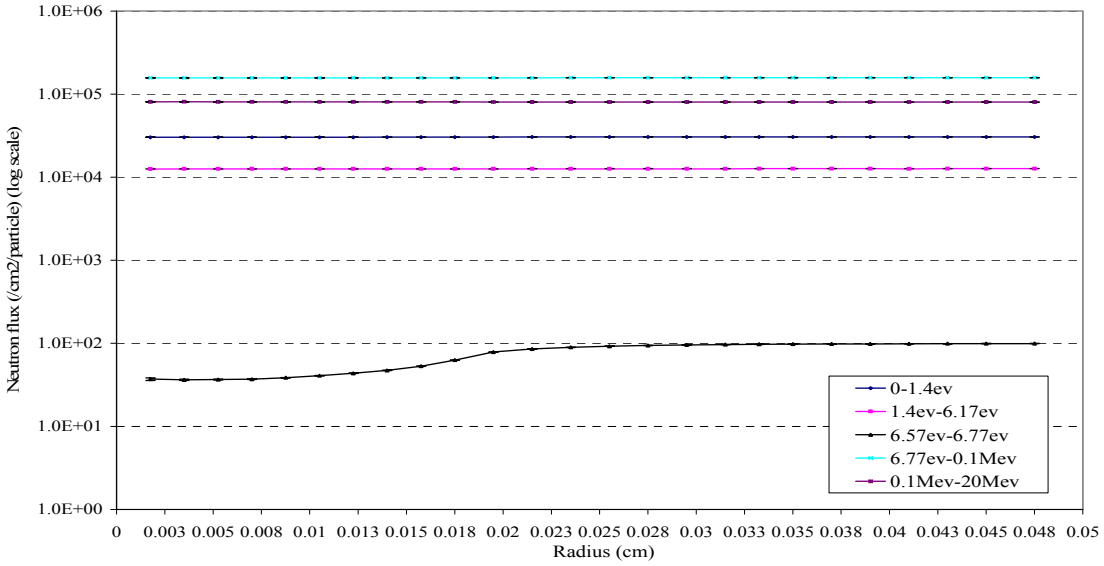

Figure 5-4 Energy-Dependent Radial Flux Profiles for Heterogeneous Microsphere Cell.

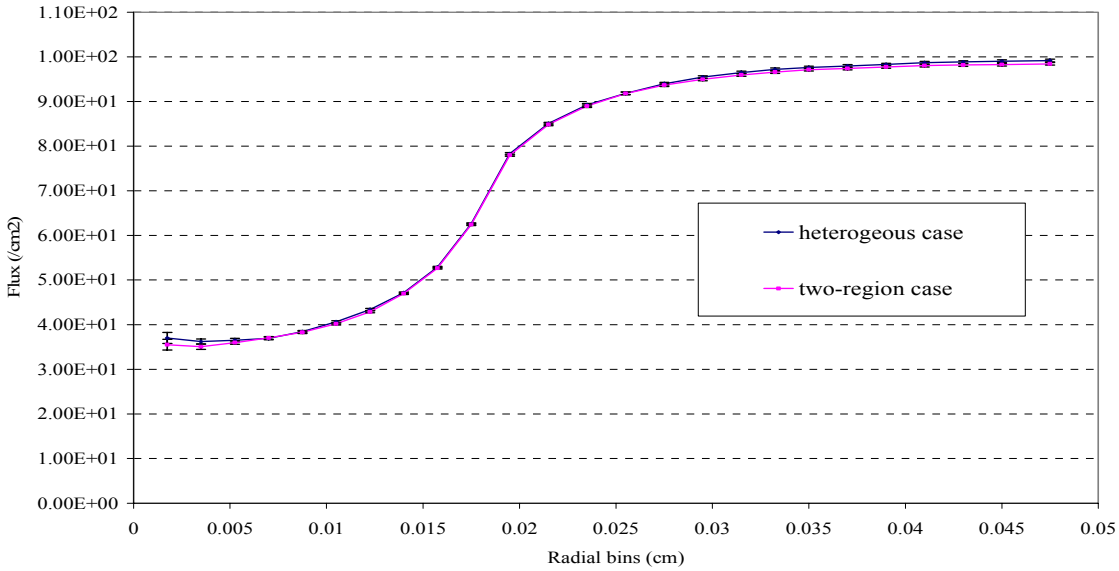

Figure 5-5 Comparison of 6.57-6.77 eV Flux Profiles.

Energy spectra in the fully heterogeneous microsphere cell model were calculated. The calculations were done separately for six regions in one cell from inner most to the outer most: fuel kernel, carbon buffer, inner pyrolytic carbon, SiC, and outer pyrolytic carbon shells and graphite matrix. Figure 5-6 shows the results and it can be seen that except for the neutron energies close to the resonance peaks, which Figure 5-6 does not resolve, the spectra are essentially the same in all regions of the microsphere cell. Together, Figures 5-4 and 5-6 indicate that the TRISO fuel is homogeneous for all neutrons except resonance energy neutrons.

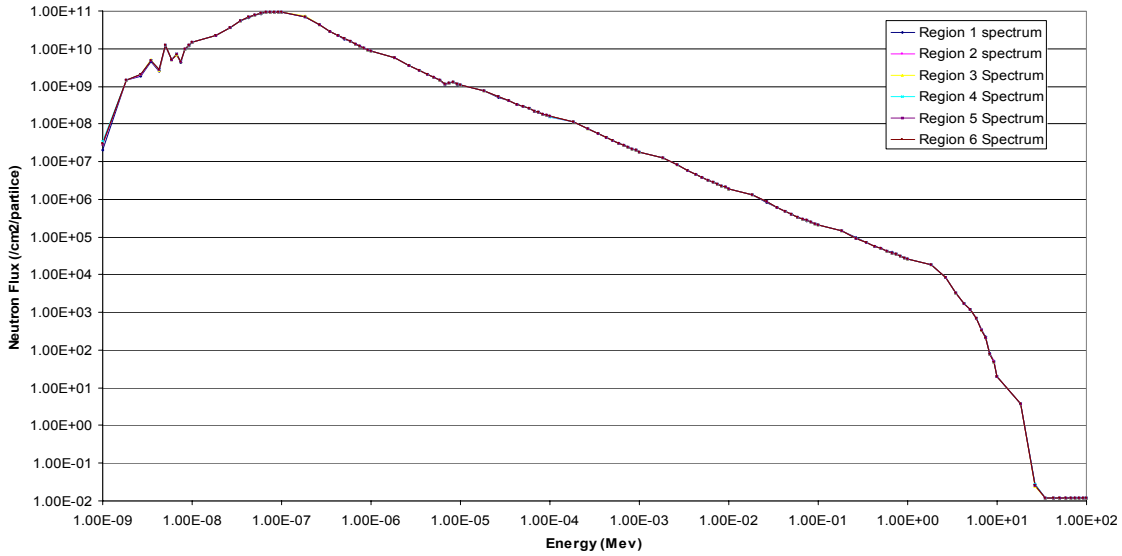

Figure 5-6. Energy Spectra for Heterogeneous Microsphere Model.

(b) Fuel compact model

The fuel compact geometry was modeled in three different ways: homogeneous, two-region heterogeneous and fully heterogeneous. Fig. 5-7 shows the three different MCNP5 fuel compact models. The graphite region surrounding the fuel compact is the proportional share of the graphite in a hexagonal block that "belongs" to a fuel compact. Table 5-2 is the summary of the MCNP5 criticality calculations for these fuel compact cells. Note that heterogeneous microsphere geometry is important at the fuel compact level as well, giving a 4% change in reactivity versus homogeneous fuel.

We have also modeled hexagonal fuel block geometry, where coolant holes and fuel compact cells are modeled explicitly. These calculations have been done with homogeneous and heterogeneous fuel compacts but the results are not included in this report, since they are consistent with the fuel compact results and we also have full-core results to present.

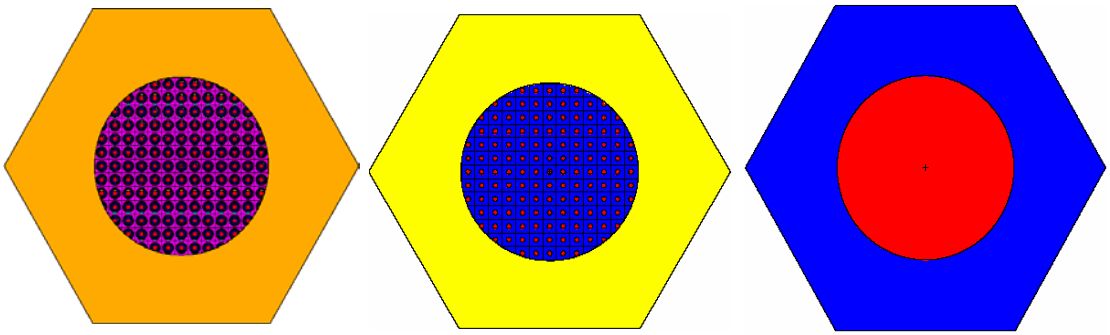

Reflecting b.c. on all surfaces of fuel compact cell

Figure 5-7 Fuel Compact Cells.

Table 5-2 MCNP5 Simulations of Fuel Compact Cells.

Fuel Compact	k_{eff}	Sigma
Homogeneous microsphere cells	1.2885	.0004
Two-region heterogeneous microsphere cells	1.3408	.0004
Fully heterogeneous microsphere cells	1.3401	.0004

(c) Full core model

Based on the microsphere cell and fuel compact cell models, we have modeled the full core geometry with MCNP5. Figure 5-8 shows the progression from microsphere cell to fuel compact cell to fuel block cell to full core geometry.

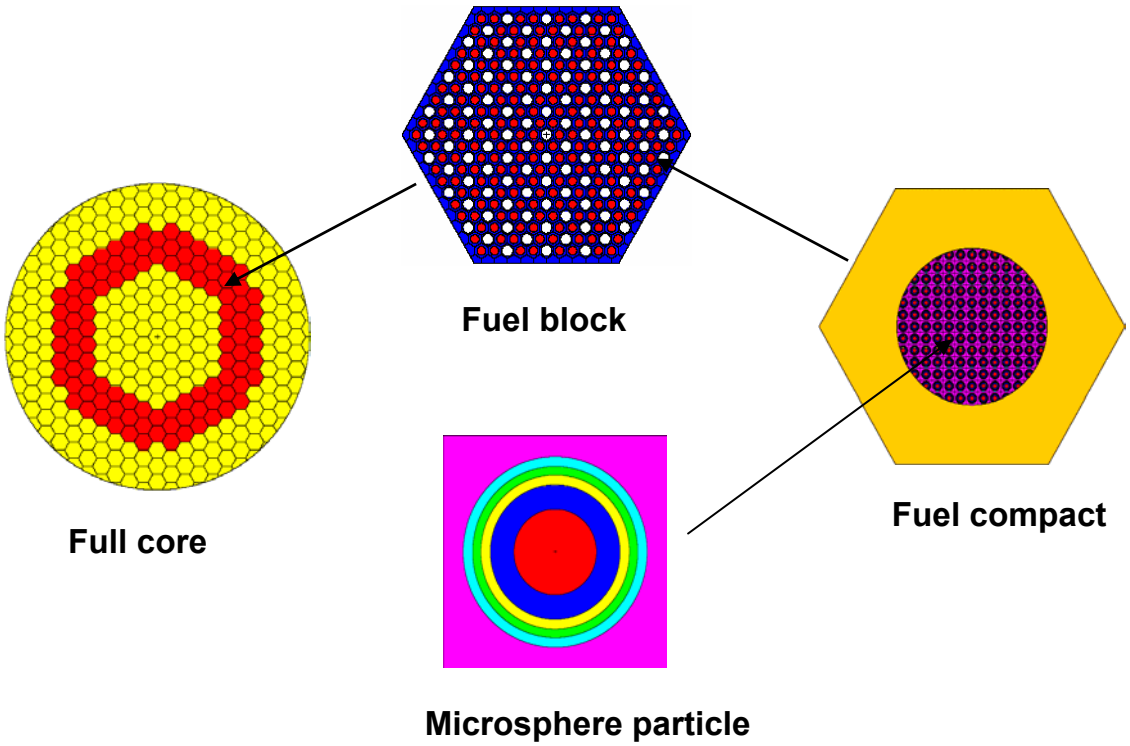

Figure 5-8 Modeling the Double Heterogeneity from Microsphere Cell to Full Core.

Criticality calculations have been performed with MCNP5 for four different full core (all fuel blocks and all axial and radial reflectors) models: (1) homogeneous model (homogenized fuel blocks), (2) heterogeneous fuel blocks with homogenized fuel, (3) double heterogeneous model (heterogeneous fuel blocks with heterogeneous fuel) with two-region microsphere cells and (4) double heterogeneous model with fully heterogeneous microsphere cells. The double heterogeneous cases model the microsphere at the center of the microsphere cell. Table 5-3 shows the results. These are preliminary calculations and need to be compared

with other results, but the relative changes are interesting. The first heterogeneity posed by the fuel compact represents a 4% change in reactivity while the second heterogeneity caused by the microspheres represents another 4% change. It is clear that the neutronic analysis of VHTR configurations has to account for both effects. Also, the full-core results with two-region microsphere cells versus heterogeneous microsphere cells indicate that the two-region model may be an acceptable alternative since the k_{eff} agreed to within .01% for the two cases, although the uncertainty is larger than this result.

Table 5-3. MCNP5 Simulations of Full Core Models.

Full Core	k_{eff}	Sigma
Homogeneous fuel block cells	1.0153	.0002
Fuel block level heterogeneous cells	1.0583	.0001
Double heterogeneity with two-region heterogeneous microsphere cells	1.0949	.0004
Double heterogeneity with fully heterogeneous microsphere cells	1.0949	.0003

2. VHTR Power Distribution with T/H Feedback

This effort involved two distinct activities: (a) the creation of temperature-dependent cross sections for the VHTR full core model and (b) performing the explicit T/H feedback calculations to arrive at a converged power distribution for the VHTR. These efforts are described below.

(a) Generation of temperature-dependent cross-section libraries

The cross-section libraries included in the standard MCNP5 distribution are limited to 12 or fewer discrete temperatures for ^{235}U and ^{238}U, and even fewer for other isotopes. In order to represent distributed temperatures, we have devised a pseudo-material scheme in our MCN5 runs, where cross section libraries at a few temperature points are mixed and interpolated to yield cross section libraries at the desired temperature. The number density associated with each library is a fraction of the total number density of the isotope dependent on the temperature of both cross-section libraries and the desired temperature of the pseudo-material. The advantage of using pseudo-materials is that cross sections for any arbitrary temperature can be determined at run time by "mixing" cross sections from materials at the bracketing temperatures, avoiding the need to determine cross section sets for every conceivable temperature beforehand.

For a given isotope in a material, there will be two cross-section libraries used. The temperatures at which these libraries were generated bound the desired temperature of the material. The formula for calculating the number density associated with the lower temperature cross section is shown below:

$$P_L = \frac{\sqrt{T_H} - \sqrt{T}}{\sqrt{T_H} - \sqrt{T_L}},$$

where T_H is the temperature of the higher temperature cross-section library, T_L for the lower temperature library and T is the temperature of interest. This functional form is suggested by the known dependence of the resonance integrals on $\sqrt{T}$ (Askew, 1971) and the realization the Doppler broadening of the resonance integrals is the primary reactivity effect of a higher temperature. The percentage of the total number density

associated with the higher temperature is then $P_H = 1 - P_L$. The fractions, P_H and P_L, are then used to calculate the number density used on the material card for that particular isotope and library.

We performed a test to determine the validity of this approximation. We ran full core simulations with homogeneous fuel assembly blocks for each temperature library using the normal method of choosing a temperature for MCNP. We compared the value of k_{eff} for these normal materials with our pseudo materials and found good agreement across the temperature spectrum of interest. Everything in the simulation was kept the same between the normal and pseudo-materials except for the definition of the materials cards. The results can be seen in Figure 5-9, where the error bars represent one standard deviation.

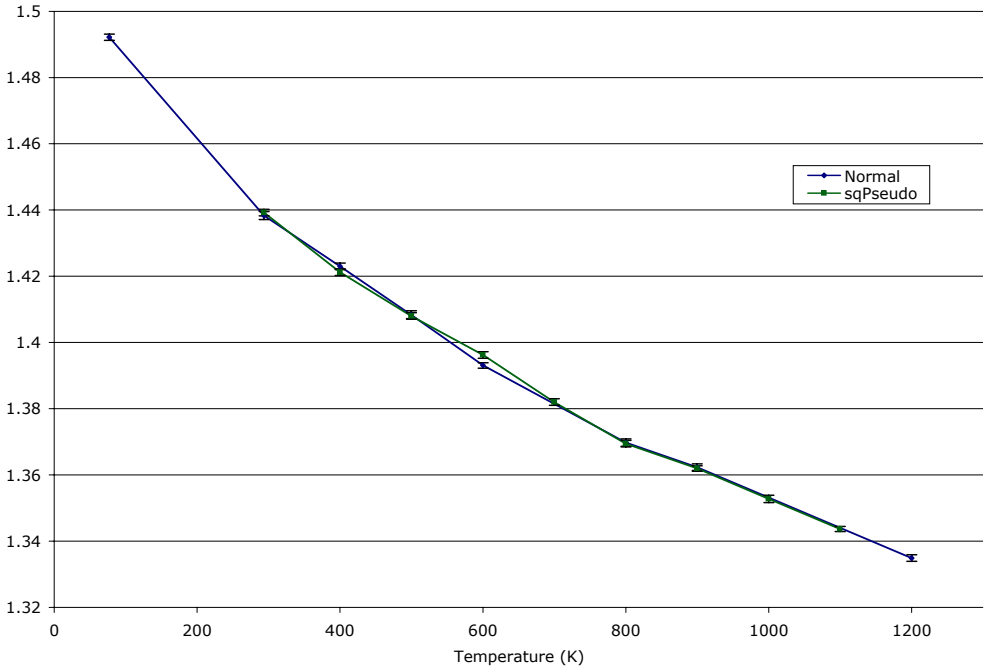

Figure 5-9 Comparison of Pseudo-Materials with √T Interpolation.

The drawback to using pseudo-materials is you must have libraries at temperatures above and below the desired temperature. The largest temperature that ships with MCNP is 3000 K followed by 1200K; we didn't use the library at 3000 K. In order to reduce this limitation we are generating Doppler broadened versions of the libraries at one hundred degree Kelvin intervals. Combining this with the use of the pseudo-material concept, we expect to have more flexibility on the range and accuracy of the temperature of our materials.

A Python script is being created that accepts as input, a list of temperatures from RELAP5/ATHENA and creates an MCNP input deck with radial and axial temperature zones using the Doppler-broadened libraries and pseudo-materials. This is described below.

(b) Prediction of global VHTR power distribution with T/H feedback

We have made initial efforts to represent the effects of temperature feedback on global power distributions. For this coupled nuclear-T/H analysis for the VHTR core configuration, we have used a homogenized

representation for each of 103 prismatic fuel assemblies and grouped the fuel assemblies into three rings: inner, middle and outer rings comprising 30, 37, and 36 assemblies each. The core, with a height of 7.93 m, is discretized axially into 12 equal segments.

With the assistance of Dr. George Mesina and Mr. Cliff Davis at INEEL, we have performed RELAP5/ATHENA (RELAP5 Team, 2003) calculations representing the homogenized three-ring model of the VHTR core. With minor modifications to the RELAP5 input deck that Mr. Davis provided to UM, we have gone through to date four iterations involving manual transfers of temperature and power distributions between MCNP5 and RELAP5/ATHENA. The RELAP5/ATHENA code determines the temperature distribution for the 36 regions of the global geometry based on the power distribution from MCNP5. Pseudo-material number densities corresponding to the region-average temperatures are then determined for MCNP5. As illustrated in Figure 5-10 after four iterations, we have yet to achieve a satisfactory convergence on the axial power distributions within each of the three rings, although the fraction of the power summed over each ring is easily converged. This may be due to the large core height, which tends to make the core loosely coupled, thereby rendering the axial power distribution sensitive to axial imbalances in cross sections. This is currently under investigation.

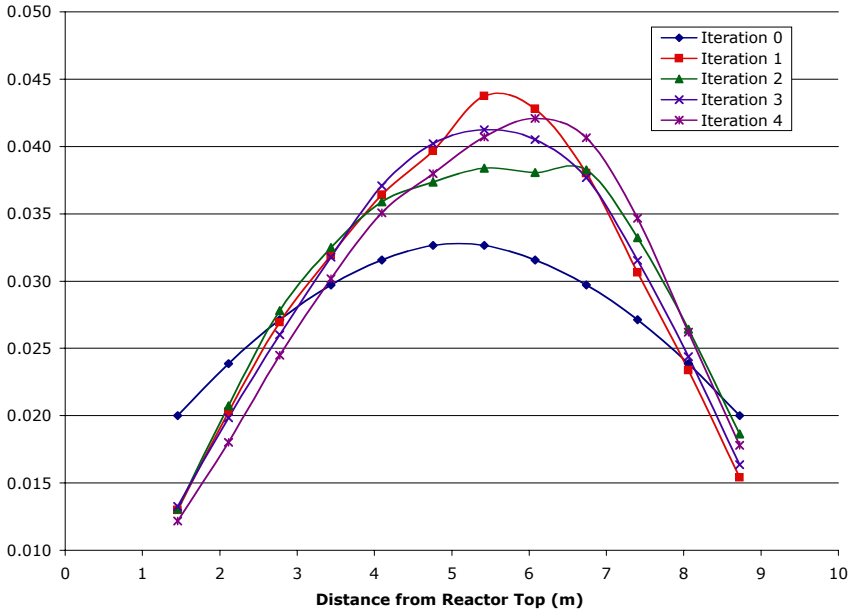

Figure 5-10 Iterations on Axial Power Distribution in the Middle Core Ring.

Next year activities

The full-core calculations will be compared to other predictions for both homogeneous and heterogeneous fuels. The effect of random orientation of the microspheres within the microsphere cell will be assessed by performing full-core calculations with random microspheres versus a uniform array of microspheres. The temperature-dependent flux and power distributions will be determined. The analysis of depletion will be initiated. Not only is the choice of depletion module a question but also the effect of depletion on the modeling of double heterogeneities needs to be examined.

Issues/Concerns: None.

Task 6 -- Verification and validation (INEEL and KAIST).

Each party has completed initial assessments during the past year. Additional assessments will be performed in year 2005. Assessments of the data being generated at SNU will also be performed.

APPENDIX-A

References

Task 1

J.J. Duderstadt and W.R. Martin, Transport Theory, John Wiley & Sons, 1979.

J. P. HOLAMAN, Heat Transfer, McGraw-Hill, New York, 1986.

T. Schaaf, et. al., "The NACOK Experimental Facility for Investigating an Air Ingress into the Core of a High Temperature Reactor," Kerntechnik, Vol. 63, No. 3, 1998.

"Heat Transport and Afterheat Removal for Gas Cooled Reactors Under Accident Conditions," IAEA-TECDOC-1163, International Atomic Energy Agency, 2000.

T. TAKEDA, "Air Ingress Behavior during a Primary-pipe Rupture Accident of HTGR," JAERI-1338, Japan Atomic Energy Research Institute, 1997.

Task 2

IAEA, "Heat Transport and Afterheat Removal for Gas Cooled Reactors Under Accident Conditions," IAEA-TECDOC-1163, Vienna, 2000.

N. Kuzavkov, "Heat transport and afterheat removal for gas cooled reactors under accident conditions," IAEA, Vienna, pp.19-27, 2000.

D.Especel, S.Mattei, "Total emissivity measurement without use of an absolute reference," *Infrared Physics & Technology* **37**, pp.777-784, 1996.

N. Lallemant, A. Sayre, R. Weber, "Evaluation of emissivity correlation for H20-CO2-N2/Air mixture and coupling with solution methods of the radiative transfer equation," *Prog. Energy Combust. Sci*., Vol. 22, pp. 543-574, 1996

S. S. Sazhin, E. M. Sazhina , "The effective-emissivity approximation for the thermal radiation transfer problem," *Fuel*, Vol.75, No. 14, pp. 1646-1654, 1996.

Leonid A. Dombrovsky, "Heat transfer by radiation from a hot particle to ambient water through the vapor layer," *International Journal of Heat Mass Transfer***, 43**, pp. 2405-2414, 2000.

J Nikuradse, "Gesetzmessigkeiten der turbulenten stromung in glatten rohren," In Forschungsheft 356, volume B. VDI Verlag Berlin (1932). Translated in NASA TT F-10, 359, 1966.

W.B. Hooper, "The Two-K method predicts head losses in Pipe Fittings," *Chem. Eng*., **24**, pp 96-100, 1981.

S. Kakac, R.K. Shah and W. Aung, Handbook of single-phase convective heat transfer, A Wiley-Interscience publicaion, 1987.

F.W. Dittus and L.M.K. Boelter, University of California, Berkeley, Publications on Engineering, Vol.2, p 443, 1930.

Y. Mori and W. Nakayama, "Study on Forced convective Heat Transfer in Curved Pipes", *Int. J. Mass Transfer*, **10**, pp. 37-59, 1967.

M. P. Paulsen, et al., "RETRAN-3D – A Program for Transient Thermal-Hydraulic Analysis of Complex Fluid Flow Systems," EPRI NP-7450, 1996.

S.R. Tailby and P.W. Staddon, "The influence of 90o and 180o pipe bends on heat transfer from an internally flowing gas stream," *Heat Transfer*, Vol.2 paper No. FC 4.5, 1970.

M. Moshfeghian and K.J. Bell, “Local heat transfer measurements in and downstream from a U-bend,” ASME paper No. 79-HT-82, 1979.

J.Pruvost,J.Legrand and P.Legentilhomme, “Numerical investigation of bend and torus ows,part I :e ect of swirl motion on ow structure in U-bend,” *Chemical Engineering Science*, **59**, pp. 3345 –3357, 2004.

IAEA, "Current status and future development of modular high temperature gas cooled reactor technology," IAEA-TECDOC-1198, 2001.

A. A. Zukauskas, “Heat Transfer from Tubes in Cross Flow,” *Adv. Heat Transfer*, **8**, pp. 93-106, 1972.

Y. Mori and W. Nakayama, “Study on Forced convective Heat Transfer in Curved Pipes,” *Int. J. Mass Transfer*, **10**, pp. 37-59, 1967.

F. P. Incropera and D. P. DeWitt, “Introduction to Heat Transfer”, 5th Edition, John Wiley and Sons, New York, p. 357, 2002.

TAC Technologies, “NEVADA Software Package Quick Reference Series”, TAC Technologies, USA, 2000.

Task 3

Z. Alkan et al., ”Corrosion-resistant graphite for nuclear application,” KERNTECHNIK **63,** 3, 98-106, 1998.

Minoru Takahashi, Masahiro Kotaka and Hiroshi Sekimoto, “Burn-off and production of CO and CO2 in the oxidation of nuclear reactor grade graphite in a flow system,” J. Nuclear Science and Technology **31**, 12, 1275-1286, 1994

H.K. Hinsen, W. Katscher, R. Moorman, “Kinetics of the graphite/oxygen reaction in the in-pore diffusion controlled regime,” 1983

J.B. Lewis, J. Dix, R. Murdoch, “The order of reaction for the oxidation of nuclear graphite in moist oxygen-nitrogen mixture,” Carbon **3**, 321-322, 1965

J. Aurthur, “The reaction between carbon and oxygen,” Trans. Faraday Soc **47**, 164-178, 1951

M. Rossberg, Z. Elektrochem. **60**, 952, 1956

Task 4

Bird, R. B., W. E. Stewart, and E. N. Lightfoot, “Transport Phenomena,” John Wiley & Sons, Inc., New York, 1960.

Hishida. M. and T. Takeda, “Study of Air Ingress During an Early Stage of a Primary-Pipe Rupture Accident of a High-Temperature Gas-Cooled Reactor,” Nucl. Eng. and Des., **126**, 175-197, (1991).

Kuhlmann, Mario B., “Experimente zu Gastransport und Graphitkorrosion bei Lufteinbruchstorfallen im Hocktemperaturereaktor,” Berichte des Forshungzaentrums, Julich 4003, ISSN 0944-2952, 2002.

Lim, H. S. and H. C. No, “Transient Multicomponent Mixture Analysis Based on ICE Numerical Scheme for Predicting an Air Ingress Phenomena in an HTGR,” Proc. of NURETH-10, Seoul Korea, October 5-9, 2003.

Reid, R. C., J. M. Prausnitz, and B. E. Poling, “The Properties of Gases and Liquids,” Fourth Edition, McGraw-Hill Book Company, New York, 1987.

RELAP5-3D Code Development Team, “RELAP5-3D© Code Manual,” INEEL-EXT-98-00834, Revision 2.2, October 2003.

SCDAP/RELAP5-3D Code Development Team, "SCDAP/RELAP5-3D© Code Manual, Volume 2: Modeling of Reactor Core and Vessel Behavior during Severe Accidents" INEEL-EXT-02-00589, Revision 2.2, October 2003.

Schaaf, J., W. Frohling, and H. Hohn, "Status of the Experiment NACOK for Investigations on the Ingress of Air into the Core of an HTR-Module," Nuclear Energy Agency, "Workshop on High Temperature Engineering Research Facilities and Experiments," Petten, Netherlands, 12-14 November 1997.

Schaaf, Th., W. Frohling, H. Hohn and S. Struth, "The NACOK Experimental Facility for Investigating an Air Ingress into the Core of a High Temperature Reactor," Kerntechnik, 63, 3, 107-112, 1998.

Task 5

J. R. Askew, D. W. G. Harris, and L. J. Hutton, "The Calculation of Resonance Capture in Granular Fuels," DCPM 11/Winfrith1, Dragon Countries Physics Meeting report (1971).

F. B. Brown, "MCNP – A General Monte Carlo N-Particle Transport Code, Version 5", LA-UR-03-1987, Los Alamos National Laboratory (2003).

F. B. Brown and W. R. Martin, "Stochastic Geometry for MCNP5," *Trans. Am. Nucl. Soc.* **91**, 171-173, Washington, DC (November 2004).

F. B. Brown and W. R. Martin, "Stochastic Geometry Capability in MCNP5 for the Analysis of Particle Fuel," *Annals of Nuclear Energy* 31, (November 2004).

W. Ji, J. L. Conlin, W. R. Martin, and J. C. Lee, "Reactor Physics Analysis of the VHTGR Core," *Trans. Am. Nucl. Soc.* 91, 556-558, Washington, DC (November 2004).

P. E. MacDonald, et al., "NGNP Preliminary Point Design – Results of the Initial Neutronics and Thermal-Hydraulic Assessments During FY-03", INEEL/EXT-03-00870 Rev. 1, Idaho National Engineering and Environmental Laboratory (2003).

The RELAP5-3D Code Development Team, "ATHENA Code Manual," INEEL-EXT-98-00834, Rev. 2.2, Idaho National Engineering and Environmental Laboratory (2003).

APPENDIX –B

Project Milestone / Deliverable Summary

Milestone/Deliverable Description	Planned Completion	Actual Completion
1. CFD TH Code Development	30 June 2005	In progress
1-1 CFD TH model	31 December 2004	Completed
1-2 Diffusion model	31 December 2003	Completed
1-3 Chemical reaction model	30 June 2005	In progress
1-4 Particle model	30 June 2005	In progress
2. RCCS Separate Experiment	30 June 2005	In progress
2-1. Development of water-pool RCCS	31 December 2003	Completed
2-2. Scaling of water-pool RCCS	30 June 2005	In progress
2-3 Heat transfer coefficients	30 June 2005	In progress
3. Air Ingress Separate Experiment	30 June 2005	In progress
3-1. Measurement technique development	30 June 2004	Completed
3-2. Diffusion-limited model	30 June 2005	In progress
4-1. Implementation of Diffusion model	31 March 2005	In progress
4-1-A. Noncondensable gas implementation	30 April 2003	Completed
4-1-B Diffusion model	31 December 2003	In progress
4-1-C Simulation	31 March 2005	Starts in Year-2
4-2. Implementation of Chemical Equilibrium Model	31 December 2003	In progress
4-2-A. Simulation	31 March 2005	Starts in Year-2
5. Neutronic Modeling	31 December 2005	In progress
6. V&V Simulation	31 December 2005	In progress
6-1. RCCS validation	31 December 2005	In progress
6-2. System code vs. CFD code	31 December 2005	In progress
6-3. Large-scale air ingress analysis	31 December 2005	Starts in Year-3
6-4. System-scale simulation	31 December 2005	Starts in Year-3

ID	Task Name	Duration	Start	Finish
1	**CFD TH Code Development**	2.5 yrs	01 Jan 03	30 Jun 05
	- CFD TH model		01 Jan 03	31 Dec 04
	- Diffusion model		01 Jan 03	31 Dec 03
	- Chemical reaction model		01 Jan 04	30 Jun 05
	- Particle model		01 Jan 04	30 Jun 05
2	**RCCS Separate Experiment**	2.5 yrs	01 Jan 03	30 Jun 05
	- Conceptual development of water-pool RCCS		01 Jan 03	31 Dec 03
	- Scaling of water-pool RCCS		01 Jul 03	30 Jun 04
	- Heat transfer coefficients		01 Jan 04	30 Jun 05
3	**Air Ingress Separate Experiment**	2.5 yrs	01 Jan 03	30 Jun 05
	- Measurement technique development		01 Jan 03	30 Jun 04
	- Diffusion-limited model		01 Jan 04	30 Jun 05
4	**Improvement of System Codes**	2.25 yrs	01 Jan 03	31 Mar 05
	- Implementation of diffusion model		01 Jan 03	31 Mar 05
	- Noncondensable gas implementation		01 Jan 03	30 Apr 03
	- Diffusion model		01 Jan 03	31 Dec 03
	- Simulation		01 Jan 04	31 Mar 05
	- Implementation of chemical equilibrium model		01 Jan 03	31 Dec 03
	- Simulation		01 Jan 04	31 Mar 05
5	**Neutronic Modeling**	2.5 yrs	01 Jun 03	31 Dec 05
6	**V&V Simulation**	2 yrs	01 Jan 04	31 Dec 05
	- RCCS validation		01 Jan 04	
	- System code vs. CFD code		01 Jan 04	
	- Large scale air ingress analysis		01 Jan 05	
	- System scale simulation		01 Jan 05	

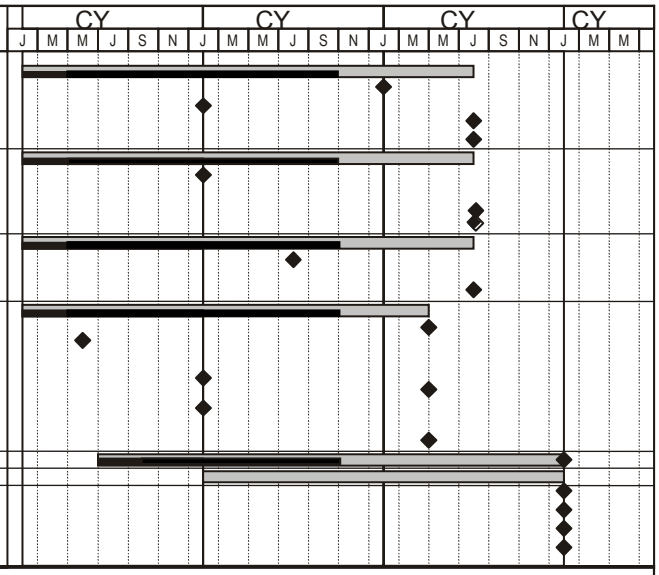

04-GA50018-01